Extreme ultraviolet probing of laser irradiated solid targets

Lucy Aileen Wilson

A thesis submitted for the degree of Doctor of Philosophy

The University of York
Department of Physics

March 2013

Abstract

This thesis explores the applications of extreme ultra-violet (EUV) radiation to the probing of plasma materials and the importance of extreme ultra-violet radiation in radiative transfer in plasmas relevant to both ICF and astrophysics.

The complex refractive index of solid aluminium and the imaginary part of the refractive index of solid iron between 17 eV and 39 eV have been measured using EUV harmonics produced from an 800nm laser focused to 10^{14}Wcm^{-2} in an argon gas jet impinging on a double slit interferometer. There is potential for further work with this method to measure the complex refractive index of plasma material.

It is shown that the drop in opacity when bound-free photo-ionization is no longer energetically possible, enables measurements of the transmission of extreme ultra-violet (EUV) laser pulses at 13.9 nm to act as a signature of the heating of thin (50 nm) iron layers with 50 nm thick parylene-N (CH) overlay irradiated by 35 fs pulses at an irradiance of 3×10^{16} Wcm^{-2}. Comparing EUV transmission measurements at different times after irradiation to fluid code simulations shows that the target is instantaneously heated by hot electrons (with approximately 10% of the laser energy), followed by thermal conduction.

The diagnostic potential of extreme ultraviolet (EUV) coherent probing within a laser produced plasma with a simple transmission footprint is investigated. A fluid code is used to model the interaction of a 35fs, 2×10^{14}Wcm^{-2} 800nm laser pulse with an 800nm thick aluminium target. A post processor is used to calculate the target's refractive index and transmission to 45eV radiation. The effects of EUV radial phase variations at the rear of the target on the intensity distribution at a detector 1.5m from the target are studied. An irradiated aluminium target is found to have little effect on the transmission of 45eV radiation. However, there can be significant phase differences in the probing beam in the radial direction due to heating beam footprint variations for example due to a non-uniform focal spot. These phase variations affect the subsequent propagation of the radiation, suggesting a simple diagnostic measuring the far-field footprint of coherent EUV radiation passing through an irradiated target is sensitive to radial variations of the target heating.

Contents

List of Figures

Acknowledgements

First and foremost I would like to thank my supervisor Professor Greg Tallents for his patience and the support and guidance he has given me throughout this work.

I have enjoyed working long hours on experiments, surviving summer schools and conferences and having useful discussions with current and previous members of the laser plasma physics group namely Reem Alraddadi, Ozgur Culfa, Robert Crowston, Rachel Dance, Tom Fox, Lauren Hobbs, Andy Rossall, Mohammed Shahzad and Erik Wagenaars. In particular I am grateful to Nigel Woolsey for his advice and support and to John Pasley for his advice and for providing access to the HYADES code along with Raoul Trines at the CLF.

I would also like to thank the rest of the fusion DTN students for their encouragement over the last 3 and a half years and Rebecca Dean for her support, encouragement and the vital provision of tea and cake throughout my time in York.

I am grateful for support of Emma Springate, Edmond Turcu, Cephise Cacho and the rest of the Artemis and CLF staff which was vital for the work performed on Artemis and I would also like to thank the target fabrication group at the CLF for their support. I am grateful to Olivier Guilbaud, Sophie Kazamias and the rest of the LASERIX team for their assistance and the time and hard work that went into insuring the LASERIX experiment was a success.

Finally, I would like to thank my little brother Daley and my parents for their patience, encouragement and support over the years.

Author’s Declaration

I declare that the work presented in this thesis, except where otherwise stated, is based on my own research and has not previously been submitted for a degree at this or any other university.

Parts of the work presented in this thesis have been published in some of the papers listed in Appendix C.

Lucy Aileen Wilson

Chapter 1

Introduction

This thesis explores the application of extreme ultra-violet radiation to the probing of plasma materials and the importance of extreme ultra-violet radiation in radiative transfer in plasmas.

The extreme ultraviolet (EUV) spectral region extends between photon energies of approximately 30eV - 250eV, while the spectral region from 250eV - several keV is often referred to as the soft x-ray region [1]. The EUV region is characterised by high absorption and low reflectance in most materials. Absorption in solids is high due to the presence of atomic resonances and absorption edges associated with the removal of inner shell electrons in medium and low Z materials (see fig. 1.1). Lower energy photons will be absorbed by conduction band electrons to produce phonons (see fig. 1.2).

Reflection in the EUV is low because the refractive indices are close to unity, with refractive indices less than one also common in the EUV region, because the frequency of radiation in the EUV region ω is often much higher than the critical frequency ω_c of the conduction band electrons or the free electrons created upon ionisation of the material to create a plasma.

There are a variety of intense EUV coherent radiation sources including high harmonics generated by high power laser interaction with solid or gas targets, x-ray free electron lasers (XFELs) where coherent radiation is produced by an oscillating beam of electrons and plasma based EUV lasers where the gain medium is a high Z, high temperature plasma. High harmonics produced in gas jets and EUV lasers are both utilised in this thesis to probe solid and laser heated materials. Coherent EUV sources are discussed in more detail in chapter 3. Incoherent EUV radiation sources have been produced by the laser irradiation of solid targets [2] and from plasmas produced in Z pinches [3] (see chapter 2 subsection 2.3.5) . XFELs and other EUV sources have signifi-

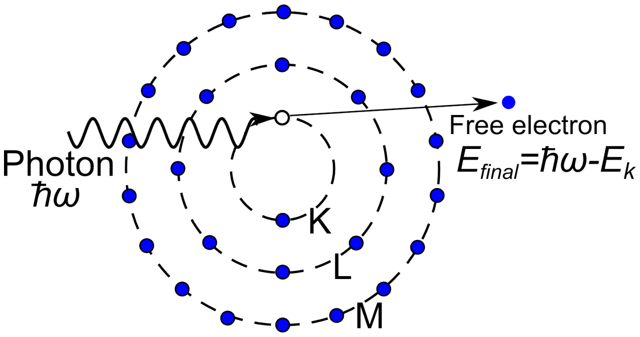

Figure 1.1: Schematic showing K shell photoionisation of a bound K shell electron by a photon of energy $\hbar\omega$. If the K shell ionisation potential is E_k a free electron of energy $\hbar\omega - E_k$ is created. Shells are labelled K, L, M,.. corresponding to the principle quantum numbers n = 1, 2, 3, ..

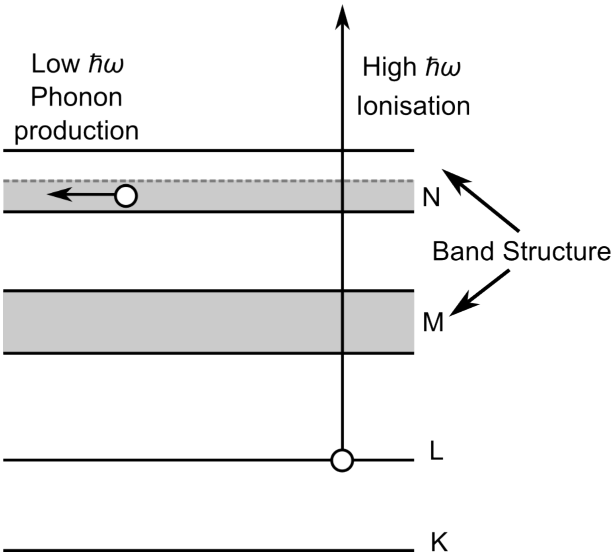

Figure 1.2: Schematic showing atomic band structure of the N and M shell with thermal low energy ($\hbar\omega$) photons exciting conduction band electrons to produce phonons and high energy photons ionising inner shell electrons.

cant potential in imaging small structures such as protein molecules using x-ray radiation scatter. Ultrashort pulses allow the imaging of the molecule before damage from the x-rays occurs [4]. Coherent high brightness ultrashort x-ray pulses can be used for coherent diffractive imaging which allows imaging of nanoscale non-periodic objects, such as a virus or a cell, by reconstructing an image from the diffraction pattern of the object using a phase retrieval algorithm [5].

The short pulse lengths and high intensities of XFEL sources allow the heating of targets before they have had time to expand, allowing the creation of high energy density uniform plasmas dominated by radiative processes [6, 7]. Nagler et al. (2009) [7] describe the creation of uniform warm dense matter aluminium samples at 25eV electron temperatures with an XFEL with an intensity of 10^{16}Wcm^{-2} and a photon energy of 92eV. The absorption is dominated by L-shell photo absorption. The absorption becomes saturated as all the aluminium atoms are ionised, and the aluminium consequently becomes transparent.

1.1 Applications of EUV Probing

The optical properties of solid materials need to be known to a high degree of accuracy for the production of EUV optics. EUV optics are required for a variety of applications where EUV radiation needs to be reflected or focused. Examples of where EUV optics are required include EUV astronomy where high angular resolution images can be produced with multilayer optics and plasma diagnostics were EUV and x-ray emission from a high temperature plasma is of interest. The optical properties of radiation filters frequently made of materials such as aluminium are also important for plasma diagnostics. Semiconductor lithography is being developed to use EUV wavelength radiation to copy the sub - microscale ($<$100nm) highly detailed patterns required to produce microchips and therefore, requires high efficiency EUV optics .

The EUV optical properties of plasmas, such as the opacity are not well known and are difficult to model theoretically, for example, due to the high number of bound - bound transitions possible in high Z atoms. Opacities can be difficult to measure experimentally due to the requirement of a source to be brighter than the plasma self emission and the difficulty of creating uniform plasmas of well - defined density and temperature . Plasma opacity, opacity modelling and experiments are discussed in more detail in chapter 2 section 2.3.

The short wavelengths of the EUV region allow probing of plasmas to higher densities than optical radiation probes due to the higher critical density n_c. The critical density is given by $n_c = \frac{1.1\times10^{21}}{\lambda^2}$, where λ is the wavelength in microns. EUV radiation of wavelengths shorter than approximately 50nm can probe unionised solid density material without collective absorption. We show in this work that EUV probing radiation is particularly sensitive to plasma conditions between the ablation surface and the critical density of the plasma production laser.

There are several potential applications of laser plasmas including inertial confinement fusion (ICF) and the creation of material relevant to astrophysical plasmas such as stellar interiors. EUV radiation is particularly important in ICF where a radiation field is created in a hohlraum and in radiation transfer within stars. These two important applications of laser - plasmas (ICF and stellar radiation transfer) are reviewed below.

1.1.1 Inertial Confinement Fusion

Inertial confinement fusion involves the implosion of a capsule of deuterium - tritium (DT) fuel using the inertia of the fuel itself to achieve confinement. DT fuel is used as there is a larger reaction cross section at lower temperatures than reactions involving other fuels, for example the deuterium - deuterium fusion reaction. Fusion has to take place within the time for a rarefaction wave to cause expansion of the compressed fuel. This is approximately the time for a sound wave to propagate from the surface to the centre of the fuel capsule. In order to achieve fusion on the necessary short timescale (<nanosecond) very high densities (100 - 1000gcm^{-3}) are required to produce the high reaction rates needed. In contrast, with magnetic confinement fusion, plasma is confined by magnetic fields at a low density (10^{-4} gcm^{-3}) over a long time scale (10s of seconds) [8].

In order to achieve high temperatures and densities the fuel is compressed adiabatically by implosive shocks driven by energy from a driver ablating shell material containing the fuel. The driver energy can be supplied directly by uniform laser irradiation in the case of direct drive, or soft x-rays emitted from a blackbody cavity heated by laser beams in the case of indirect drive (see Fig. 1.3). The symmetric ablation of the fuel capsule surface causes an implosion in order to conserve momentum. Ignition will occur within a central hot spot at temperatures of ≈5keV. A temperature > 5keV is required for energy produced via fusion reactions to overcome losses, for example via bremsstrahlung [9]. The critical value of ρR, where ρ is the density and R is the radius, required for fusion in a central hot spot of temperature of 10KeV is given by [9, 10]:

$$\rho R = 0.3\,\mathrm{gcm}^{-2} \tag{1.1}$$

A value of $\rho R \approx 0.3$gcm^{-2} is approximately the range of the α particles emitted from DT fusion and so α particles can be reabsorbed in the fuel causing the temperature to increase further. As the temperature increases the range of the α particles also increases, heating up the surrounding material and causing a propagating burn wave [10]. To achieve high gain, a substantial fraction of the fuel needs to be burnt before the confinement is lost. If the burn fraction is ≈33%, a higher value of $\rho R = 3$gcm^{-2} is required [9].

Indirect drive fusion uses thermal x-ray radiation emitted from a heated black body cavity to drive the implosion. This method of inertial confinement fusion is used on the National Ignition Facility (NIF), at Lawrence Livermore National Laboratories. NIF uses 192 laser beams focused

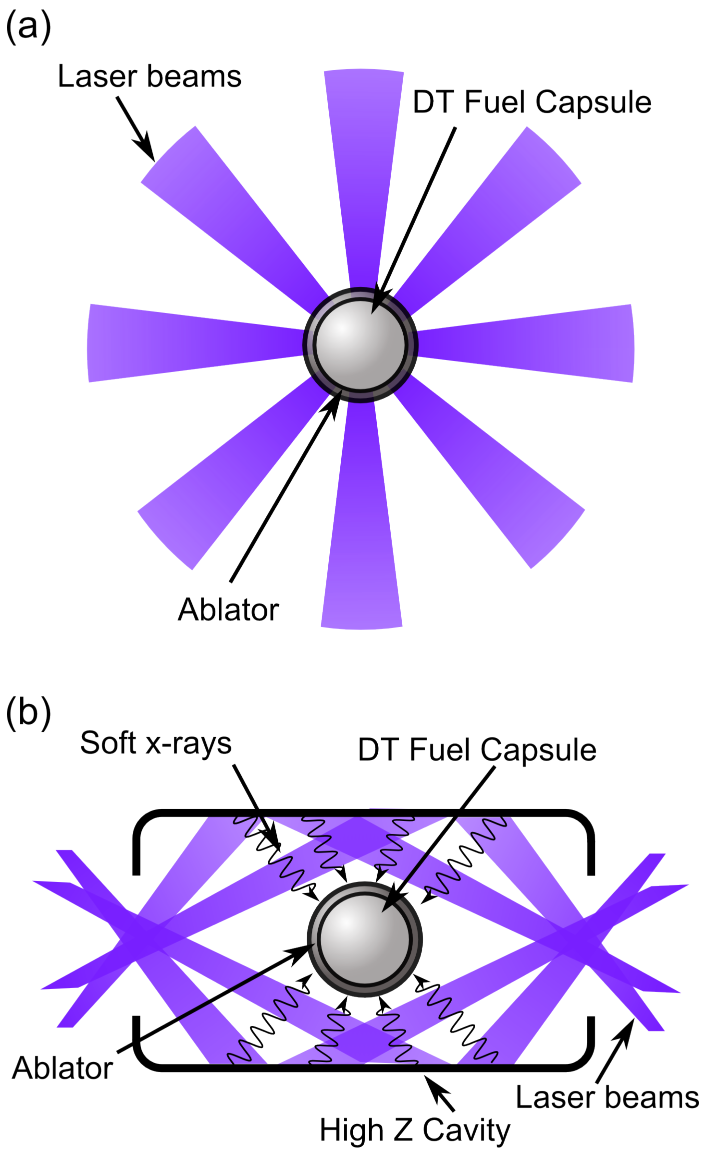

Figure 1.3: Diagram of (a) direct drive inertial confinement fusion and (b) indirect drive inertial confinement fusion

into a high Z cavity, known as a hohlraum, to produce the x-ray driver. These beams are arranged into 4 cones entering each side of the cavity at angles from 23.5° to 40°

In indirect drive fusion blackbody hohlraums are heated by laser irradiation of the inside wall (up to temperatures of $\approx 3 \times 10^6$K [8]) with the aim of improving driver uniformity to prevent the seeding of hydrodynamic instabilities such as the Rayleigh - Taylor instability. The laser beams enter the hohlraum through holes on the axis and are directed onto the walls, heating them and forming hot spots. The heated hohlraum walls absorb and re-emit radiation producing a near Planckian distribution of photons peaking in the soft x-ray region and heating the inside of the hohlraum to about 300eV [11]. These x-rays heat the outer layer of the fuel capsule ablating the surface [9]. The fuel capsule typically consists of an outer ablator layer of a low Z material such as plastic or Be, surrounding a layer of frozen DT and an interior of high pressure DT gas. Typically the total radius of a fuel pellet is about 1mm [12].

To improve efficiency, hohlraums are made of high Z materials so that they have high opacity and absorb most of the incident laser energy, decreasing radiation flow through the wall. The high absorption of the walls means radiation transport through the wall can be assumed to be a radiative diffusive Marshak wave. Opacity of the wall is high because from Kirchhoff's law, if LTE is assumed the greater the absorption, the greater the re-emission of energy as x-rays from the hohlraum walls. Therefore, to improve the efficiency of a hohlraum it is necessary to maximise the opacity over the EUV and x-ray range. One approach is to create hohlraums using a mixture of high Z elements in order to maximise opacity over a wide range of wavelengths, as regions with low opacity in one element may have a high opacity in another [12]. Designs of hohlraums used on NIF include using uranium (U) with a gold (Au) inner surface, Au / U / Au 'sandwich' hohlraums and pure Au hohlraums. It is estimated that U / Au layered hohlraums are 5 - 10 % more efficient than pure Au requiring lower laser peak power and energy [11].

The x-rays or laser in direct drive, heat up the ablator layer of the target which expands outwards forcing the rest of the shell to collapse inwards in order to conserve momentum. Shockwaves are driven into the fuel. The laser pulse intensity is increased with time so that typically a total of 4 shock waves are driven into the target, timed in order that they meet at the inner edge of the solid DT layer. These shock waves compress the fuel to the high densities required. Finally, at stagnation when the material comes to rest, the capsule is isobaric with a central hot spot (density of 100gcm^{-3}) surrounded by a lower temperature denser region of fuel (density of 1000 gcm^{-3}). When a density of 100gcm^{-3} value is reached fusion reactions will start in the hot spot and cause a burn wave to propagate outwards igniting the rest of the fuel [9, 10].

Opacity is also an important factor in choosing materials for the ablator layer of a fuel capsule. The ablator layer needs to have a low opacity when heated so that radiation can easily be transmitted through the exhaust and a high opacity when cold so that radiation is absorbed. Because of this low Z materials doped with layers of higher Z impurities are used [10]. For example, NIF targets use either CH/Ge (0.5%Ge) or Be/Cu (1%Cu) ablators. The Ge and Cu are added to reduce preheating by photons from x-ray M and O band radiation produced in the laser hot spots on the hohlraum walls and to reduce the effects of windows in the opacities of low Z materials near their K edge [9, 11]. Collective processes within the ablated material can also produce hot electrons which have much larger energies than thermal electrons, preheating the fuel and reducing compression efficiency.

The fast ignition approach to ICF involves separating the compression of the fuel from ignition, with the compressed fuel being ignited by an external driver, usually a beam of energetic particles generated by an ultra intense short pulse laser interaction. Separating the compression from the ignition reduces the requirements for highly symmetric irradiation. One approach is to use the fast electrons generated at the tip of a high Z cone, which helps guide the beam to the hotspot. This approach relaxes the symmetry requirements of central hotspot ignition. The main fuel density can be lower than in central hot spot ignition resulting in a compressed fuel requirement of a temperature of ≈10keV and $\rho R = 0.5\text{gcm}^{-3}$. The igniter pulse duration must be less than the confinement time for the hotspot, typically <20ps. Particles used to heat the hot spot must also have penetration depths less than the hot spot diameter [8].

Work in this thesis includes measuring energy transport by thermal electrons and determining heating by hot electrons in short pulse laser heated targets. This work has applications in inertial confinement fusion as energy transport from the region where the laser energy is deposited to the ablation surface of the capsule effects the efficiency of capsule implosions in direct drive fusion. In the indirect drive case, the energy transport through ablated material from the wall is significant with recent discrepancies between simulated and observed data on NIF having been found to be related to electron transport models (see chapter 2 section 2.1.5).

1.1.2 Stellar Structure

Stellar structure and evolution depends on energy transport through the interior of a star. Accurate values of opacities are necessary to fully comprehend the mechanism behind the pulsation of intrinsic variable stars such as the Cepheid variables. Understanding the pulsation of the Cepheid variables is essential for astronomy and cosmology as they are used as standard candles to measure distances between galaxies and within galaxies. For example, Cepheid variables have in the past been used to measure the shape and size of the Milky Way galaxy and the position of the solar system relative to the centre [13, 14].

Within stellar interiors, the photon mean free path is very much smaller than the characteristic length of the system - for example the radius of the star. Therefore, transport of energy by photons can be modelled as a diffusion process with the diffusive radiative flux in the interval ν, $\nu + d\nu$, F_ν given by [15]:

$$F_\nu = -D_\nu \nabla U_\nu \tag{1.2}$$

where U_ν is the energy density given by $U_\nu = \frac{4\pi}{c} B(\nu, T)$, where $B(\nu, T)$ is the Planckian radiation formula. D_ν is the diffusion coefficient given by:

$$D_\nu = \frac{1}{3} c \lambda_{mfp} = \frac{c}{3\sigma_\nu \rho} \tag{1.3}$$

where λ_{mfp} is the mean free path. ∇U_ν is then given by:

$$\nabla U_\nu = \frac{4\pi}{c}\frac{dB(\nu,T)}{dT}\nabla T \quad . \tag{1.4}$$

Combining (1.2),(1.3) and (1.4) gives:

$$F = -\left[\frac{4\pi}{3\rho}\int_0^\infty \frac{1}{\sigma_\nu}\frac{dB(\nu,T)}{dT}d\nu\right]\nabla T \quad . \tag{1.5}$$

Using $\int_0^\infty \frac{dB(\nu,T)}{dT}d\nu = \frac{acT^3}{\pi}$, where a is the radiation density constant and substituting in the Rosseland mean opacity (see chapter 2 subsection 2.3.4) given by:

$$\frac{1}{\sigma_R} = \frac{\int\limits_0^\infty d\nu \frac{1}{\sigma(\nu)}\frac{dB_\nu}{dT}}{\int\limits_0^\infty d\nu \frac{dB_\nu}{dT}} \tag{1.6}$$

gives:

$$F = -\frac{4ac}{3}\frac{T^3}{\sigma_R\rho}\frac{dT}{dr} \quad . \tag{1.7}$$

The opacity of the plasma material has an effect on how efficiently energy is transported and therefore, determines the temperature gradients within the star. Rearranging (1.7) and using $F = \frac{L}{4\pi r^2}$, where L is the luminosity gives an expression for the radiative temperature gradient [16]:

$$\frac{dT}{dr} = -\frac{3}{4ac}\frac{\rho\sigma_R}{T^3}\frac{L}{4\pi r^2} \quad . \tag{1.8}$$

In the region just below the stellar convection zone the temperature is ≈190eV giving the peak value of $\frac{dB(\nu,T)}{dT}$ at a photon energy of ≈750eV. This means the peak radiative flux is in the EUV and soft x-ray region making the optical properties and radiation transport in this photon energy region important [17].

The radiative temperature gradient determines the depth of the convection zone [14]. When the radiative temperature gradient becomes greater than the adiabatic gradient, convection becomes the dominant form of energy transport. This is the point when a rising bubble of gas that is displaced upwards will still be at a higher temperature than its surroundings. If the gas rises adiabatically to a region with lower pressure it expands, doing work on its surroundings and losing internal energy. If this rate of temperature change is less than its surroundings, it will be at a higher temperature and will continue to rise.

The adiabatic gradient is determined by the adiabatic requirement from the ideal gas laws that for a pressure P and a volume V the condition $PV^{\gamma_{ad}}$ is constant where γ_{ad} is the ratio of specific heats for constant pressure and constant volume. For an ideal gas $\gamma_{ad} = \frac{5}{3}$, leading to the condition that $T^3(n_e+n_i)^{-2}$ is constant, assuming $V \approx \frac{1}{(n_e+n_i)}$ and where T, n_e and n_i are the temperature and electron and ion densities respectively and using the ideal gas law given by:

$$P = (n_e + n_i)k_B T \quad . \tag{1.9}$$

To find the adiabatic gradient we can differentiate 1.9 with respect to radius and obtain:

$$\frac{dP}{dr} = \frac{dT}{dr}\frac{P}{T} + \frac{d(n_e + n_i)}{dr}\frac{P}{(n_e + n_i)} \tag{1.10}$$

Differentiating the adiabatic condition $PV^{\gamma_{ad}} =$ constant, with respect to radius, substituting in 1.10 and rearranging for $\frac{dT}{dr}$ we obtain the adiabatic gradient:

$$\frac{dT}{dr} = \frac{1-\gamma_{ad}}{\gamma_{ad}}\frac{T}{P}\frac{dP}{dr} \quad . \tag{1.11}$$

The radiative temperature gradient can exceed the adiabatic gradient when ionisation and bound-

bound transitions start to become important and the opacity starts to increase [16]. In stars of mass around $1\mathrm{M}_\odot$ ($\mathrm{M}_\odot = 1$ solar mass) this occurs in the outer layers. For example in the sun the lower boundary of the convection zone has been observed to be at a radius of $0.713\mathrm{R}_\odot \pm 0.001\mathrm{R}_\odot$ from helioseismic observations [18]. Figure 1.4 illustrates this effect. Temperature gradients are plotted against radius for a variety of metal ($Z \geq 3$) contents for a $1\mathrm{M}_\odot$ main sequence star. Increasing metal content increases the opacity. The adiabatic gradient $\frac{dT}{dr}$ is also plotted. The point where the radiative and adiabatic gradients cross indicates the depth of the convection zone. Fig. 1.4 data is from a simplified web based version of the stellar model Evolve-ZAMS [19], called EZ-web [20].

Metals (Z $\geq$3) can have a large contribution to the solar opacity despite having relatively low abundances (see fig 1.5). The three largest contributors to the opacity in the region below the convection zone are oxygen, iron and neon. Iron has a solar mass fraction of about 10^{-3}. However, it remains partially ionised down to the core of the sun so that a range of bound - bound and bound - free transitions can occur. The contribution of bound - bound absorption to the total opacity is increased by the high densities within stars as the absorption lines are broadened by collisions [15]. At the base of the convection zone, iron is most commonly in a F, O or Ne-like state, with a large number of possible bound-bound transitions. The most abundant elements, hydrogen and helium, are fully ionised in the region at the base of the convection zone.

Recently discrepancies have been found between the depth of the solar convection zone observed from helioseismology and that calculated from stellar models. This was caused by observations of up to 25% lower solar surface metal abundances compared to those previously used in models from a metallicity of 0.0229 to 0.0165 [22, 23]. An example of the reduction in oxygen abundance is described in Asplund et al (2004). Here the abundance is determined by photospheric absorption lines and is also compared to observed abundances in nearby stars [24]. This decrease of the solar metallicity effects the opacity of the solar interior as abundant metals are

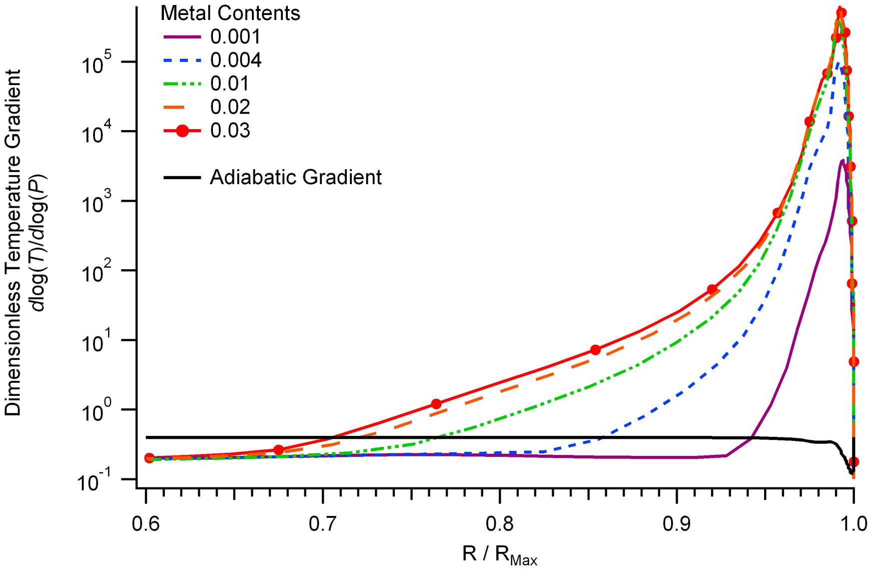

Figure 1.4: Graph showing the dimensionless gradients defined as $\frac{d\log T}{d\log P}$, as a function of radius in the interior of a $1\mathrm{M}_{\odot}$ star with different metal contents. Where the radiative (coloured lines) and adiabatic gradients (black solid line) cross indicates the depth of the convection zone. (Calculated using EZ - Web [20])

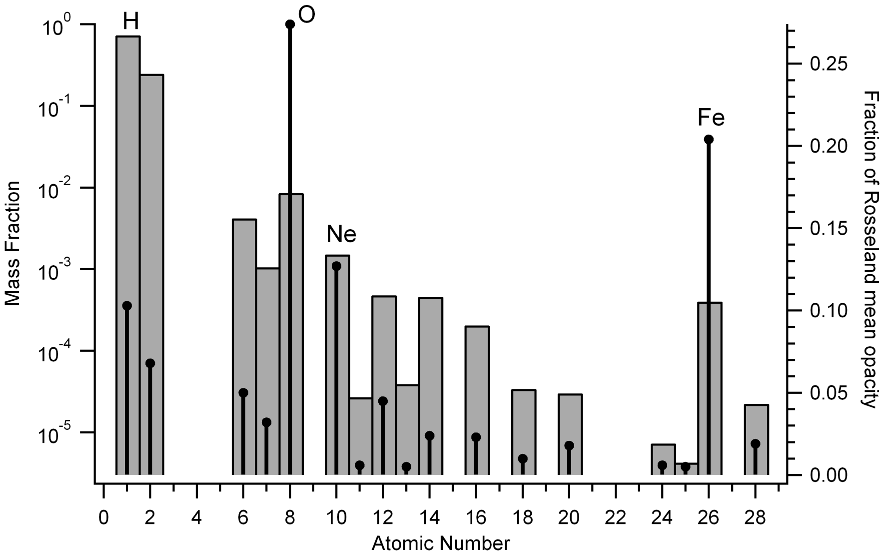

Figure 1.5: Bars: Mass fraction of different elements within the solar interior. Lines: Fraction of Rosseland mean opacity contributed by each element near the base of the convection zone. Data adapted from [17] and [21].

major contributors to opacity in the region just below the convection zone [24].

It has been suggested by Bahcall et al (2005), that an increase in the Rosseland mean opacity of 10% in the temperature range $2-5\times10^6$K, corresponding to around $0.4-0.7\mathrm{R}_{\odot}$, would solve this inconsistency and bring observations back into agreement with stellar models [22]. However, another suggestion given by Drake et al (2005) is an increase in the solar neon abundance by at least a factor of 2.5. Neon abundance is not well known and is hard to measure accurately in the solar photosphere as neon photospheric absorption lines are not detectable in the visible region of the solar spectrum. Measurements of neon emission in the EUV and soft x-ray region will give measurements of the abundance of neon in the higher temperature solar corona rather than the photosphere. Measurements of x-ray spectra from the corona of nearby stars were used to produce estimates of the solar Ne abundance that was greater than previous measurements [23]. More recently, solar abundances have again been revised and increased by 10% to 0.0178. However this is still much lower than measurements previously used giving the convection zone depth of $0.724\mathrm{R}_{\odot}$. Again, it is suggested in Serenelli et al (2009) that if calculated opacities are modified, a $2-5\%$ increase in the opacity towards the core of the sun rising to a $10-15\%$ increase at the base of the convection zone would be required [25].

1.1.3 Variable Stars

Intrinsic variable stars undergo periodic fluctuations in luminosity due to some internal mechanism. One group of these stars pulsate radially due to the opacity or 'κ' mechanism. An important example of this type of star are the Cepheid variable which are metal-rich stars that pulsate over periods of 1-50 days. The Cepheids are high surface temperature, high luminosity stars that start to pulsate after they have started to burn helium. A star may undergo several periods of pulsation during its lifetime [14].

The relationship of the pulsation period to their luminosity means Cephied variables are useful as standard candles. A measurement of the pulsation period indicates their absolute luminosity and therefore, their distance. Cepheid variables are used to measure distances of galaxies up to around

20Mpc and can be used to calibrate the distance of type 1A supernovae enabling estimates of the Hubble constant which indicates the age and size of the observable universe [26]. Cepheids have also been used to measure galactic properties such as the distance to the centre of the Milky Way galaxy, the sun's position in relation to the galactic plane and to map the spiral arm structure of the Milky Way [27].

The driving mechanism behind the pulsation of Cepheid variables is driven by increases of opacity with temperature and pressure in ionisation regions in the outer layers of stars. This usually occurs in the He^{+} ionisation region. Metal opacities, in particular due to iron M-shell transitions, have been found to have a significant effect increasing opacity at around $Log_{10}T = 5.3$. This is shown in fig 1.6 as 'bumps' in the opacity with temperature. The effects of different values of metal content are also plotted. These lines are at constant R_{PR}, the ratio of pressure to radiation pressure given by $R_{PR} = \frac{\rho}{\left(\frac{T}{10^6 K}\right)^3}$, where T is the temperature and ρ is the density in gcm^{-3} [28].

This increase of opacity with temperature and pressure means the contraction of a star will lead to an increase in its opacity, trapping radiation, reducing luminosity and further increasing the temperature of that region. This then increases temperature and pressure further until the star once more starts to expand and cool. The opacity drops and radiation can escape allowing the star to contract under gravity and the cycle to begin again [14]. Models of the pulsation of some types of variable stars such as the beat Cepheids, whose mass can be found from the ratio of 2 different pulsation modes occurring within the star and β Cephei stars (rapidly pulsating main sequence stars), had poor agreement with observations. It was suggested by Simon (1982) that increasing the contribution of heavy elements to the opacity in the temperature range of $log_{10}T$=5 - 6, increasing the total opacity by a factor of 2 - 3, would lead to much greater agreement [29].

New calculations by both the OPAL and opacity project groups found that more detailed atomic level data using either LS or full intermediate coupling, lead to increases in opacity, of

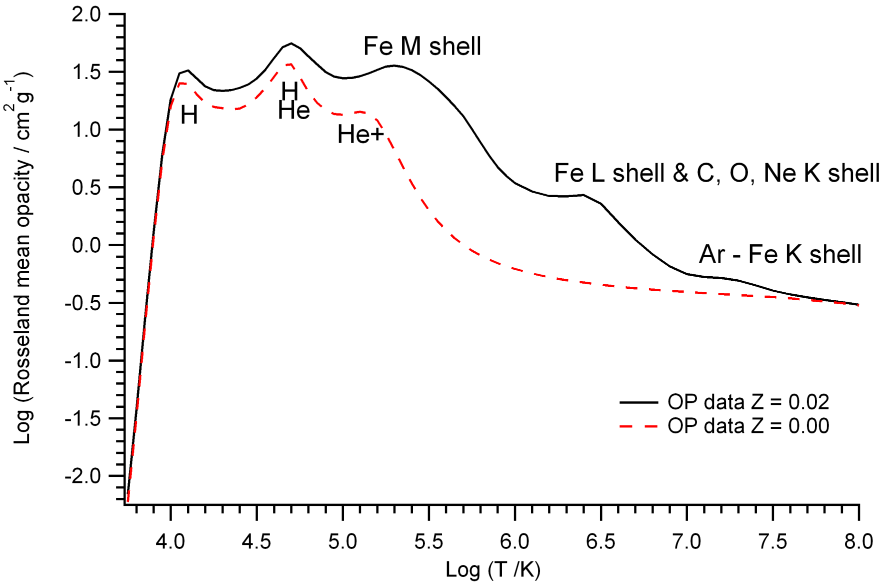

Figure 1.6: Log of the Rosseland mean opacity vs log of Temperature. Data is from The Opacity project for a solar composition of elements [21] for constant R_{PR} adapted from [14].

in particular iron, where there had previously been low opacity in the Rosseland integral [14]. The M - shell $n = 3 - 3$, ($\Delta n = 0$) transitions of iron occur near the maximum of $\frac{dB_v}{dT}$, giving them a large contribution to the opacity. Fig (1.6) shows opacities from the opacity project with this correction and the contribution due to the Fe M shell shown [14]. The modified OPAL opacities were also corroborated by experimental results using radiatively heated iron foils by Da Silva et al (1992) [2].

Measuring opacities over the full range of temperatures and densities relevant to inertial confinement fusion or astrophysics is unlikely to be possible due to the large parameter range. For example, the densities within the sun go from less than 10^{-7}gcm^{-3} in the photosphere to up to 150gcm^{-3} in the core, with temperatures varying between $\approx$ 1keV – 0.1eV [17]. Accurate theoretical models of opacities over a wide range of conditions are important. However, modelling opacity accurately is also difficult and computationally intensive primarily due to the large number of bound - bound transitions possible in medium to high Z elements over a range of different ionisation stages. Consequently a range of different approximations are used. Experimental measurements of opacities in regions of interest are required to benchmark codes by indicating their accuracy, and the validity of approximations.

Chapter 5 studies iron absorption, comparing several different opacity models using different approximations and levels of complexity to experimental transmission measurements. Previous experiments using EUV probing to measure opacity using EUV sources are described in more detail in chapter 2.

1.2 Summary

The EUV region is of interest for a variety of applications with EUV sources being used for imaging of microscale objects and creation of high energy density radiation dominated states. EUV optical properties are required to a high degree of accuracy for EUV lithography which uses the short EUV wavelengths to produce the small details required for microchip production. EUV probing can be used as a diagnostic of radiation transport and hot electron heating which has applications in ICF. EUV measurements of optical properties of plasmas are also required for both ICF and astrophysics.

1.3 Work Undertaken by the Author

The author was involved with the planning and target design for the double slit interferometry experiment detailed in chapter 4 and was a member of the experimental team who obtained the data. The diffraction data obtained has been analysed by the author to obtain the complex refractive index of aluminium and imaginary refractive index of iron which are discussed in chapter 4.

The author was involved in obtaining the EUV transmission data for a short pulse laser irradiated iron foil shown in chapter 5 along with the team from LASERIX. The analysis of this data was performed by the author to obtain the transmission data shown. Simulations were carried out by the author using the commercially available code HYADES developed by CASINC [30]. The transmission post-processor was originally developed by L. Hobbs [31] and has been modified by the author to include new opacity data and to include the parameters of the LASERIX experiment.

Chapter 6 uses the HYADES code to model a short pulse laser irradiated aluminium target to produce electron density and temperatures. These are used in a post-processor written by the author alone to produce values of opacities and refractive indices throughout the aluminium target using Saha - Boltzmann state populations. The author is responsible for developing a simple novel evaluation of refractive indices near an absorption edge using the Kramers - Kronig relation. The refractive indices are used to calculate the phase shift of radiation through the target. Examples of possible phase distributions are Fourier transformed to produce the intensity distributions in the far - field. This data manipulation was undertaken by the author using IDL programming.

Chapter 2

Theoretical Background

This chapter presents the background theory to the experimental and simulation work discussed in chapters 4 - 6. Laser plasma interactions, including ionisation, absorption and energy transport are described. Plasma opacity, opacity modelling and experiments are introduced and the plasma refractive index and the Kramers - Kronig relationship relating real and imaginary parts of the refractive index are discussed.

2.1 Laser Plasma Interactions

This subsection 2.1 presents an overview of laser plasma physics at laser intensities of up to $\approx 10^{17}\mathrm{Wcm}^{-2}$, where electrons are not sufficiently accelerated to undergo relativistic mass increase. Ionisation mechanisms and ablation of a material under laser irradiation, the transfer of energy from the laser into the target and energy transport are discussed.

2.1.1 Initial Ionisation

When a solid surface is irradiated by a high intensity (I), optical laser such that $I > 10^{10}\mathrm{Wcm}^{-2}$ [32]), a fraction of the laser radiation is absorbed at the surface of the material and the remainder is reflected. The material surface is heated and ablated, so that a plasma is rapidly produced in the ablated material as ionisation occurs.

The laser intensity required to directly remove an electron from an atom can be estimated by considering the laser electric field required to overcome the electric field binding the electron to the atom [32]. The intensity I of a laser is related to the average laser electric field E by:

$$I = \frac{\epsilon_0 c \eta}{2} E^2 \tag{2.1}$$

where η is the refractive index of the medium, ϵ_0 is the permittivity of free space and c is the speed of light in a vacuum. Equating the electric field of the atom, $E_{atom} = \frac{e}{4\pi\epsilon_0 a_B^2}$, where a_B is the Bohr radius and e is the electronic charge, to the laser electric field, E, we see that direct ionisation can take place at intensities $> 10^{16}\mathrm{Wcm}^{-2}$. In practise ionisation can occur in the field of a laser at much lower intensities by multi - photon processes or by electron tunnelling.

At intensities below $I \approx 10^{16}\mathrm{Wcm}^{-2}$ atoms become ionised via multi-photon ionisation in which several low energy photons are absorbed by an electron as opposed to a single photon with an energy greater than the ionisation energy. The kinetic energy (E_k) of the free electron after ionisation is given by:

$$E_k = (n_p + s)\hbar\omega_L - I_p \tag{2.2}$$

where n_p is the number of photons required to ionise the atom, s is the number of extra photons absorbed, ω_L is the laser photon frequency, $\hbar$ is Planck's constant divided by 2π and I_p is the ionisation energy. The rate of n-photon ionisation (Γ_n) is strongly dependant on the photon density - or the intensity of the laser [32] with :

$$\Gamma_n = \sigma_n I_L^n \tag{2.3}$$

where σ_n is the cross section for the absorption of n photons.

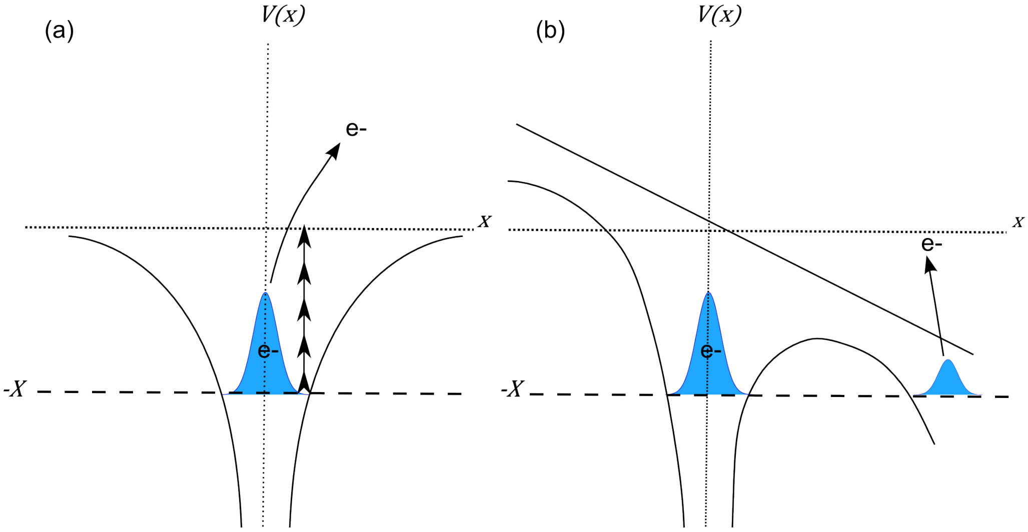

Figure 2.1: (a) shows multi - photon ionisation where an electron is ionised by several photons in an atomic potential $V(x)$ with ionisation energy I_p. (b) shows electron tunnelling ionisation where the electric field of the laser distorts the potential of the atom allowing the electron to tunnel out of the atom.

At high intensities electron tunnelling ionisation also occurs as the electric field of the laser becomes large enough to distort the Coulomb field of the atom, suppressing the Coulomb barrier and increasing the possibility that an electron may quantum mechanically tunnel out of the atomic potential. The ratio of the rate of multi - photon ionisation to tunnelling ionisation is given by the Keldysh adiabaticity parameter (γ_K) [33] where:

$$\gamma_K = \omega_L \sqrt{\frac{2I_P}{I}} \quad . \tag{2.4}$$

If $\gamma_K \gg 1$ as for a high frequency and low intensity laser, multi-photon ionisation will dominate. If $\gamma_K \ll 1$ as for a low frequency and high intensity laser, tunnelling ionisation will dominate. These ionisation processes are summarised in Fig. 2.1

2.1.2 Plasma Expansion

Density gradients within the expanding plasma formed after ionisation affect the subsequent form of laser absorption and the types of interactions and collective processes that occur within the plasma.

The density scale length of an expanding plasma is approximately given by $L = c_s t$ where c_s is the ion acoustic sound speed such that $c_s = \sqrt{\frac{Z^* k_B T_e}{m_i}}$, where Z^* is the average ionisation, T_i is the ion temperature, k_B is the Boltzmann constant and m_i is the ion mass. A self - similar description of the plasma density, assuming a 1D planar isothermal expansion, is given by [34]:

$$n_e = n_o \exp\left(\frac{-x}{c_s t}\right) \tag{2.5}$$

where n_0 is the electron density at $x = 0$.

Photons can propagate through a plasma up to a critical density n_c. The dispersion relation for a cold collisionless plasma is given by Kruer [34] as:

$$\omega_L^2 = \omega_p^2 + k^2 c^2 \tag{2.6}$$

where ω_p is the plasma frequency - the oscillation of the collective electron motion that defines the electron response time, k is the wavenumber and c is the speed of light in a vacuum. As ω approaches ω_p, k must go to 0 so ω_p can be considered the minimum frequency that an electromagnetic wave can propagate through a plasma. Using $\omega_L = \omega_p$ and $\omega_p = \sqrt{\frac{n_c e^2}{m_e \epsilon_0}}$ the critical density n_c is given by:

$$n_c = \frac{m_e \epsilon_0 \omega_p^2}{e^2} = \frac{1.1 \times 10^{21}}{\lambda_{\mu m}^2} cm^{-3} \tag{2.7}$$

for an incident laser wavelength of $\lambda_{\mu m}$ (in μm).

Near the critical density, the density profile can steepen due to the deposition of momentum by reflecting laser photons [34]. Fig. 2.2 shows a typical plasma electron density and temperature profile with different regions indicated.

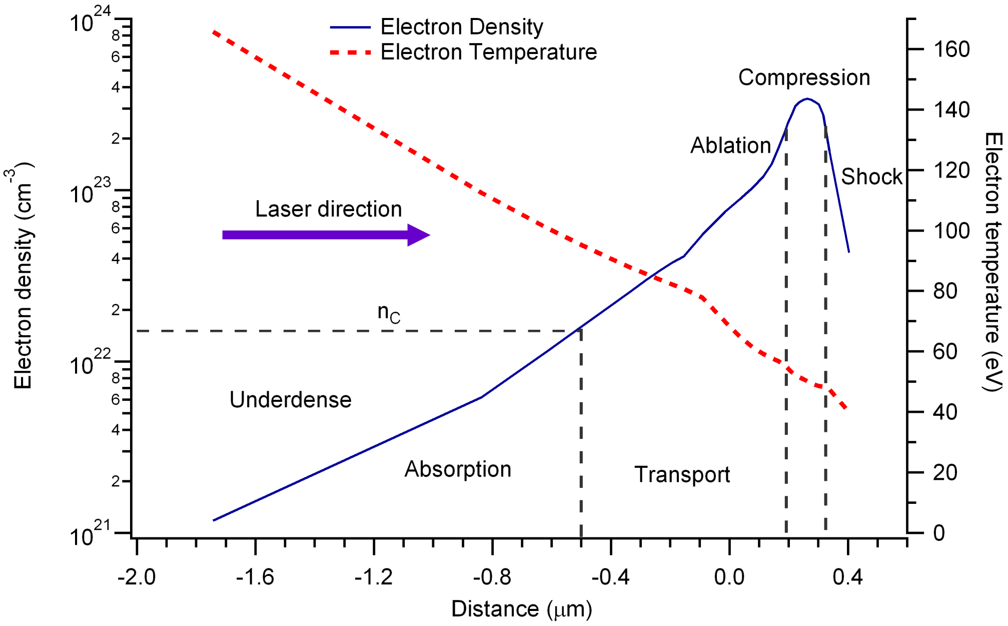

Figure 2.2: Typical electron density and electron temperature profiles from a HYADES simulation of a laser heated iron target. The laser intensity was 3×10^{16}Wcm^{-2} at a wavelength of 0.27μm. The critical electron density is shown, with absorption, energy transport and underdense regions indicated.

2.1.3 Parametric Instabilities

Instabilities occur in the underdense plasma region and are a source of hot electrons (discussed in the next section). Simulated Brillion scattering (SBS) involves the backscattering of an electromagnetic wave from the laser by an ion acoustic wave transferring momentum from the photon into an ion acoustic wave ω_i. This can be described by $\omega_L = \omega_i + \omega_s$, where ω_s is the scattered photon frequency. As the ion wave frequency is low, most of the energy is transferred into the scattered photon. This interaction can occur throughout the plasma underdense region and can have a significant effect on reducing the amount of laser energy absorbed and the location of the peak absorption.

Simulated Raman scattering (SRS) involves the decay of the electromagnetic wave from the laser into an electron plasma wave and a scattered photon, $\omega_L = \omega_p + \omega_s$. As $\omega_s \geq \omega_p$ in order to propagate through the plasma, this process therefore, occurs at electron densities $n_e \leq \frac{n_c}{4}$. As the electron plasma wave is damped, it causes heating of the plasma. The two plasmon instability is a related process and occurs at $n_e \approx \frac{n_c}{4}$ and is the decay of a photon into two plasma waves, with $\omega_L = \omega_{p1} + \omega_{p2}$ [9, 34].

2.1.4 Laser Absorption

Collisional Heating

Collisional heating dominates laser absorption in plasmas at low intensities ($I < 10^{14}\mathrm{Wcm}^{-2}$) . Inverse bremsstrahlung involves the absorption of a photon by an electron during a collision with an ion or another electron. Ion - electron collisions dominate with a collision frequency given by [35]:

$$\nu_{ei}^{-1} = \tau_{ei} = \frac{3}{4}\frac{(k_B T_e)^{\frac{3}{2}} m_e^{\frac{1}{2}}}{(2\pi^{\frac{1}{2}}) Z^2 e^4 n_i \ln(\Lambda)} \approx 3.44 \times 10^5 \frac{T_e^{\frac{3}{2}}(eV)}{Z^2 n_i \ln(\Lambda)} \tag{2.8}$$

where T_e is the electron temperature, n_i is the ion density, Z is the ionisation and $\ln(\Lambda) = \ln \frac{\lambda_D}{l_{min}}$, and is known as the Coulomb logarithm, which for typical laser plasma conditions is such that $\ln(\Lambda) < 10$ (e.g for conditions $T_e = 10\mathrm{eV}{-}1\mathrm{keV}, n_e = 10^{19}\mathrm{cm}^{-3} - 10^{23}\mathrm{cm}^{-3}$) [9]. Here λ_D is the plasma Debye length, the minimum distance over which electrons will screen out an electric field and hence the maximum distance to consider for an electron - ion collision. l_{min} is the minimum impact parameter - the minimum approach distance between an electron and an ion during a collision, usually determined by the De Broglie wavelength of the electron. Collisional absorption occurs at densities up to the critical electron density and up to a distance from the critical density given by the the collisional skin depth $\delta_{ei} = \frac{c}{\omega_p}\sqrt{|1 + i\nu_{ei}|}$ [32].

Collisional heating is responsible for the bulk thermal temperature of the plasma. As the temperature of the plasma increases the collision frequency will drop. This means as the intensity of the laser increases the amount of collisional absorption will decrease and will drop off rapidly at intensities of $\approx 10^{15}$Wcm^{-2} [32].

Resonance Absorption

Above intensities of 10^{14}Wcm^{-2}, resonance absorption can be significant if the electric field of the laser has a component in the direction of the density gradient of the target and is obliquely incident onto the target. At an oblique angle of incidence, light will penetrate through to a density of $n_e = n_c \cos^2\theta$. At the turning point density, $n_c \cos^2\theta$, the electric field can tunnel through to the critical surface where an electron plasma wave is resonantly excited. If the laser polarisation is such that the electric field is directed along the density gradient, the oscillating electric field at the critical density drives electrons to higher or lower electron densities where the energy is strongly absorbed as they are oscillating at a frequency away from the plasma frequency. If the polarisation is perpendicular to the density gradient, there is little absorption as the electrons oscillate at the plasma frequency.

The fraction of absorption (A_f) is dependant on the component of the electric field along the density gradient (giving a $\sin(\theta)$ dependence) and the plasma density scale length l_{ne} and can be described simply by [34]:

$$\phi(\tau) = 2.3\tau \exp\left(-\frac{2\tau^3}{3}\right) \tag{2.9}$$

$$A_f = \frac{\phi(\tau)^2}{2} \tag{2.10}$$

where $\tau = \left(\frac{\omega_L l_{ne}}{c}\right)^{\frac{1}{3}} \sin(\theta)$. Fig. 2.3 shows a plot of the absorption fraction verses τ. A peak in absorption at $\tau = 0.8$ can be observed. This corresponds to a peak angle of resonance absorption, given by $\sin(\theta) = 0.8\left(\frac{c}{\omega_L l_{ne}}\right)^{\frac{1}{3}}$

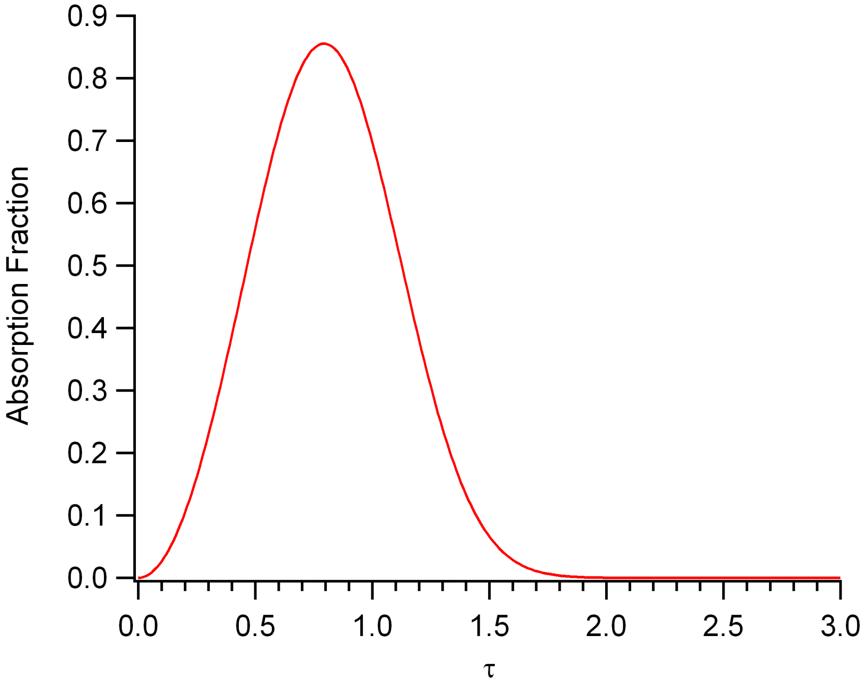

Figure 2.3: Fraction of laser absorbed via resonance absorption as a function of τ. Here $\tau = \left(\frac{\omega_l l_{ne}}{c}\right)^{\frac{1}{3}} \sin{(\theta)}$, following the theory of Kruer [34]

With steep density gradients and intensities approaching $10^{16}\mathrm{Wcm}^{-2}$, anomalous resonance absorption, also called vacuum or Brunel heating, can occur. This mechanism causes electrons to be dragged out of the plasma by the electric field into the vacuum and then oscillated across the vacuum - plasma boundary by the oscillating electric field. This mechanism increases the absorption of the laser when density gradients are very steep, see [36, 37]. Critical surface rippling which will vary the angle of the laser incidence can also have an effect on resonantly absorbed radiation [34].

2.1.5 Energy Transport

Thermal energy transport enables heat to flow into the higher density regions of the target (see Fig 2.2). Assuming a gentle temperature gradient where the mean free path of an electron $\lambda_{mfp} \ll \frac{T_e}{|\nabla T_e|}$ the heat flow into the target can be approximated by a diffusive equation with Spitzer -

Harm conductivities. Spitzer - Harm conductivities are calculated assuming a nearly Maxwellian distribution of electron energies. The Spitzer - Harm heat flux can be written [35]:

$$Q_{SH} = -\kappa_{th} \frac{\partial k_B T_e}{\partial z} \tag{2.11}$$

where κ_{th} is the classical plasma thermal conductivity given by [9]:

$$\kappa_{th} = \left(\frac{8}{\pi}\right)^{\frac{3}{2}} \frac{(k_B T_e)^{\frac{5}{2}}}{Z e^4 m_e^{\frac{1}{2}} \ln \Lambda} \tag{2.12}$$

where $\ln \Lambda$ is the Coulomb logarithm. The diffusion approximation will break down as temperature and density gradients increase, and can only be considered accurate when the density scale length l_{ne} and collisional mean free path λ_{mfp} are such that $\frac{l_{ne}}{\lambda_{mfp}} \gg 50$ [38]. For many laser plasma applications this condition is not satisfied.

For a more accurate model of electron energy transport in plasmas with steep density and temperature gradients, a full Fokker - Planck model of the electron distribution is required to account for non - local transport. The Fokker - Planck equation describes the temporal and spatial evolution of the electron distribution function. An example of a Fokker - Planck calculation is given by Bell [38]. The Fokker - Planck calculations are often simplified by several assumptions. For example in [38] the electron distribution function in phase space is expressed as an expansion of Legendre polynomials. Usually electron - ion energy exchange is ignored as the ion heat capacity will be a factor of Z lower for the cold ions than the electrons. The resulting expressions are then solved numerically by an iterative procedure. Other examples of Fokker Planck models are given, for example, in Davies et al [39] and Bell and Kingham [40].

Fokker - Planck calculations can be very expensive to include in fluid simulations. A flux limited heat transport model is often used in laser plasma interaction modelling. Here the maximum possible free streaming flux of electrons within the plasma is multiplied by a flux limiting factor f, such that the flux limited heat flow rate is given by:

$$Q_{FS} = f n_e k_B T_e v_{Th} \tag{2.13}$$

where v_{Th} is the thermal velocity of the electrons, and f has a typical value of $0.03 \leq f \leq 0.1$ [41, 42].

The free streaming flux is combined with the Spitzer - Harm flux to give the total heat flux, Q. These can be combined in several ways within simulations ,for example by calculating the harmonic mean of the two fluxes, $\frac{1}{Q} = \frac{1}{Q_{SH}} + \frac{1}{Q_{FS}}$, or by taking the minimum value of the two fluxes. The value of the flux limiter f has recently become an issue for the modelling of x-ray production from holhraum walls in indirect drive fusion on NIF. Discrepancies between expected amounts of Raman scattered light and drive, and asymmetrical implosions were observed. It was found to be necessary to use a greater value of flux limiter $f = 0.15$, as opposed to the lower value of $f = 0.05$ used previously, in order to produce lower plasma temperatures due to increased electron heat conduction. Asymmetric implosions can be caused by increased resonance absorption of the laser beams in cooler plasma, particularly in the beams focused further in the hohlraum (see the discussion on hohlraums in section 1.1.1) [43, 44]. These problems indicate some of the issues surrounding flux limited transport which is studied further in chapter 5.

2.1.6 Hot Electron Production

Collective processes such as resonance absorption, vacuum heating and parametric instabilities can produce a population of electrons with energies much greater than the thermal electron temperature. These hot electrons oscillate at the laser frequency and are accelerated to high energies. Usually the hot electron population is assumed to have a Maxwellian form due to electron - electron collisions so that the electrons appear as a higher temperature tail to the the thermal electron temperature distribution.

Hot electron temperature scaling laws relevant to the intensities used in this work are as follows [32]. Assuming resonance absorption, for intensities $I\lambda^2 < 10^{17}\text{Wcm}^{-2}\mu\text{m}^2$ and density scale lengths $\frac{l_{ne}}{\lambda_L} > 1$ we have following Forslund, Kindel and Lee (1977) [45] that:

$$T_{hot}(keV) = 14\left(T_{e\,keV}\left(\frac{I}{10^{16}\text{Wcm}^{-2}}\right)\lambda_{\mu m}^2\right)^{\frac{1}{3}} \tag{2.14}$$

where T_{ekeV} is the electron temperature in keV and I is the laser intensity in units of $10^{16}Wcm^{-2}$. For intensities $I\lambda^2 < 10^{17}$ and density scale lengths $\frac{l_{ne}}{\lambda_L} < 0.1$, Gibbon and Bell (1992) [37] suggests:

$$T_{hot}(keV) = 7\left(\left(\frac{I}{10^{16}\text{Wcm}^{-2}}\right)\lambda_{\mu m}^2\right)^{\frac{1}{3}} \tag{2.15}$$

The factor $I\lambda^2$, arises because the velocity of the electron oscillation in an electric field (the quiver velocity) is proportional to $\left(I\lambda^2\right)^{\frac{1}{2}}$ making $I\lambda^2$ a common scaling which is frequently used as a normalised irradiance wherever the electron quiver velocity is involved [46, 47]. For example the electron quiver velocity is given by [32, 46]:

$$\frac{v_{os}}{c} = \frac{eE}{m\omega c} = 0.84\left(\left(\frac{I}{10^{18}\text{Wcm}^{-2}}\right)\lambda_{\mu m}^2\right)^{\frac{1}{2}} \tag{2.16}$$

where v_{os} is the quiver velocity.

At high irradiances ($I\lambda^2 > 10^{17}\text{Wcm}^{-2}\mu\text{m}^2$) electrons can be directly accelerated in the direction of a laser pulse by the $\overline{\boldsymbol{J}} \times \overline{\boldsymbol{B}}$ Lorentz force due to the electron velocity in the laser $\overline{\boldsymbol{E}}$ direction causing a $\overline{\boldsymbol{V}} \times \overline{\boldsymbol{B}}$ acceleration, where $\overline{\boldsymbol{B}}$ is the laser magnetic field. Gradients of laser intensity also produce electron acceleration to lower intensity due to the uneven oscillation of electrons. These electron acceleration mechanisms are generally referred to as pondermotive accelerations. Accelerated electrons may thermalise to produce a hot electron distribution.

Hot electrons propagate rapidly through a target heating it before thermal conduction occurs. Hot electron production can be an issue in inertial confinement fusion where hot electrons produced during the ablation of the fuel preheat the centre reducing compression efficiency. In fast ignition, however, hot electrons are used to ignite the already compressed fuel [48]. Understanding hot electron production also has applications in ion acceleration [49] and x-ray source production [50].

2.2 Thermodynamic Equilibrium Population Relations

Complete thermodynamic equilibrium requires the radiation field, and the population of ions and electrons to be in equilibrium. The small scale of laser produced plasmas usually results in the electromagnetic radiation being out of equilibrium with the particles. However, if collisional populating processes dominate radiation processes, then the populations of different quantum states can be described by equilibrium relationships and the condition of local thermodynamic equilibrium (LTE) applies. As local thermodynamic equilibrium applies where rates of collisional processes dominate over radiative rates, high electron densities are required.

Assuming a plasma is in LTE allows the calculation of populations of ionised and excited states given a known temperature and electron density using the Saha and Boltzmann equations. The population distribution for excited states in LTE is given by the Boltzmann ratio:

$$\frac{N_j}{N_i} = \frac{g_j}{g_i} \exp\left(-\frac{E_j - E_i}{k_B T_e}\right) \tag{2.17}$$

where N_i and N_j are the lower and upper states, g_i and g_j are the lower and upper state degeneracies and E_j and E_i are the state energies.

Population ratios of different ionisation states can be found as follows: the Boltzmann equation for an neutral atom and the first ionised state is:

$$\frac{dN_{q+1}}{N_q} = \frac{g}{g_q} \exp\left(-\frac{I_{pi} + \frac{1}{2}m_e v^2}{k_B T_e}\right) \tag{2.18}$$

where dN_{q+1} is the differential number of ions in the ground state with free electrons in the velocity range $v, v + dv$ with kinetic energy $\frac{1}{2}mv^2$. N_q is the number of ground state atoms, $g = g_e g_{q+1}$ where g_e is the free electron degeneracy and g_{q+1} is the ground state ion degeneracy. I_{pi} is the ionisation energy. g_e is the number of degenerate electrons within a small momentum interval $p, p + dp$, and is given by:

$$g_e = \frac{2V\Delta p^3}{h^3} \tag{2.19}$$

where V is the volume per electron and p is the momentum. V can be assumed to be $\frac{1}{n_e}$, the factor of 2 accounts for the 2 spin states of the electrons. Using $\Delta p^3 = 4\pi m_e^3 v^2 dv$, and substituting for g_e, 2.18 becomes:

$$\frac{dN_{q+1}}{N_q} = \frac{g_{q+1}}{g_q}\frac{8\pi m_e^3}{h^3 n_e} \exp\left(-\frac{I_{pi} + \frac{1}{2}m_e v^2}{k_B T_e}\right) v^2 dv \tag{2.20}$$

Integrating over the velocity and substituting for the constants we obtain [51]:

$$\frac{N_{q+1}}{N_q} n_e = \frac{g_{q+1}}{g_q}\frac{1}{4a_B^3}\left(\frac{k_B T_e}{\pi E_H}\right)^{\frac{3}{2}} \exp\left(-\frac{I_{pi}}{k_B T_e}\right) \tag{2.21}$$

where a_B is the Bohr radius and E_H is the hydrogen ground state ionisation energy. To derive the population of states from a given electron density and temperature, an iterative procedure to find populations of each ionisation state can then be used with an initial estimate for the ground state population and the condition that the sum of the number of electrons from each ion state should equal the total electron density, i.e :

$$n_e = \sum_{Z=0}^{Z_{max}} N_Z Z \quad . \tag{2.22}$$

If more than one type of atom is present the extra condition is required that the ratio of the total number of ions of each species is the same as the atomic ratio $\frac{A_A}{A_B}$.

$$\frac{A_A}{A_B} = \frac{\sum_{Z=0}^{Z_{max}} n_{ZA}}{\sum_{Z=0}^{Z} n_{ZB}} \quad . \tag{2.23}$$

For aluminium oxide, for example this is $\frac{2}{3}$. This method of finding ionisation populations is used to calculate the bound - free absorption coefficient discussed in the next section.

2.3 Plasma Opacity

The intensity of radiation travelling a distance x through a material is given by Beer's law (2.24):

$$I = I_0 \mathrm{exp}\left(-\int \sigma\rho dx\right) \tag{2.24}$$

where σ is the opacity, ρ is the density, I and I_0 are the final and initial radiation intensities respectively. The integral $\int dx$ is over the distance travelled through the material. The exponential exp $\left(-\int \sigma\rho dx\right)$ is the transmission, the integral $\int \sigma\rho dx$ is known as the optical depth (τ_ω) and $\sigma\rho$ is referred to as the absorption coefficient α. Where the optical depth, $\tau_\omega >> 1$ a plasma is described as optically thick with a large number of photons being absorbed. If $\tau_\omega << 1$, it is optically thin and few photons will be absorbed as they travel through the plasma.

The opacity defines the transparency of a material to electromagnetic radiation and quantifies the amount of energy transmitted by photons through a plasma. Radiative transfer is affected by both scattering and photo-absorption processes, and is usually a strong function of the photon energy. Photo-absorption includes discrete line absorption from bound - bound transitions of electrons within atoms, and absorption processes, where the final state of the electron is in the continuum. Such processes include free - free transitions such as inverse bremsstrahlung, and bound - free transitions such as photo-ionisation. Fig. 2.4 compares photo-absorption coefficients from free - free, bound - free and bound - bound absorption for Al at a temperature of 10eV and an ion density of $10^{20}cm^{-3}$ between 1 and 100eV.

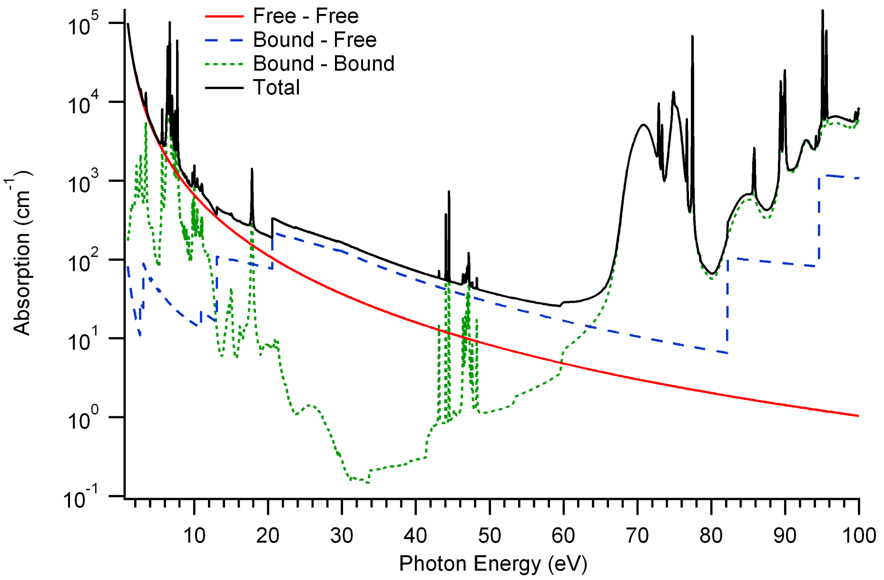

Figure 2.4: Comparison of photo-absorption processes as a function of frequency for Aluminium between 1 and 100eV, at an electron temperature of 10eV and an ion density of 10^{20}cm^{-3}. Free - free absorption is shown by the red continuous line, bound-free by the dashed blue line and bound-bound by the dotted green line. The total absorption coefficient is given by the black continuous line. Data is taken from FLYCHK [52].

Thomson scattering also reduces the intensity of a beam of photons when an electron (not in the electric field of an ion) absorbs and then emits a photon in a different direction [14]. If the scattering electron moves at a velocity close to the speed of light, then the relativistic effect can cause a frequency shift of the scattered radiation from a free electron and the process is known as Compton scattering. Thomson and Compton scattering is independent of frequency, and is only significant at very high temperatures where photo absorption coefficients are low. The Thomson scattering opacity is given by $\sigma_{TS} = 0.4\frac{Z}{A}\mathrm{cm}^2\mathrm{g}^{-1}$, where A is the atomic mass [9].

2.3.1 Free - Free Absorption

Free - free or inverse bremsstrahlung absorption involves the absorption of a photon by an electron in the electric field of an ion. This ion is required to ensure momentum is conserved. Inverse bremsstrahlung has a continuous absorption spectrum due to the final state of the electron being in the continuum, with a frequency dependence of $\frac{1}{\nu^3}$ as is shown in equation 2.25. The expression for the free - free absorption coefficient,α_{ff}, is given by [53].

$$\alpha_{ff} = \frac{4e^6}{3m_e hc}\sqrt{\left(\frac{2\pi}{3m_e k_B T_e}\right)} n_e \nu^{-3}\left(1 - \exp\left(-\frac{h\nu}{k_B T_e}\right)\right) n_i Z_i^2 \overline{g}_{ff} \tag{2.25}$$

where ν is the photon frequency, T_e is the electron temperature, Z is the ion charge, $\overline{g}_{ff}$ is the free - free Guant factor, a quantum mechanical correction factor usually assumed to be ≈ 1. n_i and n_e are the ion and electron densities respectively. Free - free absorption dominates at photon energies of a few eV, below the lowest bound electron absorption edge and where ions are highly ionised with few or no bound electrons [54].

2.3.2 Bound - Free Absorption

Bound - free absorption is the absorption of a photon by an electron within an atom with energy greater than or equal to the ionisation energy and is also known as photo-ionisation. Like free - free absorption, the final state of the absorbing electron is in the continuum resulting in a continuous absorption spectrum characterised by “jumps” in the absorption at ionisation energies - the points where photon have an energy equal to the ionisation energy for a given ion or atom. The expression given below consists of two parts: the first the energy absorbed by ground state electrons and the second the contribution by electrons in excited states. The total absorption coefficient is the sum of the absorption coefficient from all energy levels over all ionisation states and can be written:

$$\alpha_{bf} = \frac{4e^6}{3m_e hc}\sqrt{\left(\frac{2\pi}{3m_e k_B T_e}\right)} n_{eZ}\nu^{-3}\left(1-\exp\left(-\frac{h\nu}{k_B T_e}\right)\right)\sum_{Z=0}^{Z_{max}} n_{iZ}Z^2 \left[\overline{g}_n \frac{\zeta}{n^3}\frac{I_{pZ}}{k_B T_e}\exp\left(\frac{I_{pZ}}{k_B T_e}\right) + \sum_{m=n+1}^{\infty}\overline{g}_m \frac{2Z^2 R_y}{m^3 k_B T_e}\exp\left(\frac{Z^2 R_y}{m^3 k_B T_e}\right)\right] \quad (2.26)$$

where I_{pi} is the ground state ionisation energy, R_y is the Rydberg energy, ζ is the number of electrons in the groundstate n, where n is the ground state principle quantum number, and $\overline{g}_n$ and $\overline{g}_m$ are gaunt factors. n_{iZ} and n_{eZ} are the ion and electron densities of an ionisation state Z.

In equation 2.26 g_n = 0, when I_{pZ} is less than the photon energy. Likewise g_m = 0, when $\left(\frac{Z^2 R_y}{m^3}\right)$ is less than the photon energy. Calculated values of factors as a function of photon energy for all electronic shells are tabulated in Karzas and Latter [55]. These values are used later in this thesis (Chapter 6). At high densities, continuum lowering will cause a reduction in the binding energy of the electrons due to higher electron states being shifted in to the continuum. Continuum lowering is caused by the perturbing effects on the atomic potential by nearby free electrons and ions [54].

2.3.3 Bound - Bound Absorption

Bound bound absorption is the absorption of a photon by a bound electron which is then excited to a higher energy bound state. This results in discrete line absorption, with the absorbed photon having the same energy as the difference in energy between the two bound states. The bound

bound absorption coefficient is given by:

$$\alpha_{bb} = 2\pi^2 \frac{e^2}{m_e c^2} \hbar c \frac{g_j}{g_i} N_i f_{ji} L(\hbar\omega) \tag{2.27}$$

where g_i and g_j are the degeneracies of the upper and lower states respectively, N_i is the lower state population, f_{ji} is the transition oscillator strength and $L(\hbar\omega)$ is the line shape function. In higher Z elements the large number of possible transitions can result in quasi-continuum absorption where absorption lines broadened by processes such as Doppler and pressure broadening at high density merge into unresolved transition arrays. Modelling bound - bound absorption, particularly for high Z materials can be difficult due to the large number of possible transitions over a range of different ionisation stages.

Line Shapes

Discrete line absorption will have a natural line width derived from the uncertainty principle, whereby a state with a given finite lifetime τ_L, will have an associated uncertainty in its energy ΔE, given by $\Delta E \tau_L = \frac{\hbar}{2}$ The shape of the spectral line is then determined by the lifetime of the upper state, resulting in a Lorentzian line shape given by [54]:

$$L(\omega) = \frac{1}{\pi\tau_L} \frac{1}{(\omega - \omega_0)^2 + \left(\frac{1}{\tau_L}\right)^2} \tag{2.28}$$

where ω_0 is the central line frequency. The full width half maximum (FWHM) is then given by $\frac{2}{\tau_L}$. This broadening is generally much lower than other forms of broadening in plasmas.

Doppler broadening is caused by the thermal motion of the emitting ions in the plasma and the Doppler shift due to ion motion in the direction of observation. This can be a significant broadening mechanism in lower density plasmas and can be used to determine the ion temperature

T_i, if it is the main factor that effects line width. The line shape is Gaussian when the ion velocities are assumed to be a Maxwellian with a line shape:

$$L(\omega) = \frac{1}{\sqrt{\pi}\omega_D} \exp\left[-\left(\frac{\omega - \omega_0}{\omega_D}\right)^2\right] \tag{2.29}$$

where $\omega_D = \sqrt{\left(\frac{2k_B T_i}{m_i c^2}\right)}\omega_0$ is the Doppler broadened linewidth, and m_i is the ion mass. The FWHM of the linewidth is given by $2\sqrt{\ln 2}\omega_D$.

Pressure broadening is significant in higher density plasmas and can be caused by collisions of absorbing ions with electrons while radiation is being emitted. This has a Lorentzian form similar to that of natural broadening with the state lifetime replaced by the time between collisions. Another cause of pressure broadening is related to the Stark effect, whereby the electric potentials of nearby ions perturb the potential of the absorbing ion. This broadening effect is often used to make measurements of ion densities, but is only applicable for lines where the linear Stark effect can occur, usually H - like and He - like lines.

2.3.4 Mean Opacities

The opacity of a material is usually strongly dependent on the frequency of the radiation. In some cases frequency averaged mean opacities can be used. One such method of averaging opacity over frequency is the Rosseland mean opacity which averages the opacity over the temperature derivative of the Planck radiation distribution. This average applies under optically thick conditions where a diffusive approximation for radiative transfer is valid (see chapter 1). For radiative diffusion, the mean free path of the radiation needs to be much less than the characteristic length of the system. The Rosseland mean opacity σ_R is evaluated using [56]:

$$\frac{1}{\sigma_R} = \frac{\int\limits_0^\infty d\nu \frac{1}{\sigma(\nu)} \frac{dB_\nu}{dT}}{\int\limits_0^\infty d\nu \frac{dB_\nu}{dT}} \tag{2.30}$$

where B_ν is the Planck radiation distribution, T is the temperature and ν is the frequency. Rosseland averaging has the effect of weighting the average of the opacity at the frequencies where the radiative flux is greatest, i.e. at the peak of $\frac{dB_\nu}{dT}$. This mean is used, for example, in stellar interiors [15] and in indirect ICF, in a hohlraum wall [10]. In the solar convection zone the peak of $\frac{dB_\nu}{dT}$ is in the EUV / soft x-ray region around 300 - 1300eV [17] making EUV opacities significant in understanding energy transport in the sun.

The absorbed blackbody radiation P_{abs}, within a uniform optically thin plasma of thickness Δx, and opacity as a function of frequency σ_ν, is given by:

$$P_{abs} = \int\limits_0^\infty B_\nu d\nu - \int\limits_0^\infty B_\nu \exp\left(-\sigma_\nu \rho \Delta x\right) d\nu \tag{2.31}$$

so

$$P_{abs} \cong \left[\int\limits_0^\infty B_\nu \sigma_\nu d\nu \right] \rho \Delta x \tag{2.32}$$

Consequently, for an optically thin plasma, for example within a stellar atmosphere, the relevant frequency averaged opacity is averaged over the Planck function itself, such that:

$$\sigma_P = \frac{\int\limits_0^\infty d\nu\, \sigma_\nu B_\nu}{\int\limits_0^\infty d\nu\, B_\nu} \tag{2.33}$$

The power absorbed per unit area in a thin layer becomes:

$$P_{abs} = \sigma_p \rho \Delta x \sigma_{SB} T^4 \tag{2.34}$$

as $\int_0^{\infty} B_\nu d\nu = \sigma_{SB} T^4$ where σ_{SB} is the Stefan - Boltzmann constant.

2.3.5 Opacity Measurements

A large number of experiments aimed at making measurements of plasma opacities using a variety of different methods have taken place. The main principle behind a large proportion of the measurement techniques is to measure the transmission through a sample under known conditions which can then be compared to opacity models under the same conditions. The sample is ideally spatially uniform in both temperature and density. With high density plasmas, good time resolution is often required due to the rapid changes in sample conditions and therefore, the opacity with time due to plasma expansion and heat transport [57].

The target of the material for an opacity measurement has often been a thin foil with a typical thickness of 10 - 100 nm, within a plastic tamp layer and mounted on a substrate. This tamp often made of a plastic, acts to slow down the rate of expansion of the heated foil and so improves the uniformity and increases the density at the time of measurement [2, 58, 59]. The foil is heated, typically, by x -ray radiation from a second foil also heated by a laser pulse. This x-ray source is made of gold or another high Z material (for example [2]) in order to maximise the flux of emission, though some experiments have used hohlraums (for example [60]). X-ray heating of opacity samples produce uniform heating of the sample material due to absorption over the attenuation length of the x-rays.

Short pulse lasers (pulse lengths of $<$ 0.1ps - 100ps) have also been used to heat foils for opacity measurements. If the heating beam is absorbed by a tamp layer, the foil is heated by conduction and temperatures up to 100s of eV can be produced in an opacity sample [58, 61, 62]. However, the maximum temperatures that can be examined with transmission measurements of opacity is limited by the need for a backlighter to be brighter than the self - emission from the opacity sample.

A large number of experiments have taken place where the transmission of radiation through a heated foil is measured using a broadband emission source from a heated foil backlighter. Backlighter materials are chosen so that they have a relatively featureless or continuous spectrum over the region of interest. This is more likely for high Z materials which also emit more strongly. Balmer et al (1989) [57] compared different backlighters probing an aluminium sample, from low Z aluminium to higher Z titanium and ytterbium, and found improved spectral resolution with the higher Z materials. High Z materials can have a quasi-continuous spectrum due to the broadening of large numbers of closely spaced lines. Examples of materials commonly used include gold at lower photon energies (50 - 350eV) [2, 60, 63], silver at slightly higher (720 - 760eV) [64] and rare - earth, such as samarium or neodymium, coated wires at high photon energies (1100 - 1700eV) [60, 65, 66]. The first of these types of experiments started in the late 1980s using samples of Al, Fe and Ge at temperatures of 15 - 76eV and densities of $\sim 10^{-2}$gcm^{-3} [57, 59, 66].

Using backlighters of short duration 10 - 100ps improves the time resolution within the data and ensures a more uniform plasma during the time of the transmission measurement. Usually the transmitted backlighter intensity is measured with a spectrometer, the emission from the backlighter itself also needs to be measured, either on a separate shot without the foil in place (as long as the conditions are reproducible) or by using a point projection backlighter method where both spectra are measured in a single shot insuring the conditions are the same (for example [2, 57]).

If the nominally continuous backlighter spectrum is made up of a large number of closely spaced emission lines broadened in to a quasi-continuum, problems can occur if there is structure present that cannot be resolved within the instrumental resolution. Errors in the measurement of transmission through the material will arise [67]. Saturation effects occur where the total transmitted intensity stops decreasing exponentially with optical depth or distance through the foil. This effect is dependent on the relative line widths of the backlighter emission and plasma absorption features and is greatest when the width of emission peaks in the backlighter are greater than the width of the absorption peaks in the sample [67]. For a discussion of saturation effects for a variety of possible conditions and line profiles, see [68].

The self emission of the target can place constraints on the temperatures and densities of the material examined. It is important that the backlighter is brighter than the opacity target self - emission. This has been achieved using EUV lasers as backlighters [58]. Plasma based Ni-like silver EUV lasers been been used to probe an iron plasma at temperatures and densities of $30-350$eV and $0.001-0.2$gcm^{-3} [58], in order to measure the transmission of a short pulse laser heated iron. Neon - like Zn and Y lasers have also been used to measure ablation rates of laser heated materials [69], and the imprinted modulations in transmission due to the Rayleigh -Taylor instability respectively [70]. Ne-like Ge and Ni plasma based EUV lasers have also previously been used to measure transmission through solid aluminium at photon energies of 53.7 eV and 63.3 eV [71].

There have also been a series of experiments using z - pinches [3, 72], which are bright sources of x-rays. Here foils are heated by the x-rays produced by the early stages of the z - pinch collapse of a dynamic hohlraum beneath the sample. The backlighter is formed by the collapsing Z pinch at late times when material stagnates on the axis. This measurement has enabled opacities at 156eV over a range of photon energies from $800-1800$eV [3] to be measured. The dynamic hohlraums have an advantage of producing blackbody radiation emission and, if temperatures are great enough, are able to overwhelm the self emission of the high temperature sample.

An alternative method of opacity measurement is to heat the target and measure the emission. Assuming it is in LTE, Kirchhoff's law gives the opacity. This method was first described by Nazir et al (1996) [62] and has the advantages of being able to make measurements at higher temperatures and densities, which are difficult with backlighters as the self emission from the target can be brighter than the transmitted backlighter emission. Recent work using this method has been performed at AWE by Hoarty el al [61, 73] with sample temperatures of 800 ± 100eV and mass densities of 1.5 ± 05gcm^{-3} observed [61].

It has also been suggested in Wagenaars et al (2010) that multiple high-order harmonics could be used to probe opacities over a wide enough photon energy range in a single shot to provide an estimate of frequency averaged mean opacities for low temperature plasmas (due to self emission increases from higher temperature samples and the maximum likely intensity of high harmonics). Assuming that the temperature of the sample is known to a 10$\%$ accuracy, potential accuracies of mean opacities of $\approx 20\%$ based on high harmonic probing of a 10eV electron temperature and 0.008gcm^{-3} mass density iron plasma are expected [74].

2.3.6 Opacity Models

A commonly used method to calculate opacity is the average atom model which ignores detailed atomic structure and is based on the most likely atom given the statistical averages of ionisation and excitation within the plasma. Detailed configuration accounting (DCA) includes atomic structure up to LS coupling, but does not include detailed term splitting. This method is often combined with the unresolved transition array (UTA) method for large numbers of bound electrons. UTA does not include detailed line shapes, instead the detailed term structure is assumed to be closely spaced as to overlap and form a single line with a Gaussian line shape often assumed. Detailed term accounting (DTA) is the most computationally intensive method using all possible transitions and requires detailed line shapes, making this more suitable for lighter elements.

The possible variation between opacity models run for iron under the same conditions can be seen in a summary of the 1997 opacity workshop held in Madrid [75]. Several opacity workshops have been held in order to compare results from different opacity models, with the 1997 workshop comparing Rosseland and Planck mean opacities calculated with 15 or more different models for iron under different conditions. In some cases, variations in opacities of over an order of magnitude are observed [75]. It was found that agreement increased as density increased up to 0.1gcm^{-3}. As densities were increased further above this codes began to disagree again. Experimental data can help distinguish between codes where they disagree. Where there is agreement, this could be caused by codes using the same approximations. Experiments are needed to check whether these approximations are valid [75].

Astrophysical models [25, 76] use theoretical opacity data such as the Opacity Project or OPAL (LLNL) tables. These two sets of data generally show good agreement with each other [21, 28]. These tables give values of Rosseland mean opacity for an astrophysical mixture of elements, usually derived from the measured solar abundances of elements.

This thesis uses a DCA and UTA code, called the Ionised Materials Package (IMP) [77] developed by S. Rose. Two sets of IMP data are used. An original IMP and Improved IMP. These differ as original IMP [77] data uses ion configurations based on placing quantum shells in one of 3 groups. Core shells are assumed to be fully occupied. Rydberg shells are assumed to be empty with 1 valence shell which has a varying level of occupation. The improved IMP data has several additions [78] including a greater number of possible atomic configurations which can contribute significantly to the opacity. The improved IMP data allows for ion configurations with up to 3 open valence shells with significant populations. Improved IMP opacity data used in chapter 5 is shown in Fig. 2.5.

Fig. 2.6 shows a simple model of iron opacity assuming that neutral iron has a tabulated [79] opacity per atom and calculating the opacity contribution associated with ionisation using equations 2.25 and 2.26 for ionised iron. The degree of ionisation is calculated using the Saha - Boltzmann equation (equation 2.21). This simple model shows a similar overall opacity structure to IMP opacity (compare figures 2.5 and 2.6), with lower values of opacity at higher temperatures due to the absence of bound - bound emission. A similar model is used to determine the opacity of aluminium at a photon energy of 45eV in chapter 6. The York Opacity Model [80], which is a DTA model using Opacity Project atomic data has also been used for comparison with IMP under specific conditions, this is discussed in chapter 5.

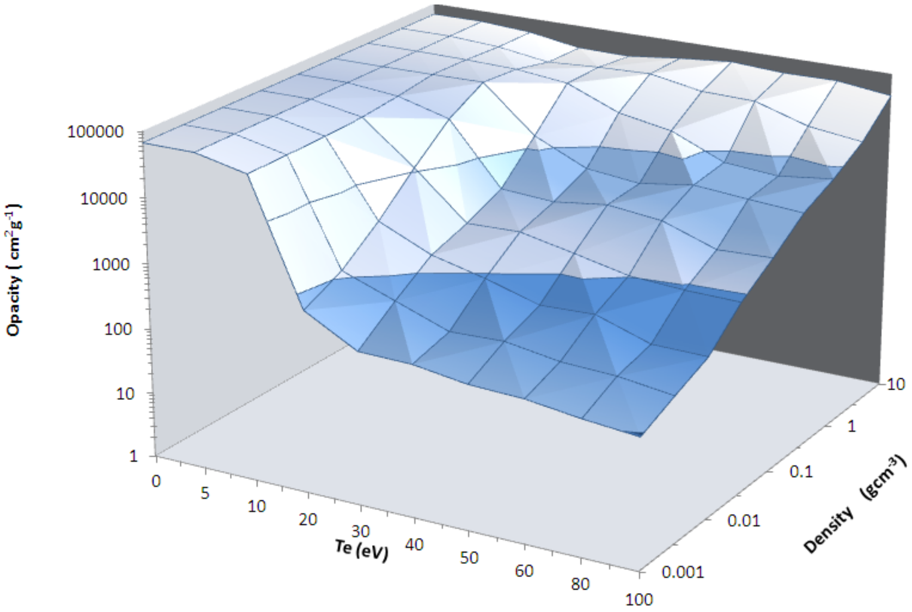

Figure 2.5: Improved IMP opacity of iron as a function of mass density and electron temperature at 13.9nm

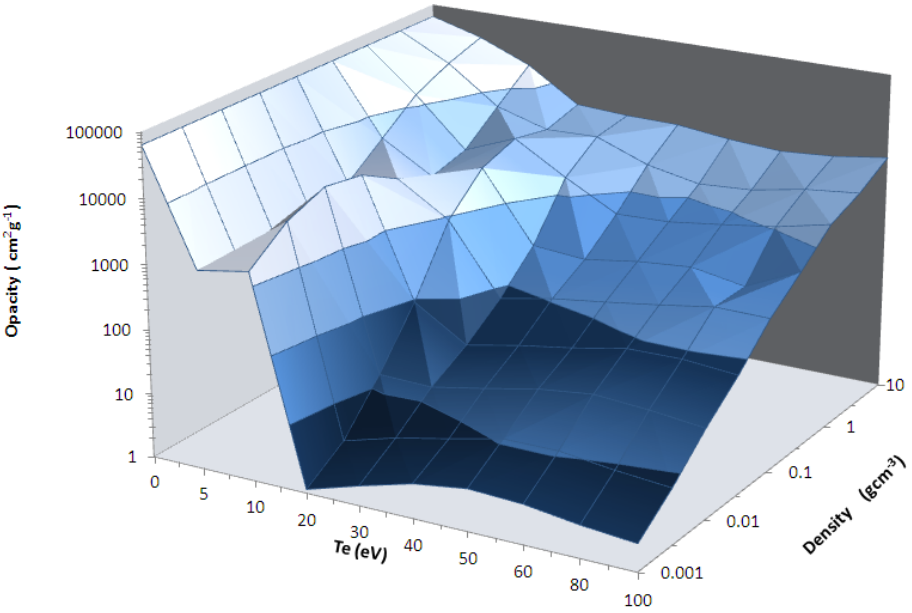

Figure 2.6: Opacity of iron calculated with free - free and bound - free absorption only, using a Saha - Boltzman distribution of ionised states as a function of mass density and electron temperature at 13.9nm

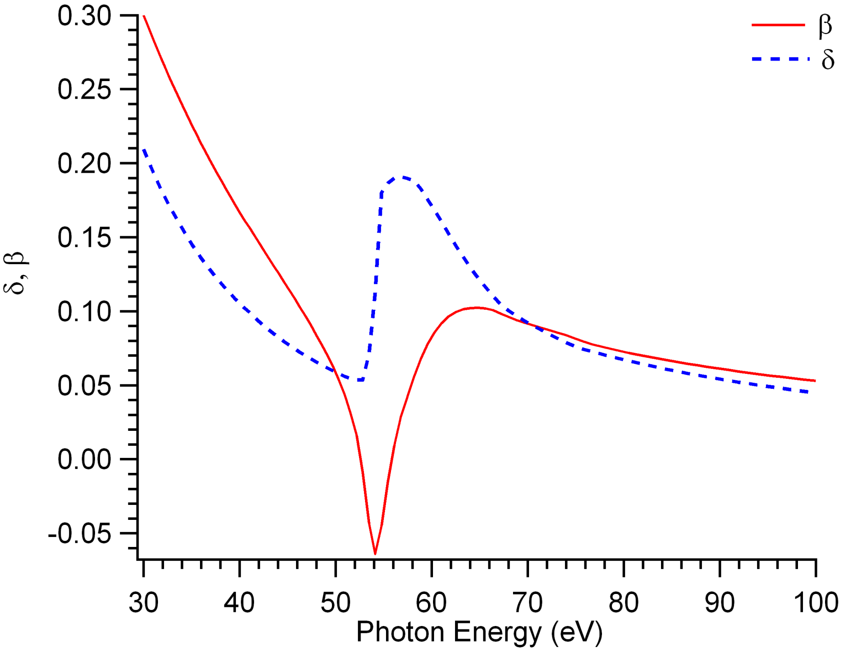

Figure 2.7: Complex refractive index of iron. Data taken from the center for x-ray optics database [79]

2.3.7 Calculating Plasma Refractive Indices

The refractive index of a material can be considered as a complex expression with a real part related to the electromagnetic phase shift and dispersion properties of a material and an imaginary part which describes the attenuation of electromagnetic radiation as it passes through a material and is related to the materials opacity. At EUV wavelengths almost all solid materials are opaque with attenuation lengths $< 1\mu$m, causing the imaginary refractive index component to become significant. We can express the refractive index in the form:

$$\eta(\omega) = 1 - \delta(\omega) + i\beta(\omega) \qquad (2.35)$$

where δ is the real part related to the phase shift and β is the imaginary part related to the material's opacity. An example of the complex refractive index components in the EUV region from 30eV - 100eV is shown in Fig. (2.7). EUV photon energies are comparable to the binding energies of inner shell electrons. Fig. (2.7) illustrates the rapid change in refractive index that occurs around absorption edges. In this example the feature at 52eV is the solid iron M2/M3 edge. These absorption edges occur when photons are above the binding energy of an electron within a given inner electron shell, in this case the M shell. This causes the photon to be absorbed and there to be a rapid increase in absorption for photon energies above the binding energy.

The complex refractive index can also be expressed as:

$$\eta(\omega) = 1 - \frac{n_a r_e \lambda^2}{2\pi} \left(f_1^0(\omega) - i f_2^0(\omega) \right) \tag{2.36}$$

where n_a is the atomic density, r_e is the classical electron radius, λ is the wavelength, and f_1 and f_2 are the real and imaginary parts of the scattering form factor [1].

These real and imaginary parts of the refractive index can be related via the Kramers - Kronig relationship, allowing one part of the refractive index to be determined indirectly if the other is known over a large range of the spectrum. Frequently this method is used to determine δ from measurements of β, as was done for example for the tabulated values of the aluminium refractive index given in Shiles et al.[81, 82] and the optical constants given by Henke et al. [83]. This method however, can lead to large errors in values of the real refractive index due to errors in the imaginary part, and can be an issue in particular around absorption edges where the refractive index changes rapidly. The Kramers - Kronig relationship is often used to express the real part of the scattering form factor as a function of the imaginary part using:

$$f_1^0(\omega) = Z^* - \frac{2}{\pi} P.V. \int_0^\infty \frac{u f_2^0(u)}{u^2 - \omega^2} du \tag{2.37}$$

where Z^* is the average ionisation, and P.V. indicates the principle value of the integration.

2.3.8 Plasma Refractive Index

The refractive index of a plasma due to free electrons is given by:

$$\eta(\omega)^2 = 1 - \frac{\omega_p^2}{\omega^2} \tag{2.38}$$

where ω_p is the plasma frequency. By substituting the plasma frequency with the critical density and assuming $n_e \ll n_c$, we get the plasma refractive index due to the free electrons as:

$$\eta(\omega) \cong 1 - \frac{n_e}{2n_c} \quad . \tag{2.39}$$

Within a partially ionised plasma, bound electrons can have a strong effect on the refractive index, with absorption edges and resonances dominating the refractive index [84, 85] and leading to plasma refractive indices > 1, as opposed to < 1 in a plasma where the free electron refractive index dominates. The contribution due to bound electrons can be described by [84]:

$$\eta(\omega) = 1 - f_1 \frac{n_i}{2n_c} \tag{2.40}$$

The value of f_1 can be calculated for a bound - free absorption edge at a photon energy E_β. We assume absorption with a typical profile above the edge proportional to ω^{-3} and note that the imaginary component of the form factor f_2 is related to the absorption coefficient by $\alpha = \frac{4\pi}{\omega} n_i c r_e f_2$, where r_e is the classical electron radius and ω is the photon angular frequency. Equation 2.37 can then be solved for this absorption profile to give:

$$f_1(\omega) = f_2\left(\tfrac{E_\beta}{\hbar}\right) \frac{1}{\pi} \frac{E_\beta^2}{(\hbar\omega)^2} \ln\left(\left|1 - \frac{(\hbar\omega)^2}{E_\beta^2}\right|\right) \quad . \tag{2.41}$$

This formula is used in the work discussed in chapter 6, to calculate the refractive index of a laser heated aluminium target.

2.4 Summary

This chapter has given the background theory to some of the work included in this thesis . Laser plasma interactions, plasma opacity, opacity modelling and experiments, the plasma refractive index and the Kramers - Kronig relationship have been introduced. The next chapter will discuss diagnostics and EUV sources relevant to the work in this thesis.

Chapter 3

EUV Sources, Diagnostics and a Fluid Simulation Code

The experimental techniques discussed in this thesis utilise extreme ultraviolet probing of materials. This chapter discusses the different sources of EUV radiation used throughout this work including, extreme ultraviolet lasers and high harmonic generation, along with potential sources for further work such as x-ray free electron lasers. The different diagnostics used to obtain data are also described along with a discussion of the radiative hydrodynamics code HYADES, used to simulate the experiments described in chapters 5 and 6.

3.1 EUV Radiation Sources

3.1.1 Plasma Based EUV Lasers

Lasing in the EUV region utilises high temperature (100eV - 1keV), high Z plasmas as the gain medium because electrons are able to be collisionally excited within a plasma to the high energy levels required for EUV emission. This form of laser has to operate with the laser radiation only taking a single pass through the gain region due to the short lifetime of the gain medium and the low efficiency and manufacturing difficulties of using EUV cavity and output mirrors. Using EUV lasers to measure transmission has the advantage that the high brightness radiation produced is able to overwhelm the self-emission of higher temperature and density plasmas (see chapter 2).

Plasma based EUV lasers typically have pulse lengths of greater than 1ps, with intensities of up to 10^{10}Wcm^{-2}, wavelengths down to 5.9nm [86] and bandwidths typically of $\frac{\nu}{\Delta\nu} = 10^3 - 10^4$ [87]. The plasma gain medium is created by focusing a low energy optical laser in a line on to a solid target, producing a pre-plasma with typical dimensions 1cm $\times 100\mu$m [87]. A short pump pulse is then focused into the pre-plasma. Short pulses are desirable due to the picosecond lifetime of the excited states. The pumped region can be moved along the length of the gain medium to increase emission as excited states have a short lifetime. The wavefront is moved in the direction of the EUV laser output by introducing a tilt in the pump pulse using a diffraction grating. The short pulse can enter the pre-plasma at grazing incidence (GRIP: Grazing incidence pumping) [87]. Using a grazing incident pump pulse improves the coupling of energy to the optimum gain region as the pumping pulse is reflected at a density below the critical density where the electron density is optimum for gain [88]. Use of a pre-pulse ensures that density gradients in the plasma are not steep at the time of the main pumping pulse. Inverse bremsstrahlung is then the main laser absorption process. In addition, refraction of the EUV laser beam is reduced leading to greater amplification in the plasma medium [87].

Population inversion is produced by collisions of free electrons with bound electrons which are then excited up to higher levels. In nickel and neon-like ions lasing occurs between 4d - 4p and 3p - 3s respectively [87]. For the case of Ni - like lasing, used in chapter 5, the 3d - 4d transition is radiative dipole forbidden and excitation can only occur via collisional excitation. This has a low transition rate, which helps achieve population inversion by reducing decay back to the ground

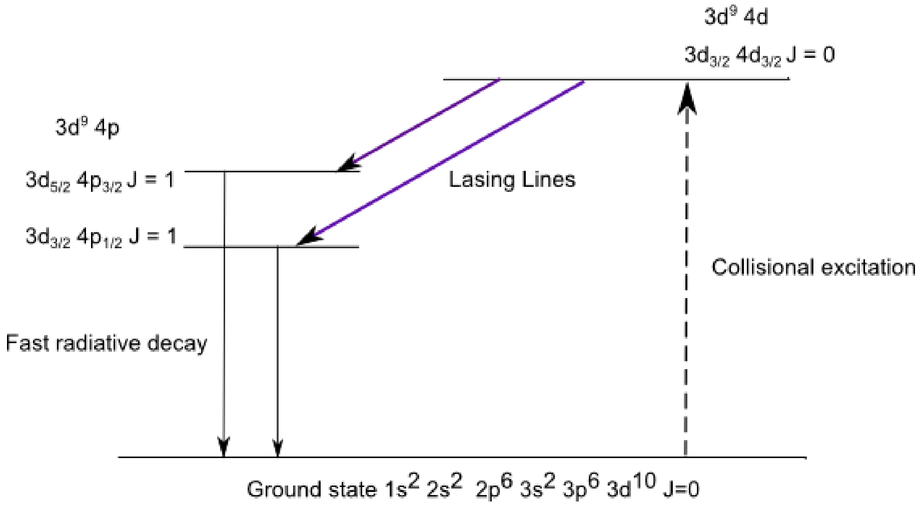

Figure 3.1: Term diagram for a Ni-like laser, adapted from [87].

state. From the 4d state decay to 4p$_{\frac{3}{2}}$ or 4p$_{\frac{1}{2}}$ can occur followed by fast radiative decay to the ground state, this process is shown in Fig. 3.1.

An alternative method of producing EUV lasing is to use a pulsed electrical discharge to create a highly ionised plasma column. Rocca et al. (1994) [89] discusses lasing observed in Ne - like argon at 46.9nm. Argon gas was preionised to improve plasma uniformity with a several ms, 10A pulse followed by a pulsed capillary discharge with a rise time of 20ns, a peak current of 40kA and a half cycle duration of 60ns. This produced a line plasma with typical dimensions 12cm × 200μm [89–91]. This method of producing EUV lasing can allow more compact EUV lasing systems.

When stimulated emission becomes a significant depletion process of the upper quantum state the laser gain medium is saturated. Saturation indicates the laser power is at a maximum and will reduce shot to shot variation in intensity during operation of the EUV laser. Output of the lasing medium is considered saturated when the product of the laser gain coefficient and lasing medium length is greater than approximately 15 [92].

3.1.2 X-ray Free Electron Lasers

X-ray free electron lasers (XFELs), typically have greater intensities, shorter wavelengths and shorter pulse durations with consequently greater bandwidth, than plasma based x-ray lasers. A large electron accelerator as used for particle physics studies is needed. The gain medium is an oscillating beam of electrons in an alternating magnetic field. Electrons are accelerated to relativistic energies to form the electron beam and then pass through an array of alternating dipole magnetic fields, known as an undulator, that causes the beam to oscillate sinusoidally. As these electron accelerate they emit synchrotron radiation at a fundamental frequency proportional to $\frac{\lambda_u}{\gamma^2}$, where λ_u is the undulator period and γ is the relativistic electron Lorentz factor. The radiation is coherent as electrons oscillate in phase with the electric field, adding emission in phase with the main beam. The electrons within the accelerated beam initially have a random phase distribution and will emit incoherent radiation at the resonant frequency. As the electrons travel through the undulator the electrons collectively interact with the emitted radiation and small coherent fluctuations in the radiation field begin to bunch electrons together at the resonant wavelength. These fluctuations grow until electrons are strongly bunched together [93].

Examples of these lasers include the linac coherent light source (LCLS) at the Stanford Linear Accelerator Center (SLAC), which has pulse lengths down to a few femto-seconds, with intensities of up to 10^{18}Wcm^{-2} and wavelengths down to 1.5 - 0.15nm [93, 94]. The Free-electron -Laser in Hamburg (FLASH) at Deutsches Elektronen-Synchrotron (DESY), has pulse lengths of greater than 10fs, with intensities of up to 10^{16}Wcm^{-2}, wavelengths of between 4.5 - 47nm and beam spectral widths typically of $\frac{\nu}{\Delta\nu} = 100$ [93, 95]. The FEL-1 beamline at FERMI@Elettra, Trieste, Italy currently operates at wavelengths of 20 - 65nm, with pulse lengths of 150fs [96] and SACLA (Spring-8 Angstrom Compact free electron LAser) at Spring-8, Japan is able to operate at wavelengths < 0.1nm [93, 97, 98] . The European XFEL, at DESY, is currently under construction,

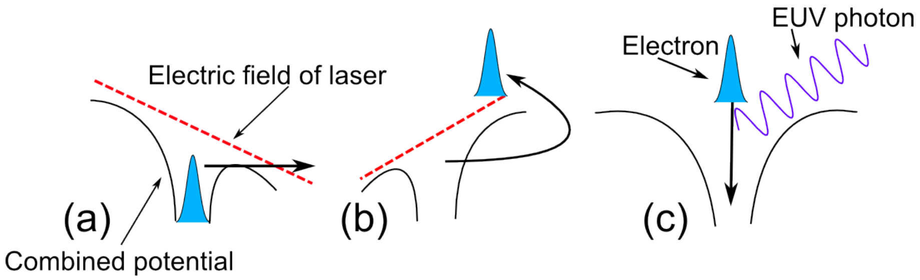

Figure 3.2: 3 Step process of high harmonic generation.
(a) electric field of laser suppresses atomic potential allowing electron to tunnel free from atom and accelerate away.
(b) electron is accelerated back as field reverses.
(c) electron recombines with atom emitting an EUV photon.

with expected wavelength range of 6 - 0.05nm and pulse lengths of <100fs [99].

3.1.3 High Harmonic Generation

The interaction of a high power laser with a solid target or a gas can be used to create a spectral sequence of harmonics of the original laser wavelength. In the case of a gas target, which is used in chapter 4, typically a 800nm laser with a pulse length of 20-100fs is focused to intensities of 10^{14}-10^{15}Wcm^{-2} within a jet of neutral He, Ne, Ar or Xe gas. It is desirable that the gas molecules remain unionised during the harmonic production, so inert gases with high ionisation energies are often used for harmonic production.

Harmonics are created by the linearly polarised electric field of the laser suppressing the binding potential of the atom allowing electrons to tunnel free. During the first half of the laser electric field cycle, these electrons are accelerated away from the atom. When the field reverses the electrons are accelerated back to the atom and either scatter or recombine (see Fig. 3.2). The rapid acceleration of the electron when this occurs causes it to emit energy in the form of higher energy photons at harmonics of the original laser energy with a limit of photon energy related to the pulse intensity. Due to the cyclic nature of the process, even harmonics are cancelled out and only odd harmonics are produced [1]. The maximum energy emitted is given by:

$$\hbar\omega_{max} = I_p + 3.2U_p \tag{3.1}$$

where I_p is the ionisation potential and U_p is the pondermotive potential, the kinetic energy of an electron averaged over one cycle. In an electric field E_0 with a frequency ω_0 the pondermotive potential is given by:

$$U_p = \frac{e^2 E_0}{4 m_e \omega_0} \quad . \tag{3.2}$$

Intensities of 10^{14}-10^{15}Wcm^{-2} are used for harmonic production as at greater intensities the magnetic field component of the laser field starts to have a significant effect on the motion of the electron, causing it to deviate and not return to the parent ion.

Fig 3.3 shows a typical harmonic spectrum, obtained in argon, with a 800nm, 10^{14}Wcm^{-2}, 35fs laser pulse. These harmonics are used to measure the complex refractive indices of iron and aluminium between 17eV and 39eV, discussed in chapter 4. This harmonic spectrum was measured using a channel electron multiplier after an EUV grating monochromator. The EUV grating monochromator allowed the selection of individual harmonics with high efficiency and low temporal broadening. The monochromator consists of a toroidal mirror to collimate radiation from the high harmonic source, followed by a diffraction grating and a second toroidal mirror which focuses radiation on to the exit slits. The incident and diffracted radiation wavevector is in a plane almost parallel to the grooves on the diffraction grating. By rotating the grating on an axis through the grating centre parallel to the grooves different wavelengths can be selected as the azimuth angle changes [101]. The angle of the elevation of the radiation above the grating is kept

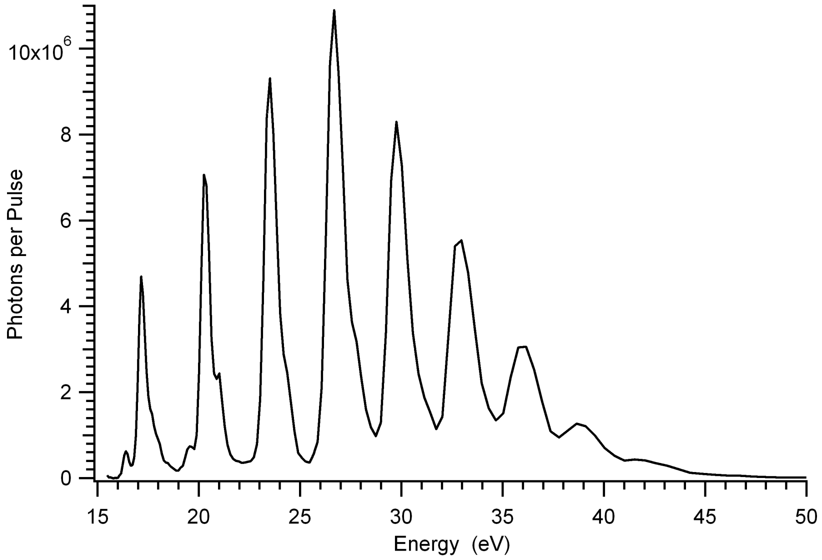

Figure 3.3: High harmonic spectrum produced on the Artemis facility at RAL [100], obtained in an argon gas jet, with a 800nm, 10^{14}Wcm^{-2}, 35fs laser pulse. Harmonics shown are 11 (17eV) to 27 (42eV)

constant. The grating equation is given by:

$$\sin\gamma(\sin\alpha + \sin\beta) = \rho_g\lambda \tag{3.3}$$

where γ is the angle of the incoming and outgoing radiation above the surface of the grating and α and β are the azimuth angle of the incoming and outgoing radiation respectively. The angle α is 0 if the rays are in a plane perpendicular to the surface of the grating and parallel to the grooves (see Fig. 3.4). In equation 3.3, ρ_g is the grating density. For the EUV grating monochromator $\alpha = \beta$ and the equation becomes [101]:

$$2\sin\gamma\sin\alpha = \rho_g\lambda \quad . \tag{3.4}$$

The monochromator will have a maximum efficiency when α is equal to the blaze angle of the grating. This leads to the form of the spectrum in Fig. 3.3, with the peak efficiency of the grating used to measure the spectrum occurring at 27eV. Efficiency drops off greatly towards 40eV.

Harmonics produced by the interaction of ultra-intense laser pulses with a solid target are

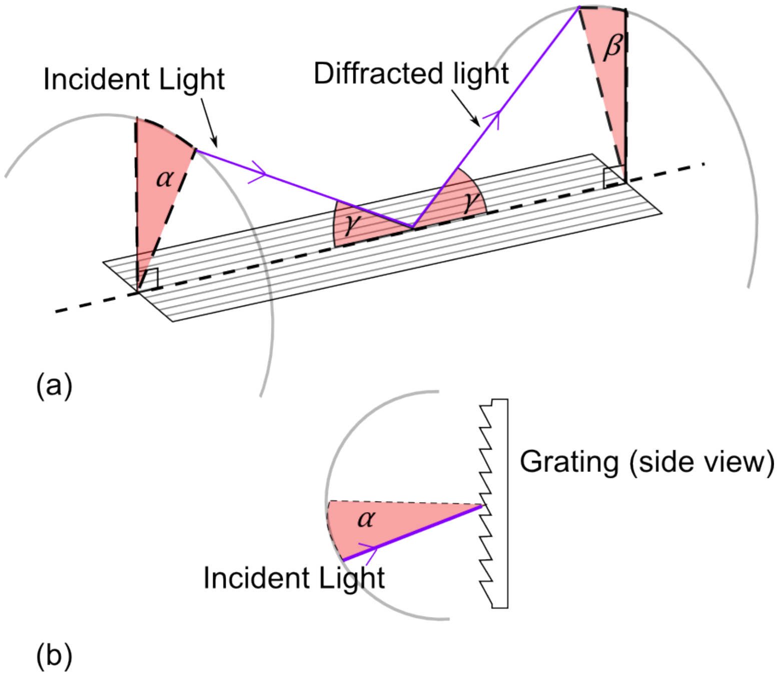

Figure 3.4: (a) Diagram of the EUV grating monochromator, γ is the angle of the incoming and outgoing radiation above the surface of the grating and α and β are the azimuth angle of the incoming and outgoing radiation respectively. (b) Side on view of grating with incident radiation with an azimuth angle α. Adapted from [101]

described by Dromey et al (2009) [102]. The interaction of the laser electric field with the target causes the electrons on the surface of the target to oscillate in phase with the laser. As the density in the plasma is greater than the critical density, this creates a relativistic oscillating plasma mirror allowing the Doppler frequency upshift of radiation reflected from the oscillating mirror, which produces a series of short pulse harmonics [102, 103].

3.2 EUV Optics

3.2.1 Multilayer Mirrors

At EUV photon energies materials tend to be highly absorbing as the photon energies readily match energy differences between quantum states in most materials. High absorption and poor reflectivity creates difficulties when reflecting and focusing EUV radiation. However, multilayer optics can allow high normal incidence reflectivity. Multilayer mirrors consist of alternating layers of materials with differing refractive index, usually a high and low Z material to increase the change in electron density. Commonly used examples include silicon and molybdenum and beryllium and molybdenum. The radiation reflected due to the change in refractive index results in constructive interference of the reflected light, with efficiencies of $> 70\%$ possible with Mo/Be coatings at 110eV [104]. Multilayer mirror reflectivity follows Braggs law, $m\lambda = 2d\sin(\theta)$, which gives the angle of maximum interference. At normal incidence, bi-layer separations of $\frac{\lambda}{2}$ are required.

Multilayer coatings can be applied to curved surfaces to make focusing optics. Multilayer optics have a variety of applications outside of plasma diagnostics, such as in astronomy and in EUV lithography which has driven a lot of mirror research [104]. The limit for multilayer coatings to provide high reflectivity at normal incidence occurs in the soft x-ray region (10s of Å) where the required value of coating thickness drops to a few atomic layers and the necessary relative uniformity of layers becomes difficult to achieve.

3.2.2 Grazing Incidence Mirrors

Even though at normal incidence EUV and x-ray wavelengths material reflectivity is low (see Fig. 3.5), at grazing incidence total external reflection can occur. Refractive indices n, in the EUV region are given by $n = 1 - \delta + i\beta$, where δ is the real part of the refractive index related to the phase of electromagnetic radiation within a material, and β is related to the absorption. The relationship between the angles of incidence θ_i and angle of refraction θ_r at a surface is given by Snell's law, so that ignoring absorption ($\beta = 0$) :

$$\sin(\theta_r) = \frac{\sin(\theta_i)}{1 - \delta} \quad . \tag{3.5}$$

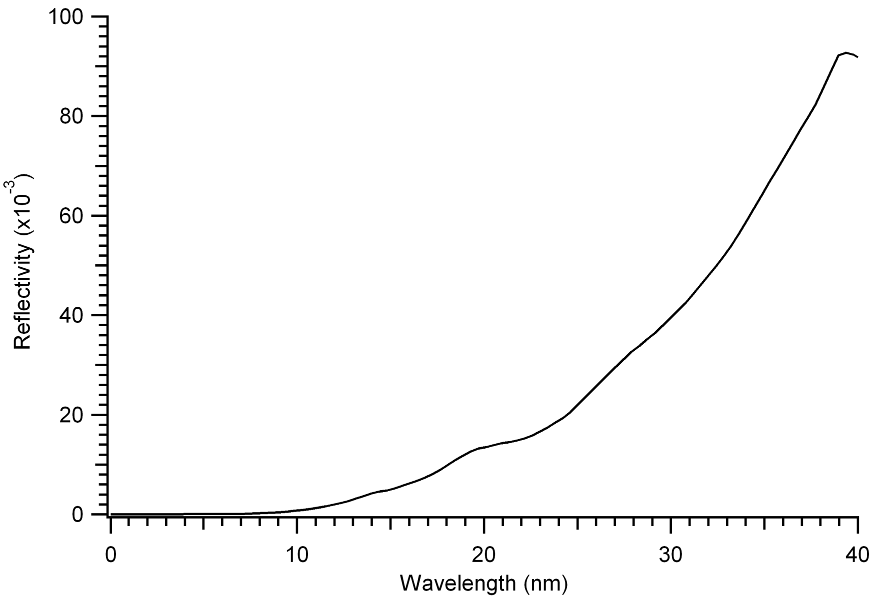

Figure 3.5: Reflectivity of gold at normal incidence as a function of wavelength in the EUV region [79]

The condition for total external reflection is that $\sin(\theta_r) = 1$, implying that $\sin(\theta_c) = 1 - \delta$. Converting from θ_r to ϕ_c, the angle between the reflected ray and the surface plane using $\phi_c = 90^\circ - \theta_r$ and applying the small angle approximation we obtain:

$$\phi_c = \sqrt{2\delta} \quad . \tag{3.6}$$

Higher Z material and a longer wavelength will increase the angle, (see chapter 2, 2.36), and typically coatings of materials such as gold with large δ are used. However, the absorption part of the refractive index β is neglected here, which for high Z materials may be significant and will effect the form of reflection curve as absorption increases smoothing out the expected strong angular dependence at the critical angle (see Fig.3.6) [1].

An experimental application of grazing incidence reflection is to filter unwanted shorter wavelength emission. This is often used in combination with a transmission filter to remove unwanted radiation. The method is used in chapter 5 to remove unwanted radiation around the 13.9nm EUV laser wavelength. A gold coated grazing-incidence mirror with a grazing angle of 7°, and a 0.15 μm thick zirconium filter before the CCD detector were employed to remove respectively short wavelength ($<$ 8 nm) and long wavelength ($>$ 17 nm) emission. The reflectivity of a gold mirror at 7° is shown in Fig. 3.7.

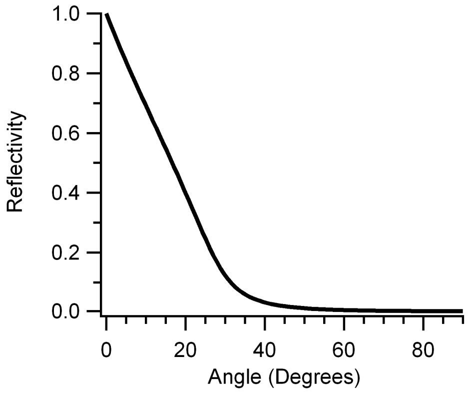

Figure 3.6: Reflectivity of gold at a wavelength of 13.9nm as a function of grazing angle of incidence [79].

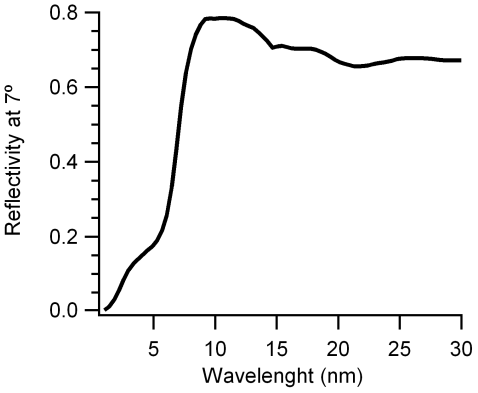

Figure 3.7: Reflectivity of gold at 7° incidence as a function of wavelength [79].

3.3 Shack Hartmann Wavefront Sensor

A Shack-Hartmann wavefront sensor (HWS) is used to measure wavefronts of electromagnetic waves. The radiation wavefront passes through an array of holes, sampling the wavefront as a series of beamlets which are then projected onto a CCD camera (Fig. 3.8). The position of each beamlet on the CCD can then be compared to reference positions from a shot with no target, allowing the slope of the wavefront at each point to be found and the wavefront reconstructed. Measurements of $\frac{\lambda}{\Delta\lambda} = 120$ are reported in [105] at wavelengths of 13.4nm. The advantage of the HWS over interferometric methods of phase front determination include the ability to work with partially incoherent beams, the ability to measure phase and intensity at the same time, a compact size and easy set up.

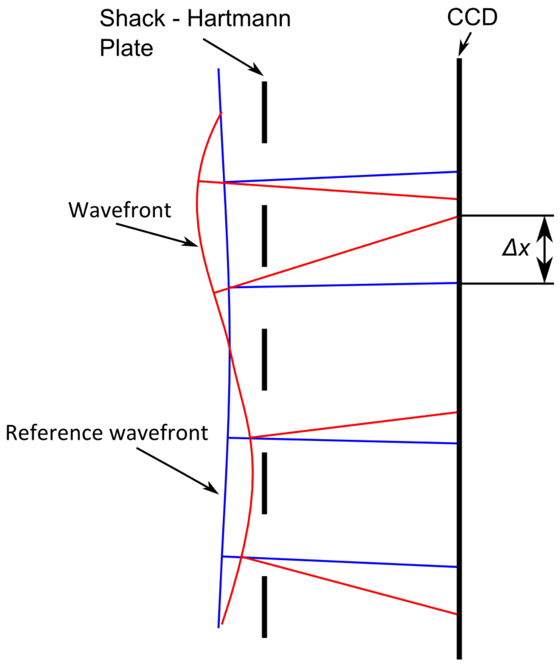

Figure 3.8: Diagram of a Shack-Hartmann wavefront sensor, showing the difference of position on a CCD of the reference and measured wavefronts, Δx. Adapted from [106]

3.4 Diffraction and Double Slit Interferometry

3.4.1 Coherence Measurements

One common requirement for EUV sources is a high degrees of coherence. This is required to allow focusing of radiation to small spot sizes, for interference measurements and to reduce beam divergence. Work discussed in chapter 4 includes measurement of the complex coherence factor of a high harmonic EUV radiation source, which was a requirement for accurate measurements of optical properties from the visibility of interference fringes.

Coherence can be regarded as measure of the degree to which phase and amplitude of an electromagnetic wave can be predicted at one point in space and time from a measurement at another position. The complex coherence factor γ, of an electric field, E, can be expressed as [1]:

$$\gamma_{12} = \frac{\langle E_1(t+\tau)E_2(t)\rangle_T}{\sqrt{|E_1|^2|E_2|^2}} \tag{3.7}$$

where E_1 and E_2 are the electric field at points 1 and 2. $|\gamma| = 1$ indicates a coherent field, $|\gamma| = 0$ is an incoherent field and $0 < |\gamma| < 1$ is partially coherent.

For the case of double slit interferometry, partial coherence will change the fringe visibility and so can be used to measure the coherence of an EUV source. The electric field of 2 interfering waves, E_1 and E_2 of the form $E = E_0 \cos(k \cdot r - \omega t + \phi)$, where k is the wavenumber and ϕ is the relative phase shift, is given by $E_{total} = E_1 + E_2$. Using $I = \left\langle \mathbb{R}E^2 \right\rangle_T$ and 3.7, we obtain [107]:

$$I = I_1 + I_2 + 2\sqrt{I_1 I_2}|\gamma| \cos \Phi \tag{3.8}$$

where $\Phi = k_1 \cdot r - k_2 \cdot r + \phi_1 - \phi_2$, the phase difference between the 2 waves. The visibility of interference fringes, V, is then given by:

$$V = \frac{I_{max} - I_{min}}{I_{max} + I_{min}} = \frac{2\sqrt{I_1 I_2}}{I_1 + I_2}|\gamma| \tag{3.9}$$

where I_{max} and I_{min} are the maximum and minimum fringe intensities. If $I_1 = I_2$, then the visibility of the source is equal to the magnitude of the complex coherence factor, $V = |\gamma|$.

3.4.2 Diffraction

Data analysis throughout this work requires understanding of far - field or Fraunhofer diffraction. It is used to measure the phase shift of solid materials using double slit interferometry (Chapter 4) and to analyse images of short pulse laser heated targets in the far - field limit (Chapter 6). The far field condition requires that the electric field incoming and outgoing from a diffracting aperture is approximately planar. This is summarised as:

$$R > \frac{a^2}{\lambda} \tag{3.10}$$

where R is the smaller of the distance to the aperture from the source, or the aperture to the image, a is the aperture size and λ is the wavelength. Using the Huygens - Fresnel principle, each point of the incident electric field $\overline{\boldsymbol{E}}$ can be described as a spherical wavelet with a source strength ϵ_A. The total field arriving at an image a distance R from the aperture is:

$$\overline{\boldsymbol{E}} = \frac{\epsilon_A \exp\left(i\left(\omega t - kR\right)\right) \exp(i\phi(y,z))}{R} \iint\limits_{Aperture} \exp\left(\frac{ik(yY + Zz)}{R}\right) dS \tag{3.11}$$

where y and z are positions on the aperture, Y and Z are positions on the image plane and ϕ is the relative phase shift.

Combining the variations in ϵ_A and constants to form an aperture function with amplitude $A_0(y,z)$ and a phase variation of $\phi(y,z)$, $A(y,z) = A_0(y,z)\exp(i\phi(y,z))$. Converting to spatial frequencies, $\frac{kY}{R} = K_y$, we get:

$$\overline{\boldsymbol{E}} = \iint\limits_{-\infty}^{+\infty} A_0(y,z) \exp\left(i\phi(y,z)\right) \exp\left(i(K_y y + K_z z)\right) dydz \tag{3.12}$$

This is the Fourier transform of the field distribution over the aperture function, which can be expressed as:

$$\overline{\boldsymbol{E}}(K_y, K_z) = \mathcal{F}\{\mathcal{A}(y,z)\} \tag{3.13}$$

This Fourier transform method is used to predict the image in the far - field of electromagnetic radiation on the rear side of a short pulse laser heated aluminium foil in chapter 6.

A double slit interferometer technique is used to determine the complex refractive index of solid materials using high harmonics. This technique uses 2 slits, with one half of one slit covered by the material of interest. The material over the slit results in a change in transmission and phase corresponding to a change in visibility and fringe position in the diffraction pattern. The diffraction

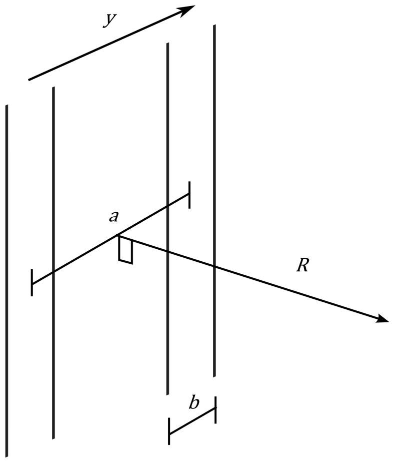

Figure 3.9: Diagram of double slits with slit separation a, slit width b, and distance to detector R.

from a double slit with one slit covered (see Fig. 3.9), results in a phase shift ϕ, with amplitudes given by ϵ_1 and ϵ_2 and can be calculated as follows, using 3.11:

$$\overline{\boldsymbol{E}} = \frac{\epsilon_1 \exp(i(\omega t - kR))}{R} \int_{-\frac{b}{2}}^{+\frac{b}{2}} \exp\left(\frac{ik_y yY}{R}\right) \, dy + \frac{\epsilon_2 \exp(i(\omega t - kR))}{R} \exp(i\phi) \int_{a-\frac{b}{2}}^{a+\frac{b}{2}} \exp\left(\frac{ik_y yY}{R}\right) \, dy \quad (3.14)$$

where a is the slit separation, b is the slit width, and R is the distance to the target.

Integrating, and substituting in $\frac{\exp^{i\theta} - \exp^{-i\theta}}{2i\theta} = \operatorname{sinc}(\theta)$ gives:

$$\overline{\boldsymbol{E}} = \frac{\epsilon_1 \exp(i(\omega t - kR))}{R} b \operatorname{sinc}\left(\frac{k_y bY}{2R}\right) + \frac{\epsilon_2 \exp(i(\omega t - kR))}{R} \exp(i\phi) \exp\left(\frac{ik_y aY}{R}\right) b \operatorname{sinc}\left(\frac{k_y bY}{2R}\right) \quad (3.15)$$

With $I = \left\langle \mathbb{R}E^2 \right\rangle_T$, we obtain:

$$I = \left[I_1 + I_2 + \sqrt{I_1 I_2} \cos\left(\frac{k_y aY}{R} + \phi\right) \right] \operatorname{sinc}^2\left(\frac{k_y bY}{2R}\right) \quad (3.16)$$

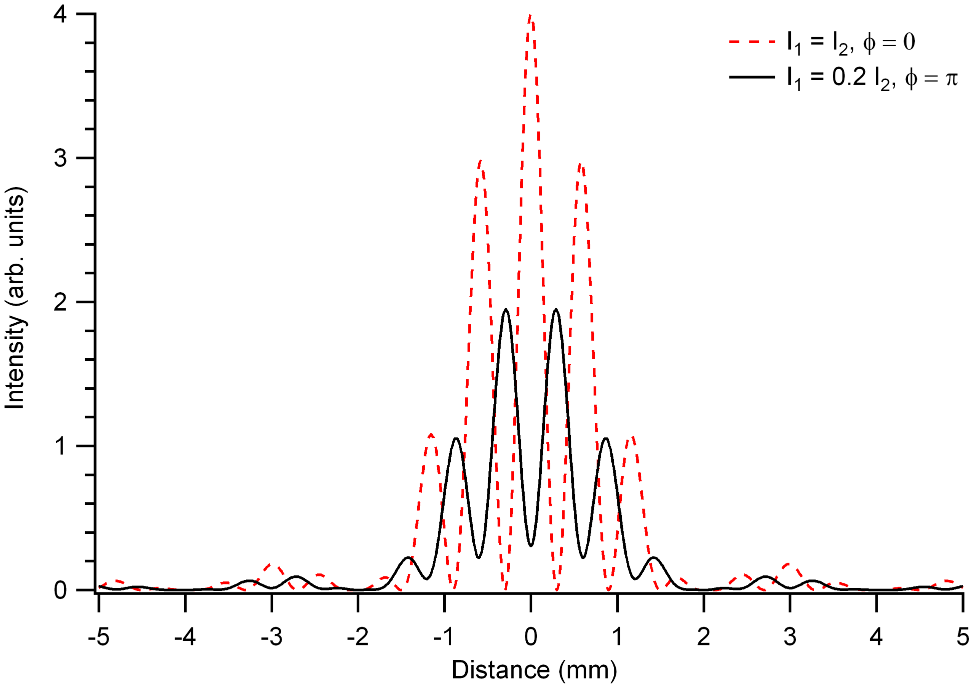

Figure 3.10: Far - field diffraction pattern for two slits of width 15μm and slit separation 50μm. The wavelength is 30nm and the distance to the detection screen is 1m. I_1 and I_1 are the intensities through slits 1 and 2 respectively and the phase difference between slits is ϕ (as indicated). For the case where one slit is assumed covered (Black solid line) the assumed intensity through the second slit is $0.2I_1$ and the assumed phase shift is π

Fig. 3.10 shows a diffracted image through a double slit with and without a phase and intensity change through one slit.

Using 3.9, and $I_2 = TI_1$, where T is the transmission, we obtain:

$$V = \frac{2\sqrt{T}}{1+T}|\gamma| \tag{3.17}$$

The transmission is then related to the imaginary part, β, of the refractive index by:

$$T = \exp\left(-\frac{4\pi\beta d}{\lambda}\right) \tag{3.18}$$

where d is the material thickness. Similarly, the phase shift, ϕ is related to the real part of the refractive index, δ by:

$$\phi = \frac{2\pi\delta}{\lambda}d \tag{3.19}$$

Using this double slit interferometry method, it is therefore, possible to measure simultaneously both real and imaginary parts of the refractive index of a material.

3.5 HYADES

HYADES is a one-dimensional Lagrangian radiation hydrodynamics simulation code developed by J. Larsen and CASINC [30]. Lagrangian codes maintain constant mass within each cell, with cell mesh moving with the material, in contrast to an Eulerian code where the mesh is fixed. Mesh point accelerations are found from pressure gradients using the Navier - Stokes equation (based on the conservation of momentum) to find mesh point velocities and positions. Three different set up geometries are possible - planar, cylindrical and spherical. This thesis concerns only planar slab targets. The electrons and ions are treated separately in a fluid approximation coupled together by Coulomb collisions, each with their own temperature. The electrons and ions are assumed to be in thermodynamic equilibrium with their velocities described by Maxwell - Boltzmann statistics. The photons can be described by a single group model and are assumed to have a Planckian distribution, or by a multigroup model which allows small departures from Planckian. Laser absorption via inverse bremsstrahlung up to critical density and resonance absorption at critical is included, with ionisation modelled by Saha, Thomas - Fermi, LTE - average atom, non - LTE average atom or fully ionised approximations. Hot electron interactions are not included in HYADES. However, work in chapter 5 includes heating via hot electrons as a dump of energy throughout the target in proportion to cell mass. This thesis uses the LTE average atom model of ionisation. All energy transport is considered diffusive with a flux limited model (see chapter 2). The flux limited model is studied in detail in chapter 5. Equation of state and opacity data are taken from sesame tables [108].

HYADES output of electron density, mass density and electron temperature have been combined with several post processers. Chapter 5, uses HYADES mass densities and electron temperatures to determine transmission using IMP opacities via equation 2.24, and Chapter 6 uses output of electron density and electron temperatures in a post processor written by the author, to calculate real and imaginary parts of the refractive index of aluminium, using a Saha - Boltzmann population model discussed in chapter 2. These post processors are described in more detail in the relevant chapters.

3.6 Summary

In this chapter the sources of EUV radiation used in this thesis have been described, with the diagnostics used in the following chapters also discussed. A description of the HYADES simulation code used to simulate experimental work in chapters 5 and 6 has been given.

Chapter 4

Double slit interferometry to measure the EUV refractive indices of solids using high harmonics

4.1 Introduction

Accurate values of the optical properties of materials are required to make extreme ultraviolet (EUV) optics such as filters and multilayer mirrors (see chapter 3 subsection 3.2.1) which are required for lithography, EUV astronomy and plasma diagnostics [1]. The properties of aluminium as considered in this chapter are particularly important as it is frequently used as a filter material and is an ideal material for theoretical comparison [7]. The optical properties of iron, which is also studied, are important in astrophysics as iron is a significant component of many astrophysical bodies. Ionised iron contributes significantly to the opacity of the sun [17] (see Chapter 1 subsection 1.1.2).

The real and imaginary parts of the refractive index can be related by the Kramers - Kronig relationship allowing the real part of the refractive index to be determined indirectly from measurements of the absorption over a large range of the spectrum [81–83] (see chapter 2 subsection 2.3.7).

The interferometry method described in this chapter allows simultaneous direct measurements of both components of the refractive index. This has the advantage of removing the error in the real part of the refractive index due to the error in measuring the imaginary part that will arise from using Kramers - Kronig analysis. This source of error can be large near absorption edges. Both real and imaginary components of the refractive index of aluminium between 77.0 nm and 113.5 nm (11 eV – 16 eV) have been previously calculated indirectly from the Fresnel coefficients derived from measurements of reflectance as a function of angle of incidence [109, 110]. This reflectance method has also been used to determine the optical constants of uranium between 10 - 47nm using a laser produced high harmonic source [111]. Independent measurements of δ for aluminium and nickel from 60 eV - 80 eV, and silicon and ruthenium from 89 eV - 105 eV have also previously been undertaken using transmission interferometry methods which allow simultaneous measurements of δ and β, with the coherent EUV radiation provided by undulator beamlines [112, 113].

The advantage of a transmission interferometry method compared to reflectance measurements is a large reduction in the effect of surface roughness on measurements as the transmission is measured at a normal incidence through the target. This method also allows for the effects of oxide layers to be taken into account without requiring targets maintained within high vacuum. Previous measurements of the transmission of aluminium have been made between the plasma frequency at 15 eV and the L3 edge at 72.7 eV by Gullikson et al (1994) using EUV emission from a laser produced plasma [114] and at 63.3 eV and 53.7 eV using Ne-like Ge and Ni EUV lasers by Keenan et al (2002) [71]. This work showed a disagreement between the measured

Al transmission and data from the CXRO database and the experimental results of Gullikson et al. However, good agreement was found to data from Henke et al (1993) [83]. This indicates a need for further investigation of aluminium EUV optical properties. The effects of aluminium oxide layers in these measurements was taken into account by using several different thicknesses of aluminium foils, assuming the aluminium oxide layer is the same thickness on each foil. The aluminium absorption coefficient can be found from the gradient of a plot of thickness against the logarithm of transmission. A similar method is used in this work to determine both components of the refractive index and to remove the effect of aluminium oxide from our data.

There are uncertainties in EUV refractive indices, especially where values change rapidly near absorption edges and in materials, in particular aluminium, which have oxide layers [71, 114]. Examples of discrepancies between data sets for Al can be seen in Fig. 4.8, which compares measured photo absorption data with calculated data from Henke et al. [83], the CXRO database [79] and Shiles et al. [81].

4.2 High Harmonic Set-up

Odd harmonics between 17eV and 42eV were generated with an 800nm, 35fs pulse laser focused to an intensity of 10^{14}Wcm^{-2} in an argon gas jet on the Artemis Facility at the Rutherford Appleton laboratories [100]. A monochromator with a resolving power of $\frac{\lambda}{\Delta\lambda}$=100 allowed the selection of individual harmonics (see chapter 3 section 3.1.3 for more details). The divergence of the beam is estimated to be 1mrad with a repetition rate of 1 kHz and a 35fs pulse length [100]. The average flux of the 17th harmonic after the monochromator was measured to be 1.1×10^{10}photons/s using a channel electron multiplier.

The range of different harmonics allowed simultaneous measurements of the real and imaginary parts of the refractive index as a function of photon energy for harmonics from 11 to 25

(17 eV – 39 eV) using a double slit interferometry method. Pairs of slits of 15μm width and 50μm separation were used. One half of one of the slits was covered with a foil of the sample material (see Fig. 4.1.). This sample foil results in a fringe shift and a change in fringe visibility of the interference fringes relative to the interference pattern from the uncovered part of the slit which could then be used as a reference. Measurements were made for samples of Al and Fe with thickness covering the respective ranges 100nm – 800nm and 30nm – 60nm.

This double slit interferometry method, as described in chapter 3 subsection 3.4.2, can also be used to measure the spatial coherence of the Artemis harmonic beam from a measurement of the fringe visibility (V) as a function of slit separation [115]. For an uncovered pair of equally illuminated slits the fringe visibility is equal to the magnitude of the complex coherence factor $|\gamma|$ (see equation (4.1)).

All the slits were placed 10cm from the monochromator exit slit and the interference patterns were detected on a multi-channel plate (MCP) detector positioned 120cm from the slits the output of which was then imaged on to a CCD camera. In order to increase the signal to noise ratio of the measurements which is dependant on the square root of the number of shots, data was taken with 937ms exposure for a series of 50 images with every sample. The repetition rate of the beam was 1 kHz giving a total of 46850 shots for each target. The experimental set-up is shown in Fig. 4.1. These images were then digitally summed to give a final image of the interference pattern (see Fig. 4.2.). To measure the amplitude of the complex coherence factor (γ) of the harmonic beam, pairs of blank slits of 25μm separation 10μm width, 50μm separation 15μm width and 75μm separation 15μm width were used. The smaller 10μm slit width for the 25μm target was chosen to increase the number of visible bright fringes from ~ 3 to ~ 5 improving the accuracy of visibility measurements. The visibility was measured for harmonics 11 - 29 (see Fig. 4.3.). The measured amplitude of the complex coherence factor for the 50μm slit separation was then used

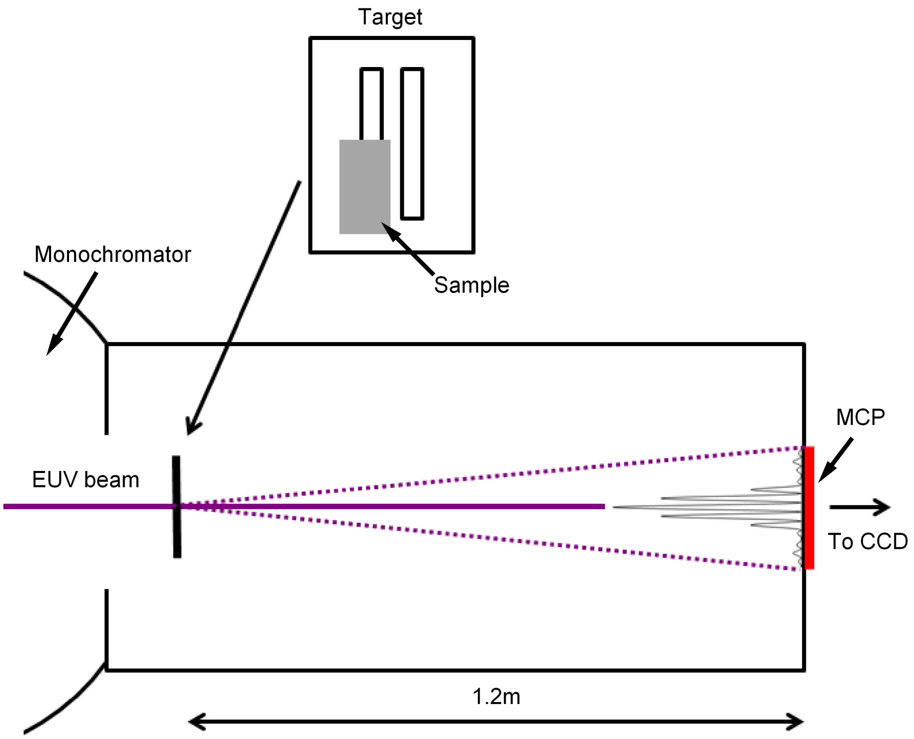

Figure 4.1: Diagram of experimental set up, with target design shown.

to determine the transmission (T) through half covered slits with a 50μm slit separation from a measurement of the fringe visibility (V) using:

$$V = \frac{2\sqrt{T}}{1+T}\,|\gamma| \quad . \tag{4.1}$$

The slits were positioned in the beam to maximise the peak intensity and visibility of fringes. The amplitude of the complex coherence factor as a function of slit separation for harmonics 11, 15, 21 and 25 are shown in Fig. 4.4. There is a high coherence of between 70% - 80% for the majority of harmonics up to the separation of 50μm used to measure the refractive indices. Coherence tended to decrease above harmonic 21 (see Fig. 4.3.).

The accuracy of the refractive index measurement is dependent on the equal illumination of the slits as unequal intensity will result in a decrease of fringe visibility and an underestimate of the coherence. However, an estimate of the effect of the maximum expected ratio of intensities of

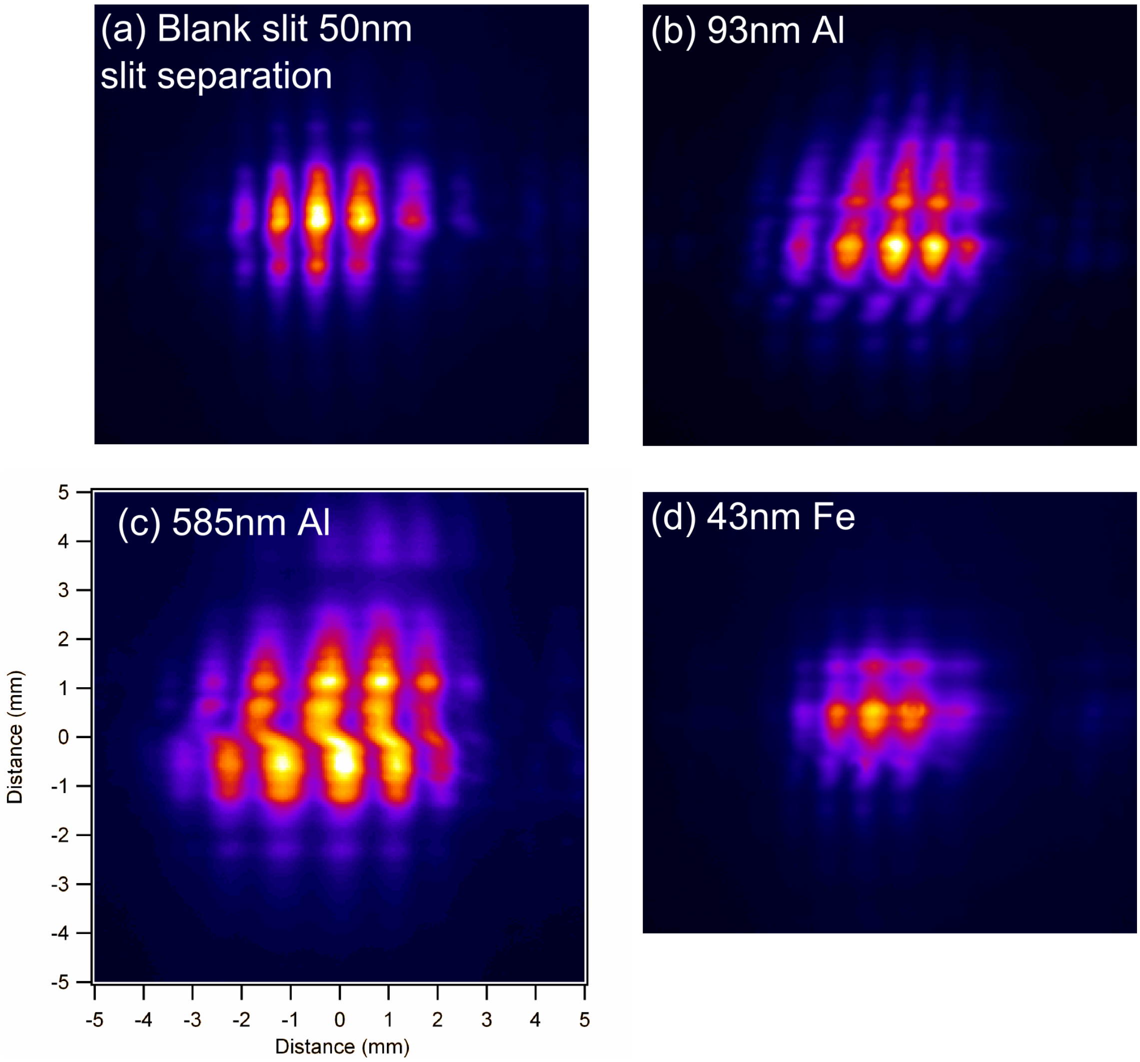

Figure 4.2: Examples of double slit diffraction as shown on the MCP at harmonic 21 (38eV). (a) is a blank target with slit separation 50μm and slit width 15μm, the rest are targets with one half of one slit covered with a sample material, (b) 93nm of Al, (c) 585m of Al and (d) 43nm of Fe. The top half of the images are the covered region. The phase shift and change in visibility due to the foils can be seen. The horizontal bar-like structure present in all images is due to diffraction from the edge of the foil and from bars used to keep the thin slits from bending, a tilt in the fringes due to a phase shift along the slit can be seen in the Al 100nm image. Image (c) includes the scale of the image on the CCD

0.70 – 1.30 through each slit, with a slit separation of 50μm and a beam width of >200μm using equation (4.1), only gives a decrease in visibility of 2%. Visiblity is most sensitive to changes in transmission at low values of transmission (see Fig. 4.5), so targets were chosen to have low values of transmission. The diffraction images (e.g Fig. 4.2.) show diffraction structure along the slits from the edge of the foil and from bars postitioned to keep the slits from bending. Visibility was measured over the most intense parts of the image, corresponding to the centre of the beam and the region with the highest coherence. In order to reduce errors in the measurement of the refractive index due to potentially unequal slit illumination and phase and to reduce the effect of surface oxide on the refractive index measurements, several different thicknesses of the sample foils were prepared in a single coating under vacuum. For aluminium, sample thicknesses were measured using optical and contact profiling to be 93 ± 1nm, 585 ± 3 nm, 610 ± 5nm and 800 ± 2 nm. The iron samples had thicknesses of 29 ± 1 nm, 43 ± 1 nm and 62 ± 2 nm. Optical profiling measures a surface profile by measuring the path distance between light reflected from the sample and a reference beam from their interference pattern. These foils were exposed to air before being inserted into the experimental vacuum chamber and so could have had oxide layers develop on their surfaces. Aluminium characteristically develops an oxide layer to a thickness of several nm, but iron transported under dry conditions may not form any appreciable oxide

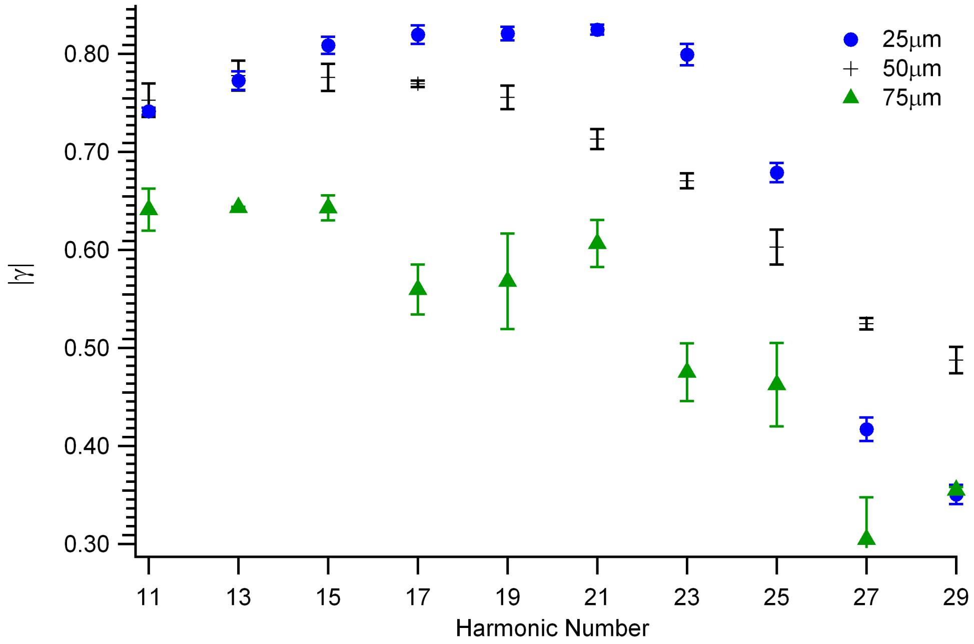

Figure 4.3: Amplitude of the complex coherence factor as a function of harmonic number for different slit separations (as labelled).

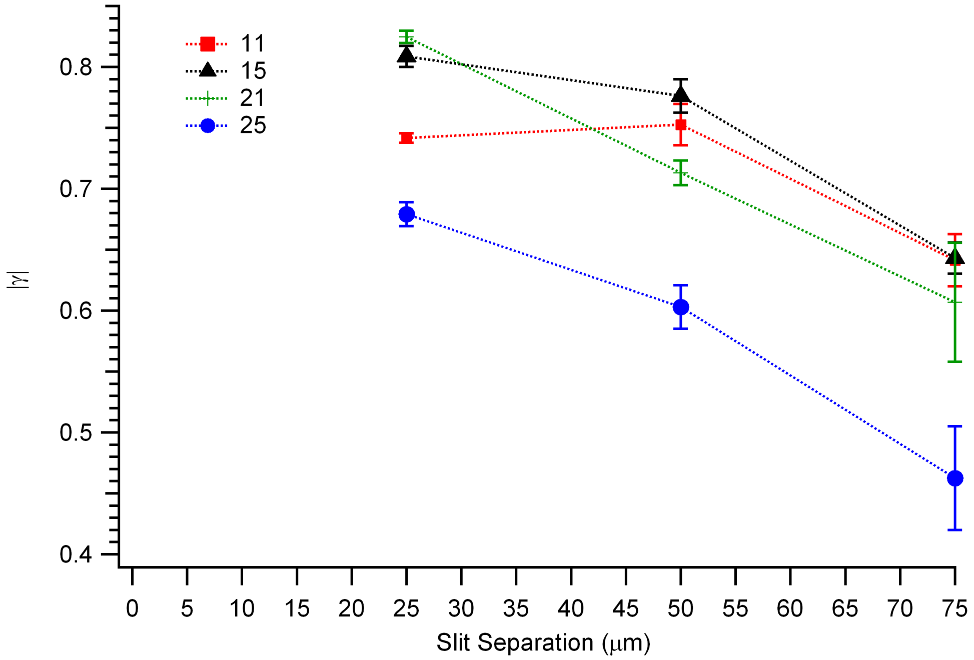

Figure 4.4: Amplitude of the complex coherence factor for different harmonics (as labelled) as a function of slit separation.

thickness. Assuming the oxide layer is the same thickness on each target material, the effect of these oxide layers on the aluminium refractive index measurements was removed by obtaining the imaginary part of the refractive index from the gradient of a plot of the logarithm of transmission against thickness and the real part from the measured phase shift against thickness. The point at which the y axis is crossed is dependant on the thickness of the oxide layer and the intensity and phase differences between slits.

4.3 Refractive Index Measurements

Phase shifts were measured from fringe shifts for each aluminium sample from harmonics 11 to 25. Data from the thickest foil (800nm) could only be used in measurements for harmonics 19 – 23 due to the very low fringe visibility in this photon energy range for this high thickness (see Fig. 4.6.). The real refractive index of iron could not be reliably extracted from the diffraction data so

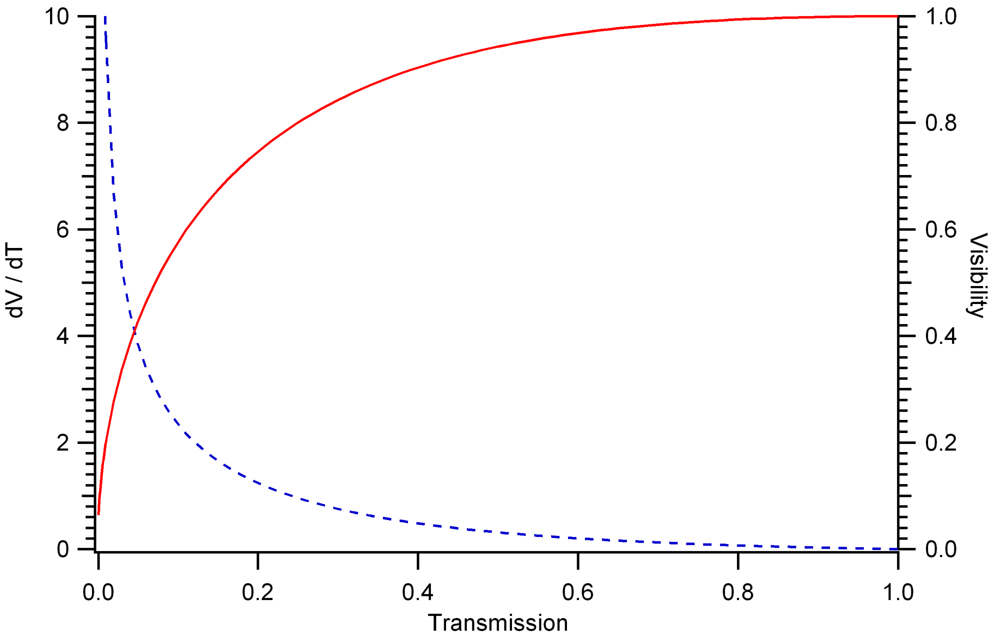

Figure 4.5: Visibility (red solid line) and rate of change in visibility (blue dashed line) as a function of transmission.

only the imaginary part of the iron refractive index is shown here. Fig. 4.7. shows the measured values (crosses) of the real refractive index component δ compared to experimental results from Larruquert et al. [109, 110] (circles), the CXRO database [79] (dashed line) and tabulated data taken from Smith et al. [82] and Shiles et al. [81] (line). Generally our measured δ values are lower than given in Shiles et al., showing increasing discrepancies at lower photon energies. This is also seen in the aluminium β values measured from the fringe visibility data (see Fig. 4.8.). In particular there is a discrepancy in the measured data not accounted for by the experimental errors with the tabulated data from Shiles et al. at 17eV. This may due to the proximity to the plasma frequency at 15eV leading to increased errors in the tabulated data which relies on the Kramers-Kronig transformation of absorption data. As discrepancies are also seen with Shiles et al. data in the imaginary part in this region, it is possible that this is a real feature. The errors shown for our measured δ values shown in Fig.4.7. are estimated from the deviation between repeated fringe shift measurements, for harmonics 11 to 21 and thicknesses of 93nm and 585nm, and the

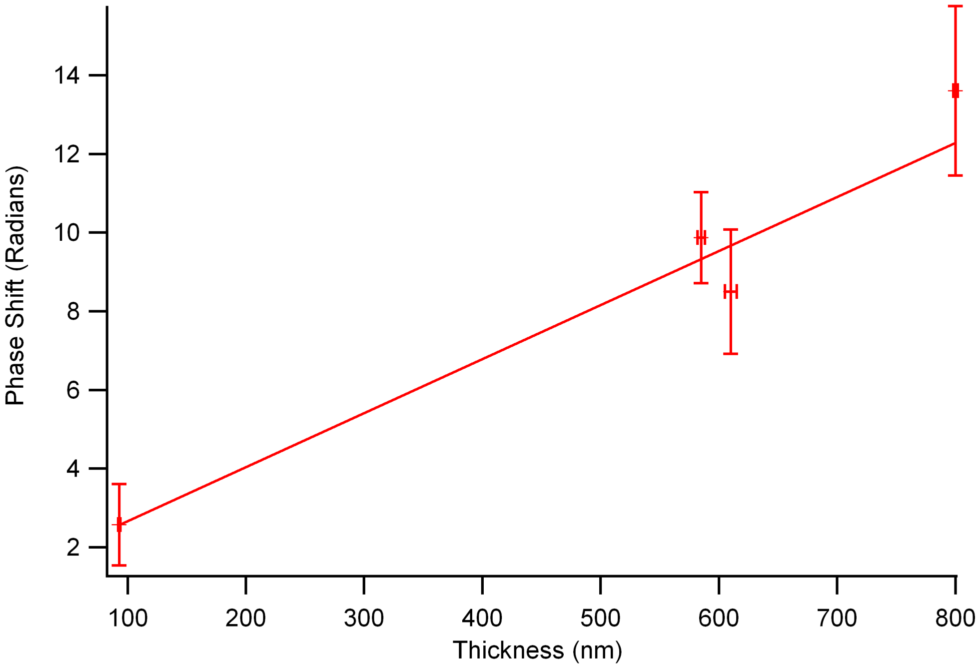

Figure 4.6: Measured phase shift as a function of foil thickness for Al foils at harmonic 23 (35eV).

estimated error in measurements of fringe position (see Fig. 4.6.).

For some images there is a noticeable tilt in the fringes along the slit direction (see Fig. 4.2) indicating a change in phase along the slit direction possibly due to uneven target thickness. This was taken into account in our measurements of the fringe shifts using a measurement of the tilt angle to determine any extra shift to the fringes. Fringe visibility measurements were made for harmonics 11 to 25, for the 3 thinnest aluminium foils and for all iron foils. Fig. 4.8. and Fig. 4.9. show the measured imaginary refractive index, β, for aluminium and iron. Comparisons to published data sets are also shown. For Al the β data generally shows good agreement with the CXRO data with values lower than expected from the Henke et al. [83] and Shiles et al. [81] data, particularly at lower energies. Agreement with the CXRO data is also seen in the measurements by Larruquert et al. There are small differences at 17 eV and 39 eV in our β values compared to the CXRO data. The iron β data shows higher values compared to both Henke et al. and CXRO data, again with the largest deviations appearing at 17eV and 39eV. The errors in our data points

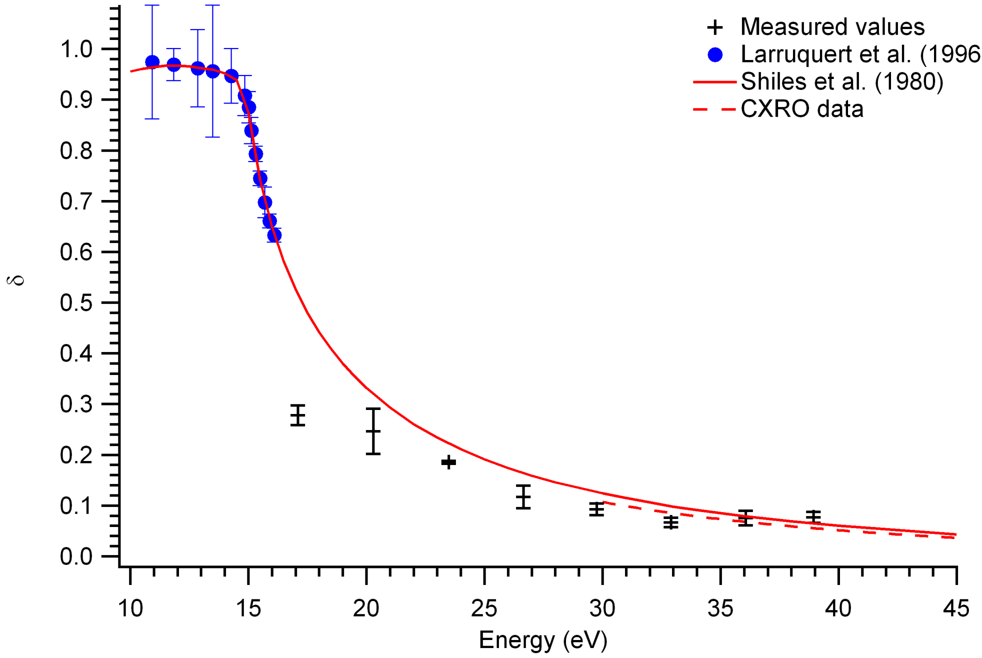

Figure 4.7: Measurements of the real component of the refractive index of Al compared to the CXRO database [79], Shiles et al. [81] and previous experimental work by Larruquert et al. [109, 110]

shown in Fig. 4.8. and Fig. 4.9. arise from both the spread of repeated results, and from estimated errors in the measurement of the fringe visibility.

4.4 Summary

Measurements of the real (δ) and imaginary (β) components of the refractive index of aluminium and the imaginary part of iron have been measured from 17eV - 39eV using harmonics from a short pulse laser. Aluminium beta values show good agreement with CXRO database [79] values as opposed to data from [83] and [81]. Discrepancies with Shiles et al data [81] at lower photon energies is also seen in the real part of the refractive index measurements. Iron β measurements show some deviation from the CXRO [79] and Henke et al. [83] data, generally showing higher values.

It may be feasible in the future to use lasers to create plasmas at times coincident with an EUV probe to measure the refractive index of plasma material. However, the EUV source would have to be brighter than the self emission of the target, and as the target will need to be replaced after each shot, images will have to be obtained within a single shot. This would make a XFEL or EUV laser a more likely EUV source due to their greater intensity than high harmonics for further study using this method with plasmas.

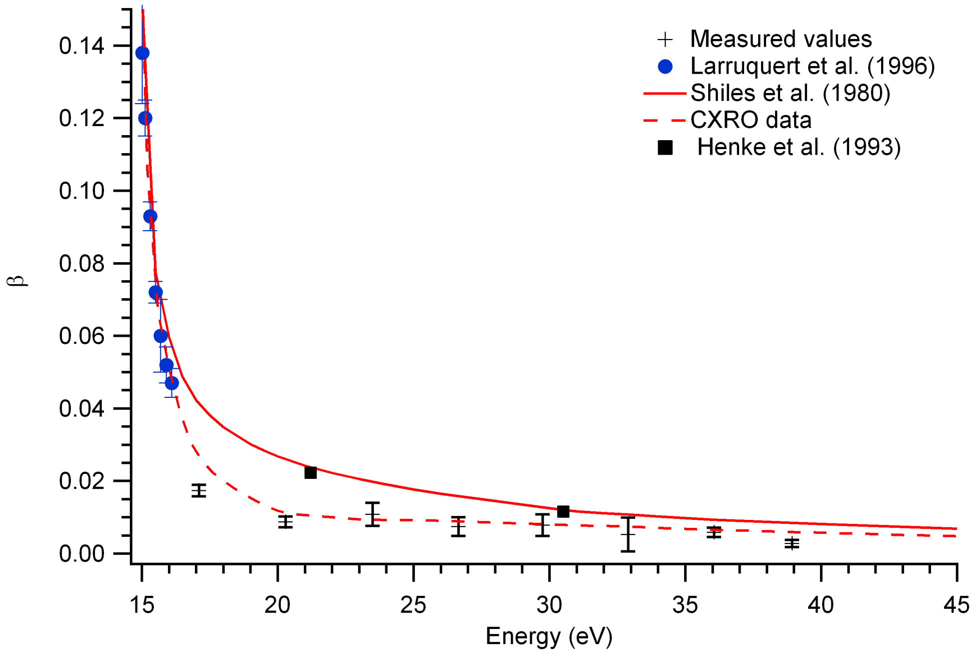

Figure 4.8: Measurements of the imaginary component of the refractive index of Al compared to the CXRO database [79], Henke et al. [83], Shiles et al [81] and previous experimental work by Larruquert et al. [109, 110]

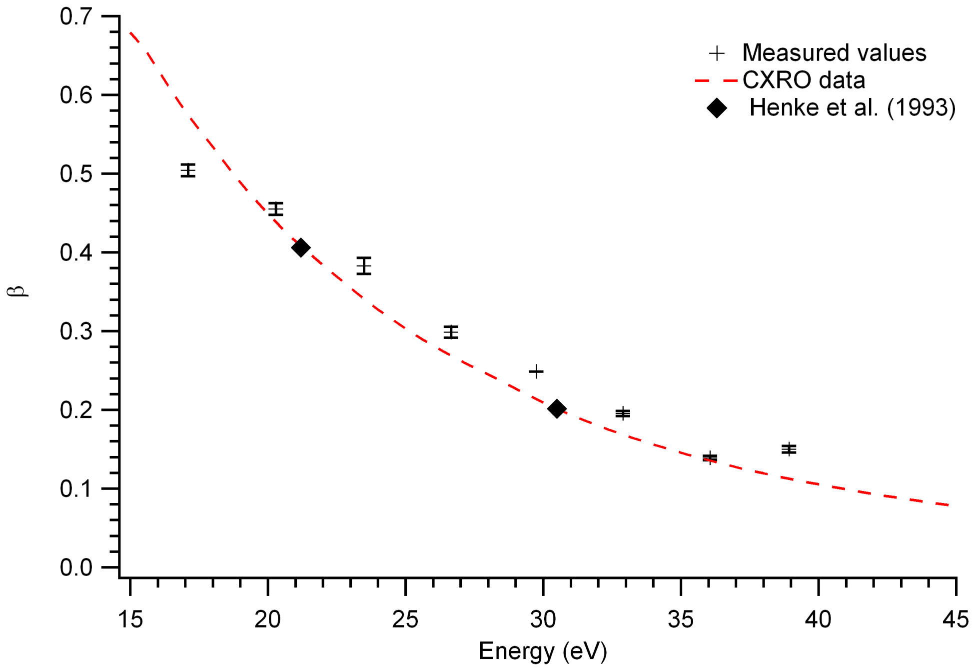

Figure 4.9: Measurements of the imaginary component of the refractive index of Fe compared to the CXRO database [79] and Henke et al. [83]

Chapter 5

Energy transport in short pulse laser heated targets measured using extreme ultra-violet laser backlighting.

5.1 Introduction

The efficiency of direct drive ICF is highly dependent on the energy flow from the region where the laser energy is deposited to the ablation surface [9]. In indirect drive ICF, understanding the heating of the cavity walls to produce x-rays is particularly important towards the end of the laser pulse when a final shock wave is driven to compress the fuel to ignition and a significant build-up of plasma expanding from the hohlraum wall means the laser energy can be absorbed away from the wall (see chapter 1 subsection 1.1.1).

As well as absorption by inverse bremsstrahlung and by collective processes such as resonance absorption [34], additional processes such as stimulated Raman scattering and stimulated Brillouin scattering can occur near the critical density [116] (see chapter 2 subsection 2.1.3). The collective processes may produce hot electrons which often penetrate into the solid target and heat it before thermal conduction occurs, which is particularly disadvantageous in ICF as the pre-heated fuel is more difficult to compress (see chapter 1 subsection 1.1.1).

Absorption is found to vary between $A \approx 40\%$ at long wavelengths increasing to $\approx 80\%$ at shorter wavelengths ($\lambda < 1\mu$m) at the irradiances and ns pulse lengths of interest for ICF (10^{14} - 10^{16} Wcm^{-2}) [117, 118]. At shorter fs - ps pulse lengths, absorption is typically $A \approx 30\%$. Resonance absorption can be strongly dependant on the angle of incidence of the heating pulse, particularly with short pulse irradiation on a steep density gradient [36, 37].

The thermal flow rate q of energy from the critical density surface to the ablation surface in laser-produced plasmas has been shown to deviate significantly from the classical heat flow rate. In fluid code modelling of the steep density and temperature gradient region between the critical and ablation surfaces, it was found that the thermal flow of energy needs to be adjusted using a flux limiter, typically with a value of $f \approx 0.03 - 0.01$ [41, 42] (see chapter 2 subsection 2.1.5). The correct value of the flux limiter is an issue in modelling x-ray production from the NIF hohlraum wall in indirect drive [43, 44] . The recent integrated experiments at the National Ignition Facility have made it clear that more extensive benchmarking of the electron transport models employed in the design of ICF targets is necessary, in order to have a satisfactory predictive capability. However, on more complex experiments, such as the implosion and hohlraum energetics experiments being performed at the NIF, it is difficult to resolve the effects of the many different uncertainties that are present. In this chapter an experimental methodology which enables the effects of electron conduction to be measured in a more direct fashion is presented.

Measurements of the EUV absorption of iron plasmas have previously been undertaken using high Z, quasi-continuum spectrally broad backlighters impinging on radiatively heated iron foils. Examples of these types of experiments have been reported by Da Silva et al., Winhart el al. and

Springer et al. [2, 63, 119] and are described in more detail in chapter 2 subsection 2.3.5. In this chapter measurements are described of the transmission of an extreme ultra-violet (EUV) laser backlighter of photon energy 89 eV through sample targets with an iron layer (50 nm thick) buried in plastic (50 nm overlay). The 50 nm thick iron layer is highly opaque to the EUV radiation at room temperature (transmission = 0.08), while the plastic overlay is relatively transparent (transmission = 0.85). As energy from the laser is conducted from the lower density absorption region to the high density solid material, the iron layer is heated and ionised. When ionization to Fe^{5+} (ionization energy 99.1 eV) occurs, bound-free absorption in the iron is no longer energetically possible, so the iron becomes highly transparent. We show that this switch in the transparency of the iron acts as a direct signature of the heat penetration into the target and enables a measure of the heat flow into the target. Potential for further work using this method with a double pulse set-up is also examined.

5.2 EUV Transmission Measurements

For this experiment, EUV radiation of pulse energy $\approx 1\ \mu$J at wavelength 13.9 nm (photon energy 89 eV) from Ni-like silver laser output was produced at the LASERIX facility [120] using grazing-incidence irradiation of a solid silver slab with 800 nm wavelength laser light comprising a deliberate 500 ps, 400 mJ pre-pulse and a 4 ps, 1 J main pulse. The EUV laser divergence was measured as 5 mrad $\times$ 10 mrad. The EUV laser output was focussed onto a sample tamped iron target using a 300 mm focal length spherical multilayer mirror positioned at 7° to the target normal. A diagram of the experimental set-up is shown in fig. 5.1. The EUV laser flux transmitted through the target was imaged with magnification of 4 using a 500mm focal length spherical multilayer mirror onto a CCD detector. A gold coated grazing-incidence mirror (grazing angle 7°) and 0.15 μm thick zirconium filter before the CCD detector were employed to remove respectively

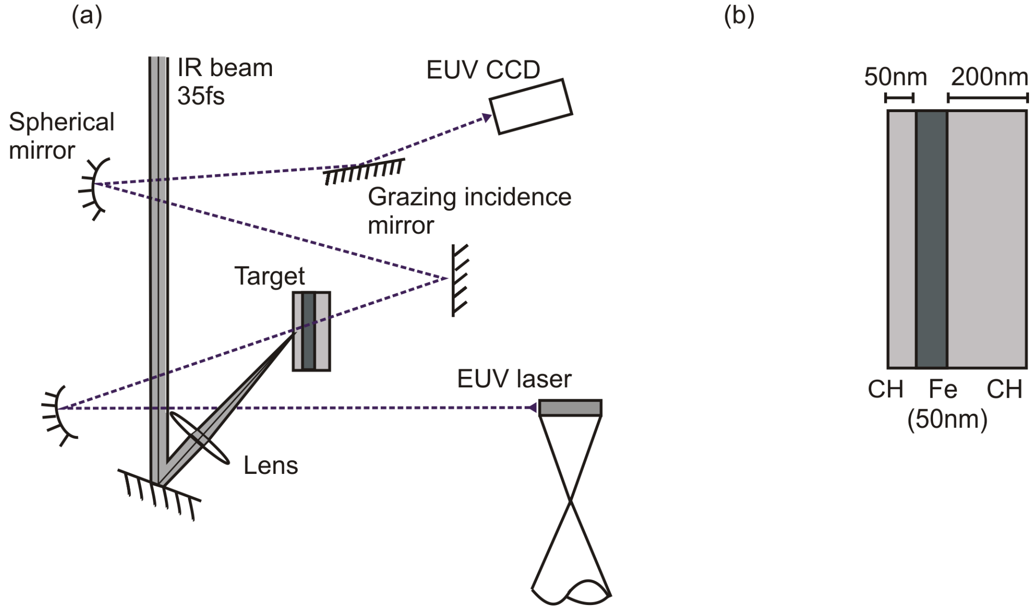

Figure 5.1: (a): Schematic showing the measurement of EUV laser transmission through a short pulse (35fs) laser heated iron layer (50nm) buried in plastic (CH). The EUV laser is focused onto the target and the target EUV transmission is imaged onto a CCD camera. (b): A schematic of the iron buried layer target.

short wavelength (< 8 nm) and long wavelength (> 17 nm) emission from the sample target. The duration of the EUV laser pulse determines the temporal resolution of the measurement and is estimated from experiments and modelling studies to be less than 5 ps [121]. The wavelength of the EUV laser has been accurately measured as 138.92 Å± 0.15 Å[122].

The sample targets used for the heat flow study were irradiated by an 800 nm, 35 mJ, p-polarized pulse of duration 35 fs incident at 20° to the target normal focussed by a 200 mm focal length lens. The sample targets consisted of a flat iron foil of 50 nm thickness tamped on the backside by 200 nm of parylene-N (CH) and on the front-side by 50 nm of parylene-N (see fig. 5.1). Pre-pulse irradiation commencing 40 ps before the main pulse initially at 10^{-7} contrast ramping to 10^{-4} contrast at 1 ps before the 35 fs pulse (see Fig. 5.2) was measured using a third-order autocorrelator.

A sample image of the EUV laser transmission through a tamped iron target at time 130 ps after the main pulse recorded on the CCD detector is shown in fig. 5.3. Using an EUV laser back-

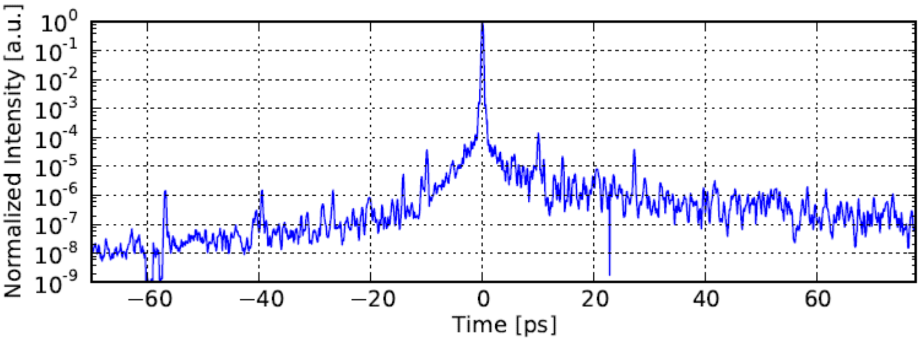

Figure 5.2: LASERIX heating pulse intensity as a function of time from peak of pulse measured using a 3rd order auto-correlator. Data obtained by Olivier Delmas at LASERIX

lighter source and heavy filtering away from the backlighter laser wavelength has ensured that the transmitted backlighter signal is much brighter than the plasma self-emission. The EUV laser beam transmission through the 800 nm laser irradiated area and the un-irradiated area is clearly apparent (fig. 5.3).

By recording images with and without an incident EUV laser and with and without an iron target heating pulse (see fig. 5.4 for EUV laser and heating pulse only shot examples), it was verified that there is only a spatially broad fluorescence arising from plasma self-emission and that the increase in recorded signal at the focal position (the bright region on fig. 5.3) is due to increased transmission of the EUV laser through the target. The transmission through the target has been measured from plots such as fig. 5.3 by comparing the spatially broad EUV laser intensity transmitted where no heating has occurred and the EUV intensity transmitted at the centre of the 35 fs laser focal spot. With our procedure, we found that the measured cold target EUV transmission is in agreement with tabulated values [79].

Varying the timing between the EUV laser creation pulses and the sample target heating beam enabled the transmission of the EUV laser at different times in the laser interaction with the tamped iron target to be measured (fig. 5.5). The errors in the transmission of the EUV laser are due to

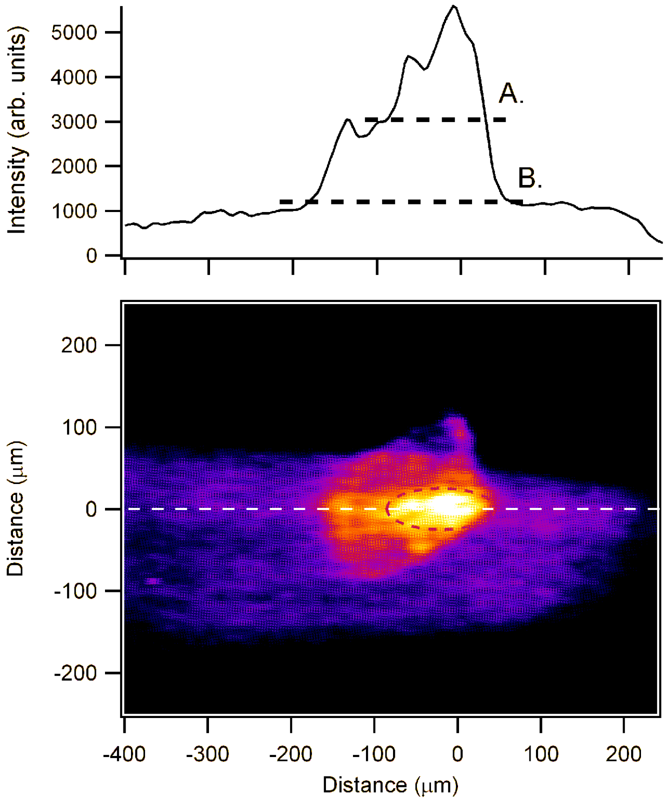

Figure 5.3: Image of the EUV laser radiation at 89 eV transmitted through a CH tamped 50 nm thick iron target at time 130 ps. The EUV radiation is transmitted through a largely unirradiated portion of the target (over 200 × 150 μm^2) with a smaller section of higher transmission where irradiation with a 35 fs laser pulse has heated the iron (encircled). On the line-out, A represents the level of EUV radiation transmitted through the unheated target, while B represents the base level of background signal found to be associated with self-emission from the tamped iron target. The large, over 600 × 200 μm^2 area of emission is due to scattered self emission.

the variation of the intensity of the EUV laser over the beam area and the spatial variation of the centre of the 35 fs focal spot irradiance. These errors are indicated by the error bars on fig. 5.5. The shot to shot variation between the data points is due to variations in irradiance of the heating beam.with each data point representing a single shot. Although the laser system can operate up to 10 Hz, it was necessary to re-position a replacement target for each shot. The fig. 5.3 images of the transmitted EUV laser flux enable a measure of the target area irradiated by the 35 fs optical pulse. From fig. 5.3 and similar images, the irradiated area is 100 μm × 50 μm implying peak irradiances of 3×10^{16} Wcm^{-2}. This measurement of the focal spot diameter is in agreement

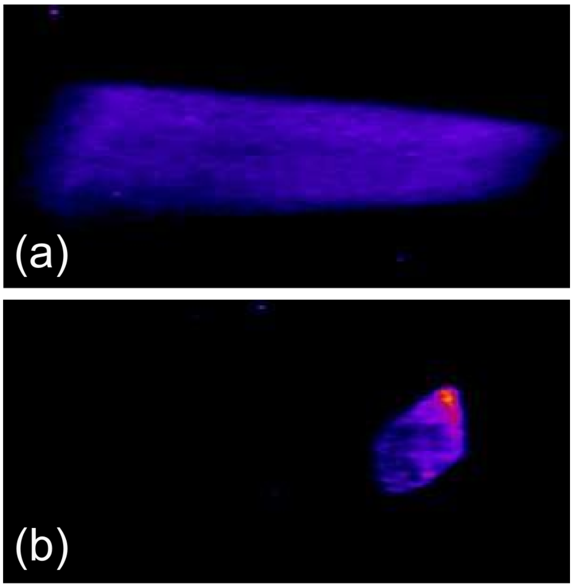

Figure 5.4: (a) EUV CCD image of the heated target with no EUV laser. This shows the extent of the target self emission. (b) EUV laser footprint on the CCD, no target or heating beam included.

with measurements made by imaging the attenuated laser beam. Some spatial frequency chirp is apparent in the focal spot causing the elliptical focal region (see fig. 5.3), but this does not affect the results presented here.

5.3 Simulations of EUV Transmission

The one-dimensional radiation hydrodynamics code HYADES [30] was used to simulate the irradiated tamped iron target temperatures, ionisation and density as a function of time and distance from which the EUV transmission was calculated. The code uses the Los Alamos Sesame library [108] for the equation of state of the plasma material. Laser energy deposition in the expanding plasma profile is modelled by calculating the rate of inverse bremsstrahlung and resonance absorption for p-polarised light incident at 20° to the target normal. The measured pre-pulse irradiation profile with an assumed Gaussian pulse shape of 35 fs full-width half maximum width at the time of the main pulse was used as a temporal profile for the laser irradiation. The effect on calculated

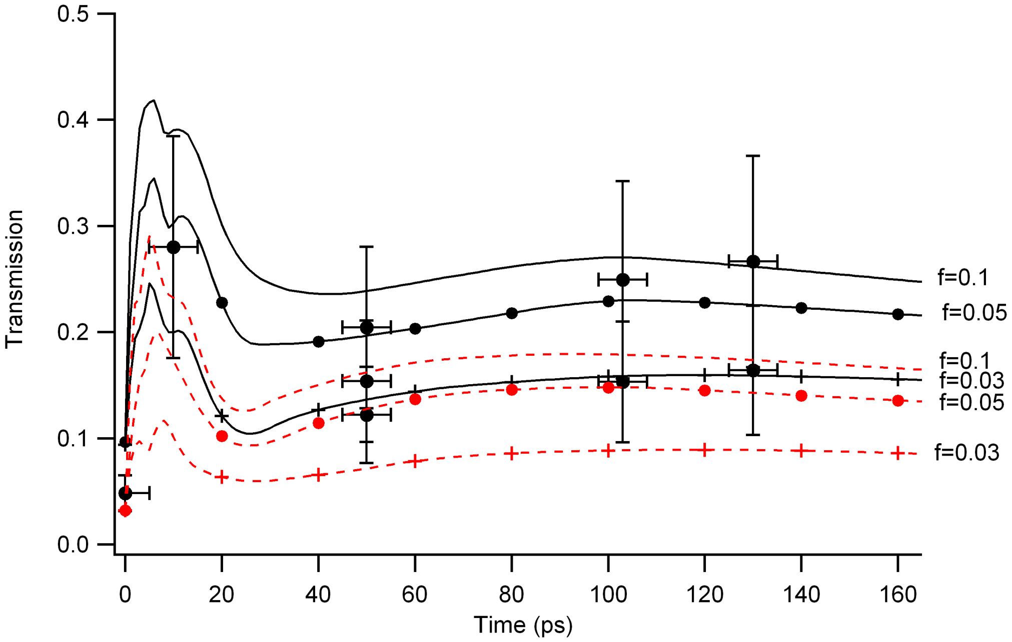

Figure 5.5: Transmission of EUV laser radiation at 89 eV as a function of time through a tamped 50 nm thick iron target. The target is irradiated at 0 ps by a 3 × 10^{16} Wcm^{-2} peak irradiance pulse of 35 fs duration. Simulation results using the HYADES code and a revised IMP opacity model post-processor are superimposed on the measured transmissions (shown with error bars). Simulation results are shown for various values of flux limiter (as labelled) calculated assuming (i) energy transport occurs via thermal conduction only (dotted curves) and (ii) hot electrons dump a fraction 10% of the laser pulse energy through the target at 0 ps and then energy transport occurs via thermal conduction (solid curves).

EUV transmission from the presence of the pre-pulse was found to be important, however, variations in the level of the prepulse of up to 50% have been found to have little effect (see fig. 5.6). The effective energy flow rate q between the critical and ablation surfaces was calculated using $\frac{1}{q} = \frac{1}{q_{SH}} + \frac{1}{f q_{fs}}$, where $q_{fs} = \nu_e n_e k T_e$, $q_{SH} = - \kappa \nabla T_e$ and f is the flux limiter.

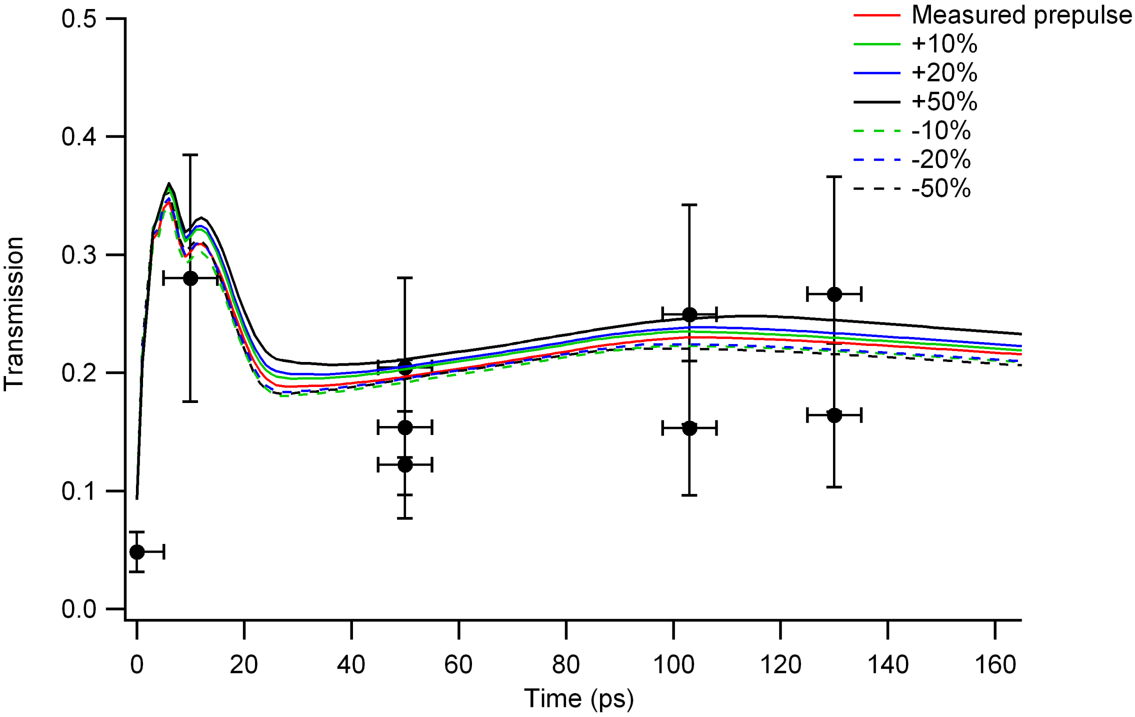

Figure 5.6: Transmission of EUV laser radiation at 89 eV as a function of time through a tamped 50 nm thick iron target. The target is irradiated at 0 ps by a 3 × 10^{16} Wcm^{-2} peak irradiance pulse of 35 fs duration. Simulation results using the HYADES code and a revised IMP opacity model post-processor are superimposed on the measured transmissions (shown with error bars). Simulation results are shown for various values levels of prepulse from the measured prepulse values (solid red line) to the measured prepulse plus or minus 10% (green lines), 20%(blue lines) and 50% (black lines)

A post-processor was used to calculate the transmission T through the target of the 13.9 nm EUV radiation (photon energy 89 eV) from the fluid code calculated electron temperature T_e, mass density ρ and cell dimensions. Tabulated opacity σ values from the IMP (ionized materials package) code [77, 78] which assumes LTE ionization balance were employed to give the transmission

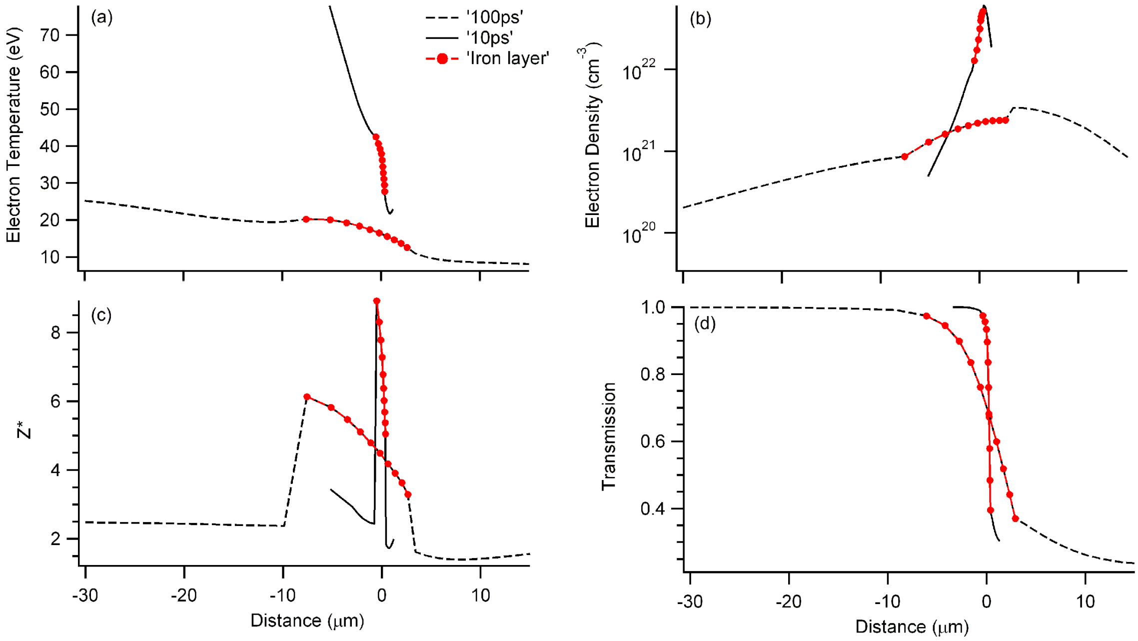

Figure 5.7: Cross sections of sample electron temperature T_e (a), electron density n_e (b), average ionisation Z^* (c) and target transmission T (d) as a function of distance from the target surface at 10ps (full line) and 100ps (broken line) after the irradiation of the target as illustrated in Fig. 5.1(b) with peak irradiance 3 × 10^{16} Wcm^{-2} in a 35fs pulse (with prepulse). The results are simulated using the HYADES code with a flux limiter of 0.05 and an assumed dump of 10% of the laser energy into hot electrons which are deposited proportionally to mass density in the target. The position of the iron component of the target is indicated by superimposed circles. The heating laser pulse is assumed incident from the left (negative distance positions). A pre-pulse starting 70ps before the 35fs pulse as measured in the experiment is assumed for the simulations.

T using:

$$T = \exp\left(-\int \rho\sigma dx\right)$$

where the integration is through the target at the 7° incidence angle to the target normal of the EUV laser beam. The opacities are dominated by the effect of photoionization (bound-free processes) in iron ions with ionization energy less than the photon energy. The opacities become small when ions of charge state Fe^{5+} with ionization energy 99.1 eV (or higher) predominate. Ions of lower ionization (eg. Fe^{4+} with ionization energy 75.0 eV) heavily absorb the 89 eV photons. The plastic opacity is also modelled in the post-processor code, but the plastic layers have only a small effect on the overall target transmission as the tamped overlay transmission is initially high at 0.85 and with heating only increases closer to 1 (see fig. 5.7). Fig. 5.7 shows the electron temperature, electron density, average ionization (Z^*) and transmission throughout the target at times 10ps and 100ps after the 35 fs heating pulse. Fig. 5.7 and fig. 5.8 show a decrease in spatial variation in the iron layer conditions with time. For example, the variation in electron temperature across the iron layer is 15eV at 10ps reducing to 8eV at 100ps and 6eV at 170ps. A similar trend of increasing uniformity with time is also seen in the electron density and average ionization. Peak values of temperature, ionization and density occur at time 1ps. The peak in EUV transmission of the iron occurs later at 6ps (see fig. 5.5) as the electron density begins to drop, but the ionization of the iron remains high.

The electron temperature and density through the target at 0ps immediately after the heating pulse is shown in fig. 5.9. This shows the front plastic layer of the target is heated to high temperatures by laser absorption up to the critical density and thermal conduction, while the iron layer indicated by the red line with circles, is at a higher temperature than the surrounding plastic, due to hot electron heating which rapidly heats the whole target after irradiation. The iron layer is heated to a higher temperature than the surrounding plastic due to its greater density. After the

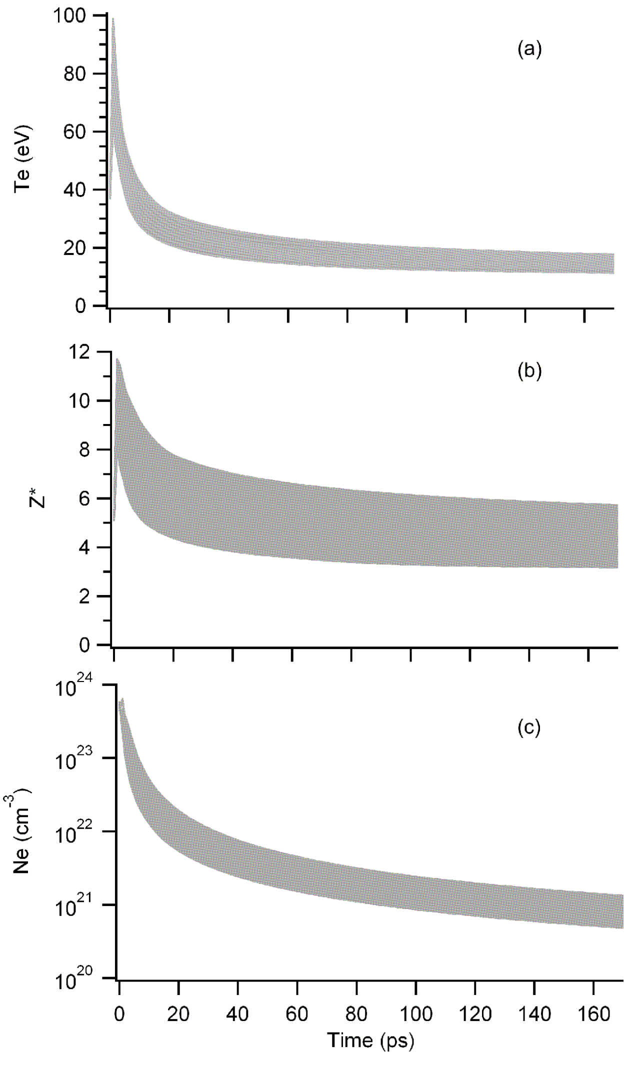

Figure 5.8: Sample target electron temperature T_e (a), average ionisation Z^* (b) and electron density n_e (c) within the iron layer as a function of time from the arrival time of the heating pulse simulated using the HYADES code at a peak intensity of 3 × 10^{16} Wcm^{-2} calculated with a flux limiter of 0.05 and 10% hot electron energy dump in the target. A pre-pulse starting at time - 70ps as measured in the experiment followed by the 35fs pulse at time '0ps' is assumed for the simulation.

initial heating by the short pulse beam, the value of the flux limiter may not change significantly as the target will begin to expand adiabatically leading to constant ionisation (see fig. 5.8) as LTE adiabatic expansions with $T_e^3(n_e + n_i)^{-2}$ = constant (see chapter 1 subsection 1.1.2) will have constant ionisation.

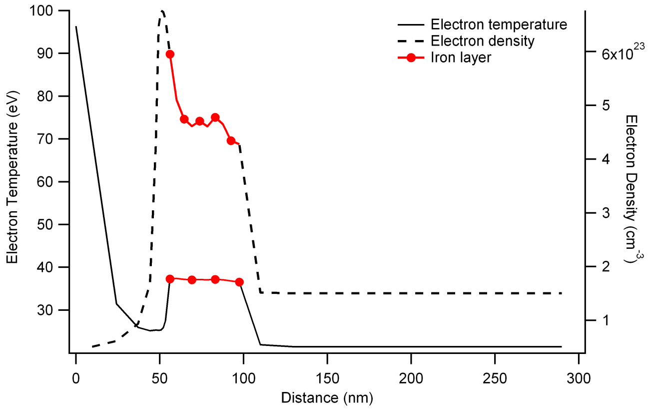

Figure 5.9: Cross section of sample electron temperature T_e and electron density n_e as a function of distance from the target surface immediately after laser irradiation simulated using the HYADES code at a peak intensity of 3 × 10^{16} Wcm^{-2} calculated with a flux limiter of 0.05 and 10% hot electron energy dump in the target. A pre-pulse starting at time - 70ps as measured in the experiment followed by the 35fs pulse at time '0ps' is assumed for the simulation.

Simulated values of transmission T using a revised IMP opacity model are superimposed on the fig. 5.5 experimental transmission results with different values of the flux limiter f and assuming either (i) a model of hot electron target heating with a dump of 10% of the laser energy distributed through the target proportional to the density at time 0 ps, or (ii) no hot electron target heating. With the hot electron heating, the simulated transmissions T are in best agreement with the measured transmissions with flux limiter f = 0.03 - 0.05. Without hot electron heating, the simulated transmissions with lower flux limiters ($f < 0.1$) do not correctly predict the rapid rise in EUV transmission observed at early times (10 ps), and a value $f \geq 0.1$ best fits the late-time transmissions. Little agreement is seen with a flux limiter of 0.03 without hot electron heating. With or without hot electron heating, the HYADES code predicts an absorption fraction A $\approx$

30% due to inverse bremsstrahlung and resonance absorption - in agreement with measurements and other simulations at the same irradiance [118]. Hot electron target heating with 5 - 10% of the laser energy has been observed previously for similar irradiation conditions [123, 124]. Resonance absorption typically couples 20% -30% of the laser energy into hot electrons under similar irradiation conditions [125]. Using the NIST ESTAR database values of electron ranges in solids as a function of electron energy [126] and assuming a Maxwellian distribution of hot electron energies with a characteristic temperature of 8.7keV (see chapter 2.1.6 equation 2.15) $\approx$30% of the electrons will be stopped and deposit energy in the target giving a maximum value of $\approx 10\%$ of the laser energy deposited into the target by hot electrons. The HYADES simulations show that the iron layer in the target for the times ($<$ 130 ps) where transmission is measured (fig. 5.5) has densities greater than 10^{-2} gcm^{-3} and so the iron ionization balance is consequently in LTE and so the use of an opacity model (IMP) assuming LTE is valid. An LTE average atom model of ionisation was also used in the HYADES simulations.

5.4 Opacity Data Comparisons

Two sets of IMP iron opacity data have been compared. The original IMP [77] data uses ion configurations based on placing quantum shells in one of 3 groups. Core shells are assumed to be fully occupied. Rydberg shells are assumed to be empty with 1 valence shell which has a varying level of occupation. A more recent set of IMP data has several improvements [78] including a greater number of possible atomic configurations which can contribute significantly to the opacity. The improved IMP data allows for ion configurations with up to 3 open valence shells with significant populations.

The revised IMP opacity data was found to give better agreement with our measured EUV transmissions. The explanation for this can be seen in fig. 5.10 which compares both sets of IMP

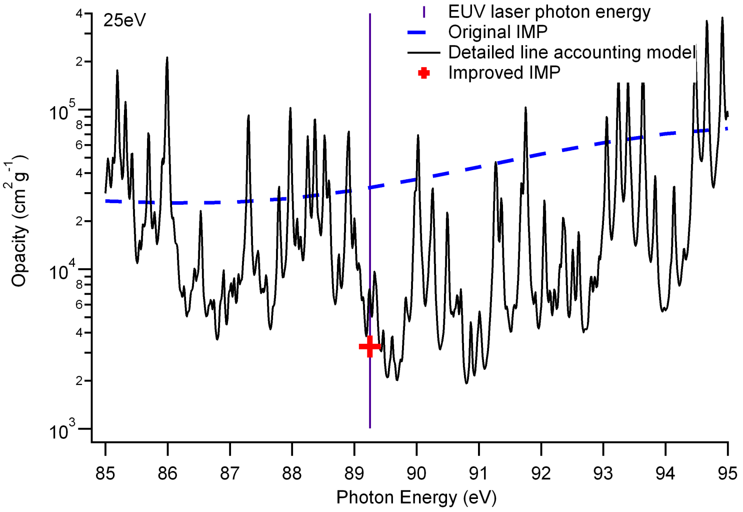

Figure 5.10: Comparison of different opacity models of iron in the 85eV - 95eV photon energy region at a density of 0.008gcm^{-3} and a temperature of 10eV. The solid line is a detailed line accounting prediction from the York opacity model [80] using atomic data from the Opacity Project [21]. Data from the IMP opacity model [77] which is accurate for spectrally broad backlighter calculations is also shown (cross is revised IMP data, dashed line original IMP data). The vertical line shows the photon energy of the EUV laser.

opacity data with frequency dependent opacities calculated from the Opacity Project atomic data [21, 80]. Modelling accurate plasma opacities, in particular for medium to high Z materials, where there are a large number of possible bound-bound transitions over a range of ionisation states, is complex and computationally expensive. Code efficiency approximations such as the IMP opacities are required which reduce spectral detail as most opacity applications are used for spectrally broad radiation spectra and not the extreme narrow-band emission ($\frac{\lambda}{\Delta\lambda} \approx 10^3 - 10^4$) from the EUV laser. From fig. 5.10, we see that the EUV laser with its characteristic narrow spectral width is positioned between iron absorption lines giving a lower opacity largely unaffected by bound-bound transitions . Using fig. 5.10, measurements such as our EUV transmission measurements could also be used to measure the accuracy of the iron absorption line photon energies calculated by the Opacity Project as the EUV laser photon energy is known to < 0.1eV accuracy [122]. Accuracies of Opacity Project line wavelengths have previously been estimated to be 1% - 4% [127].

5.5 Further Work

This EUV transmission method has potential as a simple diagnostic of energy transport through laser heated materials. However, as can be seen in fig. 5.5 this method is limited by errors due to the limited spatial uniformity and shot to shot variations of the EUV laser source. One solution is to set-up an experiment so that the differences in transmission are large enough for different conditions so that even without large reductions in error, for example via improvements to spatial uniformity, distinctions between different heat transport conditions can be made.

One method is to use a double heating pulse. An initial lower intensity femtosecond pulse separated from the main heating pulse by 10s of picoseconds focused on to a tamped target creates a pre-plasma. This expanded target with a larger scale length for the femtosecond main pulse to interact with should lead to a large difference between thermal electron conduction heating and the instantaneous heating after the heating pulse throughout the target by hot electrons. Using the first heating pulse as a prepulse allows more accurate characterisation and modelling of the plasma profile. With tuning of the prepulse timing and energy, it is possible to change the experimental conditions.

Initial simulations of the double pulse method assume laser properties, set-up and targets similar to the previous experimental work on LASERIX (see fig. 5.1). A prepulse of 5% of the main pulse intensity is used with a main pulse of intensity 3×10^{16}Wcm^{-2} focused to a spot size of $<50\mu$m are assumed. A pulse length of 35fs for both pulses is assumed. The 13.9nm EUV laser properties are as before, with a $\approx$5ps pulse length and a energy of $<1\mu$J. Plastic tamped iron targets as used in the previous experiment (50nm CH, 50nm Fe, 200nm CH see fig. 5.1) were modelled.

The optimum prepulse and main pulse separation was studied. Fig. 5.11 shows the electron density as a function of time for pulse separations of 20ps and 100ps. A flux limiter of 0.05 and

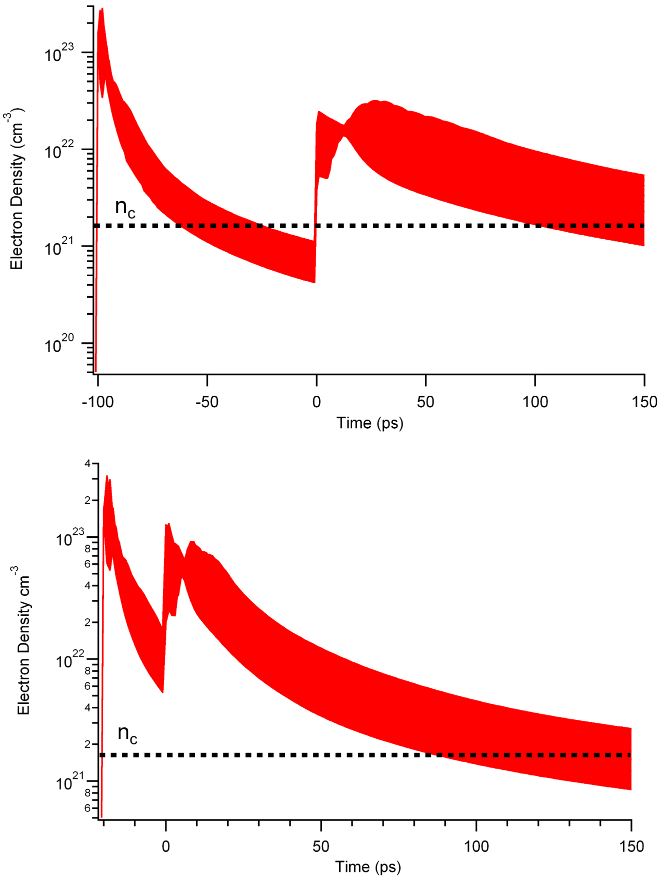

Figure 5.11: Sample target electron density n_e within the iron layer as a function of time from the arrival time of the main heating pulse for 20ps and 100ps pulse separations. Data is simulated using the HYADES code at a peak 2nd pulse intensity of 3×10^{16} Wcm^{-2} with a 5% prepulse calculated with a flux limiter of 0.05 and 10% hot electron energy dump in the target. The critical electron density for 800nm radiation is indicated by a dashed line

a 20° irradiation angle are assumed. The critical density for 800nm radiation is indicated. This shows for a 100ps pulse by the time the 2nd pulse arrives the density is subcritical throughout the target. The density drops below critical at -60ps indicating a pulse separation <40ps is required. A 20ps pulse separation as shown in fig. 5.11 is used for the rest of the simulations. The sudden rise in the electron density at 0ps is from the increase in the average ionisation of iron by a factor of 10 due to the arrival of the second pulse. Fig. 5.12 shows maximum ionisation increases from just over 1.5 before the main pulse arrives to over 15 afterwards.

Fig. 5.13 shows the 20ps pulse separation for flux limiters between 0.03 and 0.1, with and

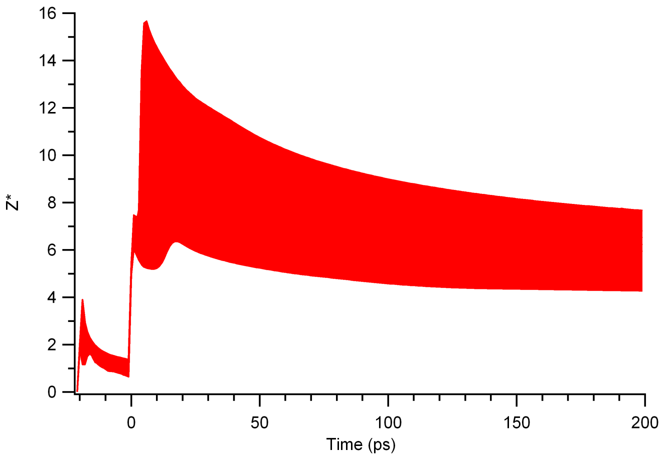

Figure 5.12: Sample target average ionisation Z^* within the iron layer as a function of time from the arrival time of the main heating pulse for a 20ps pulse separations. Data is simulated using the HYADES code at a peak 2nd pulse intensity of 3 × 10^{16} Wcm^{-2} with a 5% prepulse calculated with a flux limiter of 0.05 and 10% hot electron energy dump in the target.

without 10% of the laser energy deposited into hot electrons. A 20° irradiation angle is assumed. A separation between transmission with and without hot electron transport of ≈0.2 in transmission for a flux limiter of 0.05 can be seen, indicating that a difference greater than the typical error size (≈ 0.05 - 0.1 in transmission in fig. 5.5) can be seen between hot electron and thermal transport. Flux limiter differences still appear difficult to distinguish within these errors.

The angle of the beam onto the target can be varied to change the level of resonance absorption as the amount of resonance absorption should directly effect the level of hot electron heating. Resonance absorption and vacuum heating at these intensities ($I\lambda^2 \approx 10^{16}$Wcm^{-2}) will dominate hot electron production meaning hot electron heating will be minimum at 0° and thermal conduction will dominate. Hot electron heating will then peak at the peak angle for resonance absorption in the target which is predicted using a density scale length to wavelength ratio of $\approx 1 - 0.1$ from plots such as shown in fig. 5.7. Using the method described in chapter 2 subsection 2.1.4 a peak angle of ≈40 degrees is predicted. An angle of 40 degrees is also predicted by HYADES and Gibbon and Bell [37] for this scale length range. Simulations changing the irradiation angle between 0° and 40° at a constant flux limiter of 0.05 with and without energy deposited within hot electrons are shown in Fig. 5.14. No hot electrons have been added at 0° to reflect the predicted minimum in hot electron production, while 10% of the laser energy is dumped into hot electrons at 20° and 40° with an extra curve for 20% hot electrons at 40° to show the effect of a maximum in absorption.

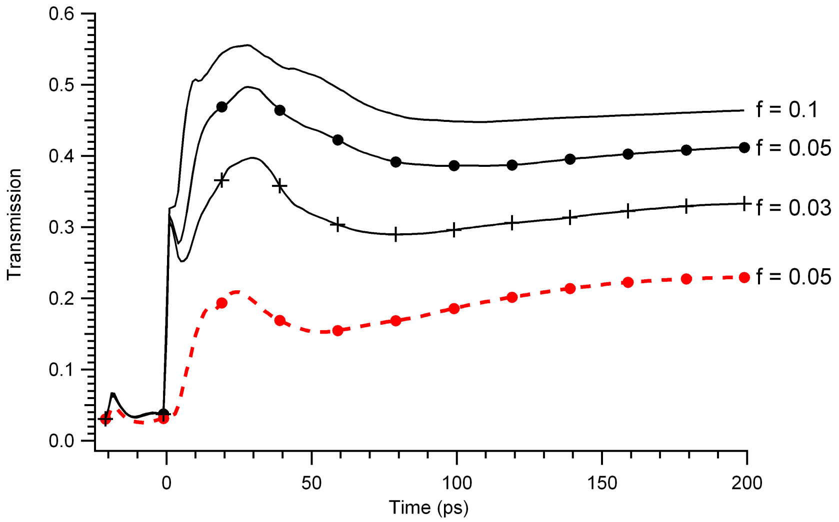

Figure 5.13: Transmission of EUV laser radiation at 89 eV as a function of time through a tamped 50 nm thick iron target. The target is irradiated at 0 ps by a 3 × 10^{16} Wcm^{-2} peak irradiance pulse of 35 fs duration, with a 35fs prepulse at 5% of the main irradiance arriving 20ps before. Simulation results using the HYADES code and revised IMP opacities are shown for various values of flux limiter (as labelled) calculated assuming (i) energy transport occurs via thermal conduction only (dotted curve) and (ii) hot electrons dump a fraction 10% of the laser pulse energy through the target and then energy transport occurs via thermal conduction (solid curves).

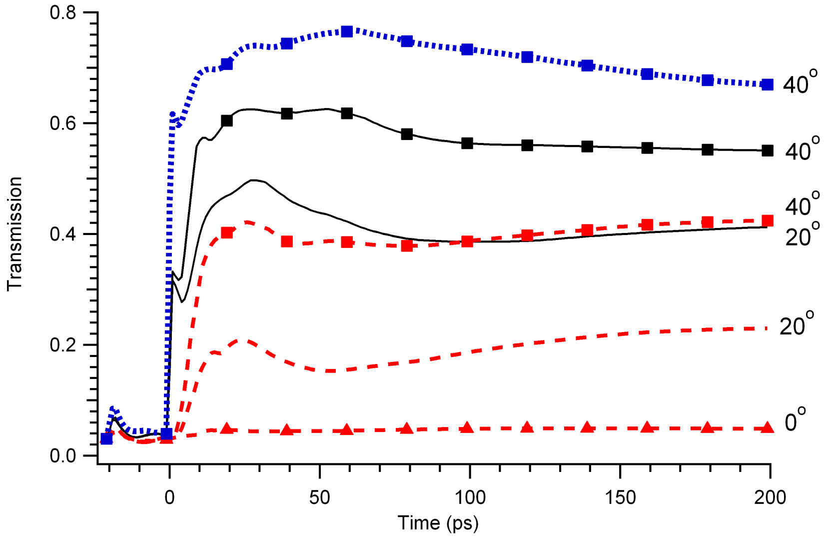

Figure 5.14: Transmission of EUV laser radiation at 89 eV as a function of time through a tamped 50 nm thick iron target. Simulation results the HYADES code and revised IMP opacities are shown for various incident angles (as labelled) calculated assuming (i) energy transport occurs via thermal conduction only (dashed curves), (ii) hot electrons dump a fraction of the laser pulse energy through the target and then energy transport occurs via thermal conduction (solid and dotted curves). Hot electrons are included at a fraction of 10% of the laser energy at 10° and 20° and 10% and 20% for 40°, assuming 40° is the peak angle for resonance absorption

5.6 Summary

The work in this chapter has shown that a rapid drop in opacity of iron with ionization enables measurements of the transmission of EUV laser pulses at 13.9 nm to act as a signature of the heating of thin (50 nm) iron layers with 50 nm thick parylene-N (CH) overlay irradiated by 35 fs pulses at an irradiance of $\approx 3 \times 10^{16}$ Wcm^{-2}. EUV transmission measurements at different times after irradiation have been compared to fluid code simulations of various heating scenarios. Best agreement is seen with the target being instantaneously heated by hot electrons with approximately 10% of the laser energy, followed by thermal conduction with a flux limiter of $\approx$ 0.03 - 0.05 or with no hot electron heating and a higher flux limiter of $f = 0.1$.

There is scope for further work using the the EUV transmission method described in this chapter, with potential for improvements to errors in measurements of transmission possible with improvements to beam uniformity. An alternative method using a double pulse set-up also allows improved transmission measurements of hot electron heating. The extent of hot electron target heating and the value of the flux limiter are both critical issues for inertial fusion research. Data such as obtained in this work is critical for the development of a predictive simulation capability that will render the development of successful inertial fusion experiments possible without substantial empirical design iteration on large facilities which is both time consuming and costly.

Chapter 6

Transmission profiles of laser - irradiated solid targets using coherent extreme ultra - violet radiation

6.1 Introduction

Experiments undertaken to record the transmission of extreme ultraviolet (EUV) light through a laser irradiated target can record the spatial variation of transmission. Diagnostics relevant to imaging with coherent light include interferometry [128–130] and the use of a Shack-Hartmann wavefront sensor [105] (see chapter 3 subsection 3.3). Another simple diagnostic, which is investigated here, is the recording of the transmission profile of coherent probing ultra-short wavelength radiation through a laser irradiated target. Transmission effects have been examined in the past [69, 130, 131] (see also chapter 5), but here it is shown that phase front effects associated with the real component of refractive index in the laser-plasma material can affect the transmitted beam profile and hence act as a diagnostic of the laser-plasma interaction. The distortion of the phase front of the coherent beam in passing through a target may also prevent the accurate imaging of the target.

The refractive index η of a material at wavelength λ can be written as (see chapter 2 subsection 2.3.7) $\eta = 1 - \delta + i\beta$, where the real part 1 - δ determines the phase velocity of radiation and the imaginary component $\beta = \left(\frac{\lambda}{4\pi}\right)\alpha$, where α is the absorption coefficient of the material. The two components of refractive index are related to dimensionless scattering form factors f_1, f_2 using:

$$\delta = f_1 \left(\frac{n_i}{2n_{crit}} \right) \tag{6.1}$$

$$\beta = f_2 \left(\frac{n_i}{2n_{crit}} \right) \tag{6.2}$$

where n_i is the ion or atom density and n_{crit} is the critical density for the radiation. The EUV optical properties of neutral materials are tabulated in terms of f_1 and f_2 [83], but there are no tabulations for ionised material. Some optical constants of solid unionised materials were measured in chapter 4.

This chapter outlines a procedure for calculating plasma refractive index values η from calculated absorption coefficients where an absorption edge structure dominates and then determines the total refractive index allowing for free plasma electrons and the presence of neutral atoms. Examples of possible radial phase profiles of the EUV radiation at the rear of a sample target are shown and a Fourier transform technique is then used to determine the far field intensity profile of the EUV beam.

Probing through laser-plasma targets samples (i) regions of hot plasma in the expanding plasma plume where free electrons dominate the refractive index and normally $\eta < 1$, (ii) low temperature ablated material between the critical and ablation surfaces where η can be greater than unity due to interactions with ions and (iii) solid unionised material with η equal to the room temperature solid material refractive index. In the EUV, (ii) is normally the only region where η is greater than unity (see e.g. [132]), so there is high potential for obtaining unique signature effects of this region, which has been notoriously difficult to diagnose. The next sections uses a hydrodynamic code coupled with a refractive index post - processor to demonstrate these effects on on the phase of EUV radiation through a laser heated solid aluminium target.

6.2 HYADES Modelling

The one-dimensional radiation hydrodynamics code HYADES [30] (see chapter 3 section 3.5 for more details), was used to simulate the laser irradiation of 800nm thick aluminium at peak irradiance $2 \times 10^{14}\mathrm{Wcm}^{-2}$ in a pulse of 35fs duration at normal incidence. An experiment under these irradiation conditions has been undertaken by Fajardo et al [133] with measurements of phase fronts of probing harmonics obtained using a Shack - Hartmann detector. HYADES outputs electron temperatures, average ionisation and electron density as a function of time and distance through the target. From the HYADES output, the EUV high harmonic transmission and phase shift through the target at a photon energy of 45eV were calculated using a refractive index post-processor.

The HYADES code uses the Los Alamos Sesame library [108] for the equation of state of the plasma material. Laser energy deposition in the expanding plasma profile is modelled by calculating the rate of inverse bremsstrahlung absorption of the laser energy (there is no resonance absorption modelled due to the normal incidence of the beam). The intensity of the input heating laser pulse was $2\times 10^{14}\mathrm{Wcm}^{-2}$ with a wavelength of 800nm and a 35fs Gaussian temporal profile.

6.3 Refractive Index Model

6.3.1 Opacity Calculations

Using the HYADES output of electron density and temperature for each cell in the simulation, the distribution of ionised states within each cell was calculated using the Saha - Boltzmann equation. The method of calculating the ionised state distribution with the Saha - Boltzmann equation is discussed in chapter 2 section 2.2 . The density of electrons and ions in each ionisation state was used to evaluate the bound - free and free - free absorption coefficient (α_{total}) using :

$$\begin{aligned}\alpha_{total} = \frac{4e^6}{3m_e hc}\sqrt{\left(\frac{2\pi}{3m_e k_B T_e}\right)} n_e \nu^{-3}\left(1-\exp\left(-\frac{h\nu}{k_B T_e}\right)\right)\cdot \\ \sum_{Z=0}^{Z_{max}} n_{iZ} Z^2 \left[\overline{g}_{ff} + \overline{g}_n \frac{\zeta}{n^3}\frac{I_{pZ}}{k_B T_e}\exp\left(\frac{I_{pZ}}{k_B T_e}\right) + \right. \\ \left. \sum_{m=n+1}^{\infty} \overline{g}_m \frac{2Z^2 R_y}{m^3 k_B T_e}\exp\left(\frac{Z^2 R_y}{m^3 k_B T_e}\right)\right] \end{aligned} \tag{6.3}$$

where e is the electronic charge, m_e is the mass of an electron, h is Planck's constant, c is the speed of light in a vacuum, k_B is the Boltzmann constant, T_e is the electron temperature, n_e is the electron density and n_{iZ} is the ion density of an ionisation state Z, ν is the frequency, ζ is the number of electrons in the ground state n, where n is the ground state principle quantum number, I_{pZ} is the ground state ionisation energy, R_y is the Rydberg energy, and $\overline{g}_n$, $\overline{g}_{ff}$ and $\overline{g}_m$ are Gaunt factors. Equation 6.3 has three contributions to the total absorption coeffcient: free - free absorption, the energy absorbed by bound - free absorption from ground state electrons and the contribution to the bound - free absorption by electrons in excited states (see chapter 2 section 2.3 for a description of these absorption mechanisms). The total absorption coefficient is then the sum of the absorption coefficient from all energy levels over all ionisation states. The opacity σ_{total} of the plasma material is related to the absorption coefficient by $\sigma_{total} = \frac{\alpha_{total}}{\rho}$, where ρ is the material density.

In equation 6.3, $\overline{g}_n$ = 0, when I_{pi} is less than the photon energy. Likewise $\overline{g}_m$ = 0, when $\left(\frac{Z^2 R_y}{m^3}\right)$ is less than the photon energy. Calculated values of Gaunt factors as a function of photon energy for all electronic shells are taken from Karzas and Latter (1961) [55] with $\overline{g}_{ff}$ = 1 assumed. A further contribution to the opacity from unionised atoms is calculated as the fraction of unionised atoms within the material multiplied by the solid opacity taken from the CXRO database [79].

From the calculated absorption coefficient the transmission (T) within each cell can be found using $T = \exp\left(-\alpha_{total}\Delta x\right)$, where Δx is the cell thickness. The total transmission is the product of the transmissions through each cell.

Figure 6.1 shows a sample HYADES output of electron density and electron temperature as a function of depth in the target at times from 1ps - 15ps after the arrival of the heating pulse. Over the first 15ps, only the first $\approx$ 200nm thickness of the sample is heated, with a peak temperature of $\approx$ 10eV and high electron densities close to 10^{23}cm^{-3}.

6.4 Real Refractive Index Calculations

The real part of the refractive index deviation from unity, δ, of the heated target is calculated from the contribution of the free electron refractive index, the bound electron refractive index dominated by the absorption edges at 92.4eV for Al^{+}, 105.4eV for Al^{2+} and 120eV for Al^{3+} plus the fraction of the solid refractive index value depending on the population of neutral atoms. The electron and ion densities of ionisation states were calculated using the same Saha - Boltzmann method used to calculate the imaginary refractive index. The real part of the free electron refractive index, δ_{free} is given by $\delta_{free} = \frac{n_e}{2n_{crit}}$, where n_e is the electron density and n_{crit} is the critical density given by $n_{crit} = \frac{1.1\times10^{21}}{\lambda_{\mu m}^2}$cm^{-3}. Here $\lambda_{\mu m}$ is the probing wavelength in microns. The bound electron contributions, δ_{bound} for each ionisation stage is given by $\delta_{bound} = f_1\frac{n_i}{2n_{crit}}$, where n_i is the ion

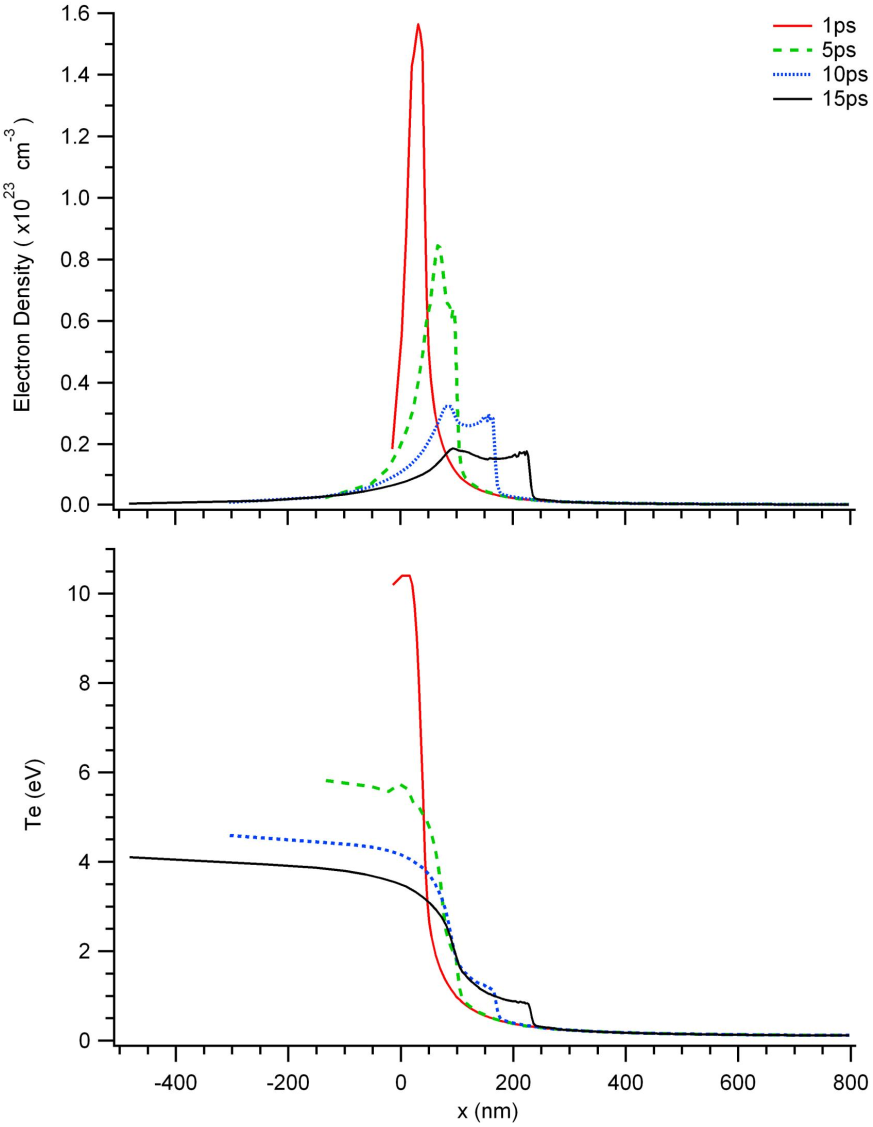

Figure 6.1: Electron density and electron temperature at 1, 5, 10 and 15ps after the arrival of the heating beam as a function of depth x through the aluminium target. The laser at irradiance 2×10^{14}Wcm^{-2} with 35fs duration is incident from the left on to an initially solid aluminium target of 800nm thickness.

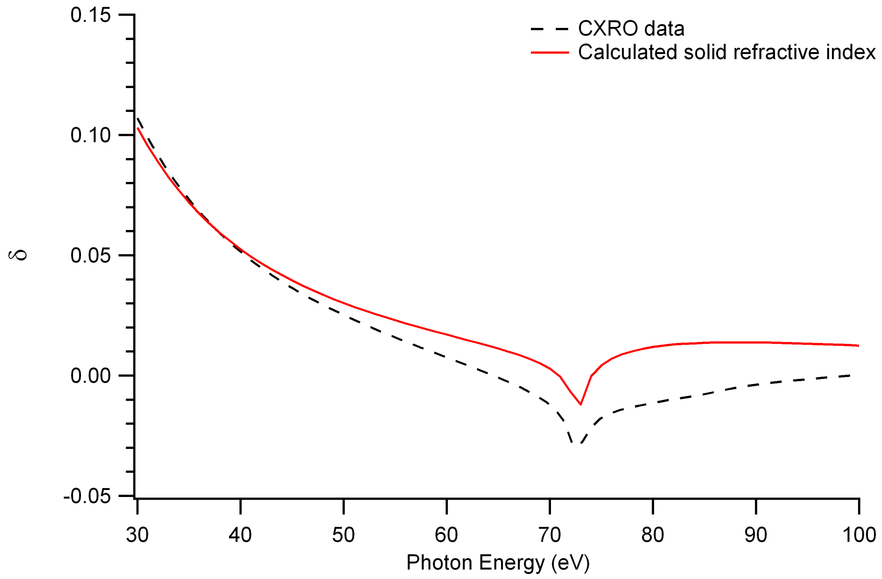

Figure 6.2: The real refractive index δ for solid unionised aluminium calculated using Eq. 6.6 (red solid line) and from the CXRO database (dashed black line)

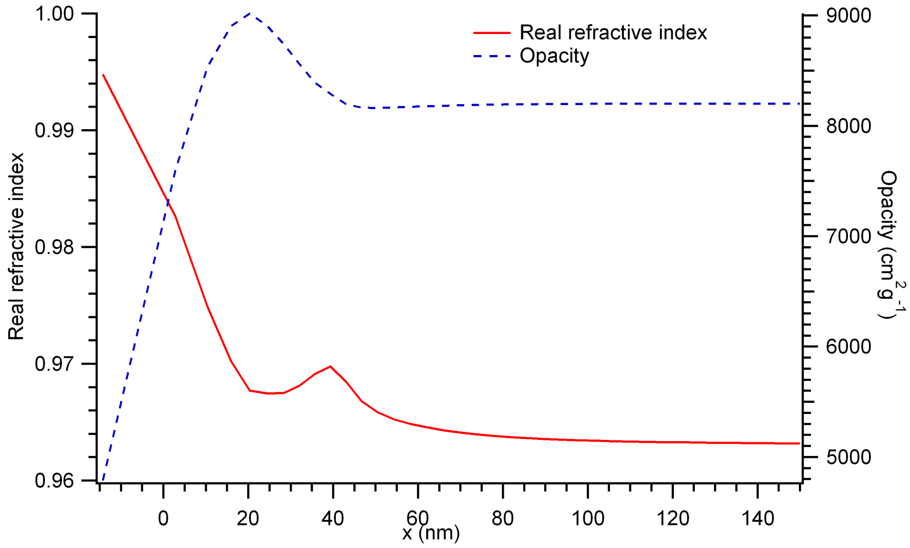

Figure 6.3: Opacity (blue dashed line) and refractive index (red solid line) as a function of distance through an 800nm thick aluminium sample 1ps after heating by a 2×10^{14}Wcm^{-2}, 35fs heating pulse

density and f_1 is the scattering form factor.

The solid refractive index value for f_1 is taken from the CXRO database values [79]. The bound electron scattering form factor f_1 for ions is calculated from the Kramers - Kronig relationship. The Kramers - Kronig relationship can be used to express the real part of the scattering form factor for neutral atoms and ions as a function of the imaginary component f_2 using:

$$f_1(\omega) = -\frac{2}{\pi}\int_0^\infty \frac{u f_2(u)}{u^2-\omega^2}du \tag{6.4}$$

where the integration is over all frequency. The imaginary component of the form factor f_2 is related to the absorption coefficient by $\alpha = \frac{4\pi}{\omega} n_i c r_e f_2$, where r_e is the classical electron radius and ω is the photon angular frequency. Absorption with a variation $\propto \omega^{-3}$ above the absorption edge at energy E_β is used in the simulations. Equation 6.4 can then be solved for this absorption profile as follows:

Rearranging α to give f_2, assuming $\alpha = \frac{aE_\beta^2}{\omega^3}$, where a is a constant related to the height of the absorption edge, and substituting to 6.4 we obtain:

$$f_1(\omega) = -\frac{aE_\beta^2}{2\pi^2 n_i c r_e}\int_{\omega_\beta}^\infty \frac{1}{u(u^2-\omega^2)}du \tag{6.5}$$

Integrating and substituting in $f_2\left(\frac{E_\beta}{\hbar}\right) = \frac{a\hbar^2}{4\pi n_i c r_e}$ gives:

$$f_1(\omega) = f_2\left(\tfrac{E_\beta}{\hbar}\right)\frac{1}{\pi}\frac{E_\beta^2}{(\hbar\omega)^2}\ln\left(\left|1-\frac{(\hbar\omega)^2}{E_\beta^2}\right|\right) \quad . \tag{6.6}$$

This formula for the scattering form factor has been used to find the solid unionised value of δ for aluminium to allow comparison to the tabulated values of δ from the CXRO database [79] in fig. 6.2. Here the free electron refractive index uses the density of conduction band electrons. Good agreement is seen for lower values of photon energy with a larger deviation seen around the edge due to the approximation used for the edge structure. The agreement at 45eV, the photon energy used in the following simulations is good.

The phase shift of electromagnetic radiation passing through a material is calculated using:

$$\phi = \int \eta \frac{2\pi}{\lambda} dx \tag{6.7}$$

where η is the total real refractive index, $\int dx$ is an integral over the thickness of the target and λ is the wavelength. Figure 6.3 shows the opacity and real part of the refractive index as a function of the distance through the target at 1ps. Changes in opacity and refractive index in the heated region can be seen.

Little change is seen in transmission through the target due to the large remaining unheated solid density material, though the phase shift compared to a solid unirradiated target is found to be significant at 3.9 radians, the potential effects of these large phase shifts are discussed in the next section. Fig 6.4 shows the contribution to the real part of the refractive index δ from free electrons, bound electrons and the solid material.

6.5 Far Field Phase Distributions

To predict EUV propagation to a CCD detector, the image of the target in the far field limit is calculated by performing a Fourier transform of the complex electric field at the target. We assume that the 45eV probe radiation is incident onto the target in a Gaussian beam with a FWHM of 100μm. The intensity at the rear of the target is assumed to have a corresponding Gaussian shape assuming the small changes in transmission (as described above at the peak of the distribution) have little radial effect on the intensity so that it remains close to Gaussian at the rear of the target.

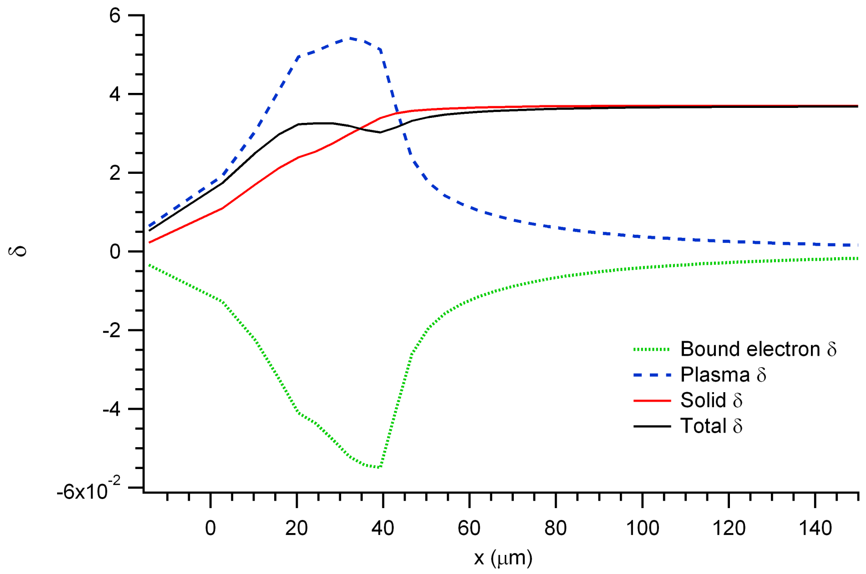

Figure 6.4: Free electron, bound electron and solid material contribution to the real part of the refractive index as a function of distance through an 800nm thick aluminium sample 1ps after heating by a 2×10^{14}Wcm^{-2}, 35fs heating pulse.

A range of phase distributions at the rear of the target are studied (see Figure 6.5), a planar or constant phase, a curved wavefront, a Gaussian wavefront and a example of a wavefront that may be caused by irregular irradiation by a heating pulse - for example by a ring shaped focal spot which may lead to structure in radial target heating.

Figure 6.6 compares different intensity distributions resulting from different phase distributions at 1.5m from the target. Each simulation assumes the same Gaussian intensity distribution at the target. Constant phase leads to no change in the form of the Gaussian intensity distribution as expected. A wavefront of assumed Gaussian shape with peak phase shift of 3.9 radians and FWHM of 100μm leads to side peaks and a curved wavefront peaking at 3.9 radians with a $\approx x^2$ profile leads a similar intensity structure as the planar phase data with extra side peaks appearing in the intensity distribution. The irregular heating ring shaped wavefront results in an intensity profile different to the Gaussian phase or constant phase wavefronts, illustrating the possibility for reconstructing the probing beam phase at the target from the intensity profile at some distance from the target, which could indicate the degree of heating uniformity.

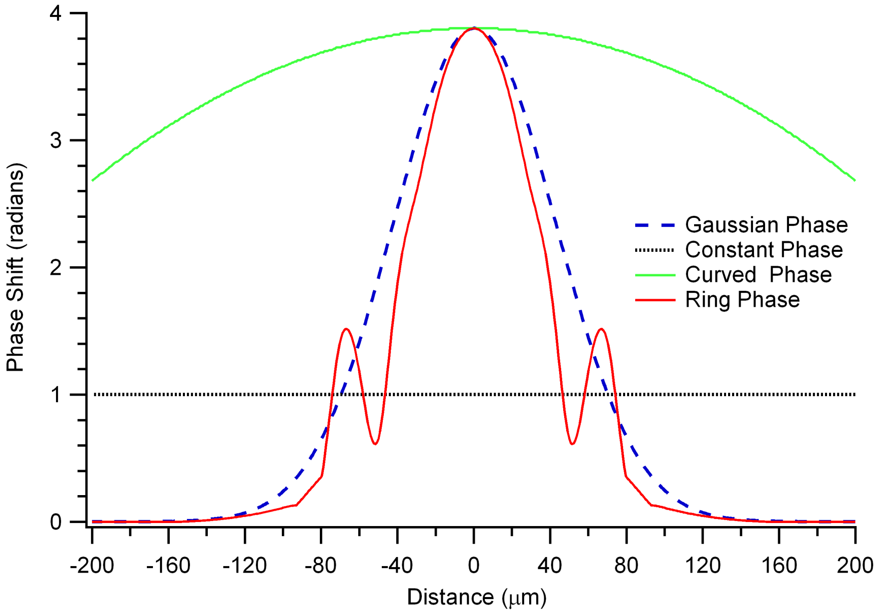

Figure 6.5: Examples of different phase distributions in 45eV EUV radiation at the rear of a laser heated target. A curved ($\approx x^2$) wavefront (solid green line), a Gaussian phase distribution (dashed blue line), a planar phase distribution (dashed black line) and an irregular distribution (red solid line) caused, for example, by a ring shaped focal spot. The peak phase shift of 3.9 radians is based on the simulations earlier in the chapter.

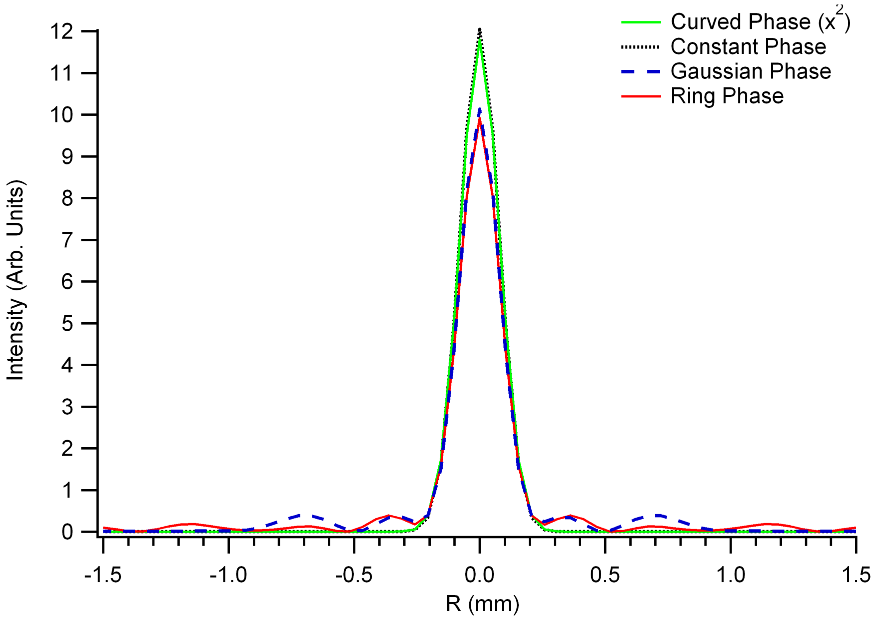

Figure 6.6: Intensity distribution of 45eV probing radiation at an detector 1.5m away from a target with different assumed phase distributions at the rear of the target: constant phase (black dotted line), Gaussian phase (blue dashed line), curved phase (green solid line) and the non Gaussian focal spot phase (red solid line). The intensity at the target is assumed to be Gaussian in all cases. The Gaussian variation is assumed to peak at 3.9 radians at the centre of the probing beam with a width (FWHM) of 100μm.

6.6 Summary

Simulations have been performed of the refractive index and transmission to 45eV radiation of a 800nm Al target heated by a 35fs, 2×10^{14}Wcm^{-2} 800nm laser pulse. The effects of EUV radial phase variations at the rear of a target on the intensity distribution at a detector 1.5m from the target have also been calculated. Although the irradiated aluminium target does not significantly affect the transmission of 45eV radiation, there are significant phase shifts in the probe beam. Phase variations due to variations in target heating radially affect the subsequent propagation of the radiation, suggesting a simple diagnostic measuring the footprint of coherent EUV radiation passing through an irradiated target is sensitive to radial variations of the target heating.

Chapter 7

Conclusions

This thesis has examined the application of extreme ultraviolet radiation to the probing of plasmas. The short wavelength of EUV radiation allows the probing of plasmas up to significantly higher density than optical radiation due to the higher critical density. However, the EUV optical properties of plasmas, such as the opacity, are also not well known and are difficult to model due to the large number of possible bound - bound transitions possible over a range of ionisation stages in high Z materials. This makes experimental measurements of EUV optical properties important for benchmarking codes. Laser produced plasmas have a variety of applications with EUV probing having the potential to measure energy transfer from thermal and hot electrons in plasmas relevant to inertial confinement fusion and the optical properties of plasmas relevant to both inertial confinement fusion and astrophysics.

Chapter 2 of this thesis outlines the background theory behind laser plasma interactions discussing ionisation, target expansion, energy transfer and hot electron production which are relevant to chapters 5 and 6 where laser produced plasmas are studied. Thermodynamic equilibrium population relations, in particular the Saha-Boltzmann equation (which is used to calculate ionisation state populations in chapter 6), plasma opacities and refractive indices are also discussed.

Different sources of coherent EUV radiation are discussed in chapter 3 with high harmonic generation, EUV lasers and XFELS described. The EUV optics required for the experimental work in chapter 5 are also introduced, along with the double slit interferometry technique used in chapter 4. The HYADES radiation hydrodynamic code, used to model plasmas produced by high power lasers in chapters 5 and 6 is also introduced.

Measurements of the optical constants of solid materials have been undertaken (chapter 4). The optical properties of solid materials are required to a high degree of accuracy for the production of EUV optics necessary for EUV lithography, EUV astronomy and plasma diagnostics. Materials such as aluminium are also often used as a filter material in high power laser experiments.

A double slit interferometry technique using high harmonics generated by focusing a 800nm, 35fs pulse length high power laser to an intensity of $\approx 10^{14}$Wcm^{-2} in an argon gas jet was used to simultaneously measure the complex refractive index of aluminium and imaginary part of the refractive index of iron between 17eV and 39eV. This data was compared to tabulated data and previous experimental work, showing good agreement between CXRO [79] database data and the experimentally measured values of Al β. Some deviation of tabulated data was seen in Al δ and Fe β values. The coherence of the high harmonic source was also measured to be 70 - 80% for harmonics up to harmonic 21 for the central 50μm of the beam. Futher work using this method could be performed using the double slit interferometer technique to simultaneously measure the real and imaginary part of the refractive index of plasma material. Extending the method to plasma measurements would have the extra constraint that the EUV source would have to be brighter than the plasma self emission and as the target would have to be replaced after every shot, data would need to be obtained within a single shot. Using this technique with plasmas would require a EUV laser or XFEL source due to their greater intensity than a high harmonic source.

Experimental work to use an EUV laser to probe a short pulse laser produced plasma has been carried out. This experiment used the drop in opacity due to ionisation to enable the transmission of an EUV laser to act as a signature of heat penetration into a plastic tamped 50nm iron target. The transmission of the 13.9nm EUV laser was measured at different times after irradiation by the 3×10^{16}Wcm^{-2}, 35fs, 800nm heating beam and compared to simulations to predict that the target is instantaneously heated by hot electrons with 10% of the laser energy, with the effect of the flux limiter also explored. Further experimental work to improve on this technique by adding a prepulse at 5% of the main pulse energy 20ps before the main 3×10^{16}Wcm^{-2} pulse is planned and simulations have been presented here (chapter 5). The interaction with the main pulse with the expanded target leads to larger differences in modelled transmission for different amounts of hot electron heating and thermal conduction allowing a clearer distinction of different heating scenarios even without large improvements to EUV beam uniformity.

Chapter 6 examined the diagnostic potential of EUV probing and imaging of high power laser produced plasmas. The transmission and refractive index at a photon energy of 45eV of a plasma produced by the irradiation of a aluminium target by a 2×10^{14}Wcm^{-2}, 35fs, 800nm laser pulse have been calculated. The transmission of the target is not seen to vary greatly from the solid value. However, the radial variations in the phase of the EUV radiation at the rear of the target at a radius of 50μm are shown to have an effect on the intensity distribution at a detector 1.5m away from the target. This phase variation at 50μm appears to be due to a drop in laser absorption at an intensity of 1×10^{14}Wcm^{-2}. This suggests a simple diagnostic of the footprint of coherent EUV radiation is sensitive to variations in the radial heating of a short pulse laser heated target.

Appendix A

List of publications

L. A. Wilson and G. J. Tallents. *"Probing of laser - irradiated solid targets using coherent extreme ultra - violet radiation. "* High Energy Density Physics **9** , 402, (2013).

L. A. Wilson, G. J. Tallents, J. Pasley, D. S. Whittaker, S. J. Rose, O. Guilbaud, K. Cassou, S. Kazamias, S. Daboussi, M. Pittman, O. Delmas, J. Demailly, O. Neveu, and D. Ros. *"Energy transport in short pulse laser heated targets measured using extreme ultra-violet laser backlighting."* Physical Review E **86** , 026406 (2012).

L. A Wilson, A. K. Rossall, G. J. Tallents, E. Wagenaars, C. Cacho, E. Springate, E. Turcu. *"Double slit interferometry to measure the EUV refractive indices of solids using high harmonics."* Applied Optics **51** , 2057, (2012).

L. A Wilson, A. K. Rossall, G. J. Tallents, E. Wagenaars, C. Cacho, E. Springate, E. Turcu. *"Double slit interferometry to measure the EUV refractive indices of solids using high harmonics"* Central Laser Facility Annual Report 2010-2011.

G. J. Tallents, D. S. Whittaker, L. A. Wilson, E. Wagenaars. *"Heating of high energy density plasmas using EUV and x-ray lasers."* Proceedings of SPIE **8140** , (2011).

D. Ros, O. Guilbaud, S. Kazamias, M. Pittman, K. Cassou, S. Daboussi, O. Neveu, J. Demailly, B. Cros, G. Maynard, B. Zielbauer, D. Zimmer, T. Khl, S. Lacombe, A. Klisnick, S. Bastiani-Ceccoti, G. J. Tallents, E. Wagenaars, L. Wilson, P. Zeitoun. *"Stable and long-time operation of a soft x-ray laser for user applications experiments."* Proceedings of SPIE **8140** , (2011).

Appendix B

Example of an HYADES input file

This is an example of a typical HYADES input file as used in chapter 5 to model short pulse laser irradiation of iron and chapter 6 to model short pulse laser irradiation of aluminium.

This file models the irradiation of a 800nm Al target by a 800nm, 35fs, 2×10^{14}Wcm^{-2} laser pulse at normal incidence. For this example 200 cells are used and the target is modelled for 20ps.

```
C Aluminium 200 cells

mesh 1 201 0. 4e-5

region 1 200 1 2.70 2.57e-5

material 1 13. 27. 1

eos 44 1

eos 1041 1

ioniz 1 4

group 1 40 0.01 10

C

C main laser pulse

source laser 0.8 1 1

gauss 5e-12 2e+21 40e-15 $ 35fs, 800nm gaussian pulse at normal incidence

C

pparray r dene te $ mesh point, electron density and electron temperature

C
```

```
parm postdt 100.e-15 $ output time step

parm editdt 100.e-15

parm tstop 20e-12 $ final time step

parm nstop 100000000

parm dtmin 1.e-25 $ minimum time step

parm dtmax 1.e-14 $ maximum time step

parm dt 1.e-16

parm lrdtrn 1 $ turn on radiation transport

parm flxlem -0.05 $ electron flux limiter

parm temin 2.57e-5 $ minimum temperature 25 deg C

parm xlram 1 $ select angle dependent resonance expression

parm xlrdsm 1 $ resonance absorption scale height multiplier

c
```

Appendix C

Code used to model the opacity and refractive index of short pulse laser heated aluminium

This IDL code is used in the work discussed in chapter 6 to model the opacity and refractive index of short pulse laser heated aluminium using the electron density and electron temperatures output by HYADES. This model first calculates the Saha - Boltzmann populations of each ionisation state (see chapter 2 section 2.2). These populations are then used to calculate the free - bound opacity and refractive index due to bound electrons. The free electron and solid material contribution to the opacity and refractive index are then also included (see chapter 6 section 6.3).

```
;;;;;;;;;;;;;;;;;;;;;;;;;;;;;;;;;;;;;;;;;;;;;;;;;;;;;;;;;;;;;;;;;;;;;;;;;
PRO opacity

; MODEL CALCULATING REAL AND IMAGINARY PARTS OF THE REFRACTIVE INDEX OF
; ALUMINIUNM USING SAHA BOLTZMANN POPULATIONS AND NEGLECTING BOUND BOUND
; OPACITIES

;;;;;;;;;;;;;;;;;;;;;;;;;;;;;;;;;;;;;;;;;;;;;;;;;;;;;;;;;;;;;;;;;;;;;;;;;
;SAHA POPULATION GENERATOR

; LOAD ARRAYS

ie = DBLARR(1,14) ;create the ionisation energy value array
OPENR,lun1,'Ie_al.txt',/get_lun ;open the file
READF,lun1,ie ;
;CLOSE,lun1 ;
FREE_LUN,lun1,/FORCE

ie_shift = DBLARR(1,14) ;create the shifted ionisation value array
OPENR,lun2,'Ie_al_shift.txt',/get_lun ;
READF,lun2,ie_shift ;
CLOSE,lun2 ;
```

```
FREE_LUN,lun2,/FORCE

de = DBLARR(1,14) ;create the degeneracy value array
OPENR,lun3,'degeneracy_al.txt',/get_lun ;
READF,lun3,de ;
CLOSE,lun3 ;
FREE_LUN,lun3,/FORCE

ionis = DBLARR(1,14) ;create the ionisation array
OPENR,lun4,'ionis.txt',/get_lun ;
READF,lun4,ionis ;
CLOSE,lun4 ;
FREE_LUN,lun4,/FORCE

e_gs = DBLARR(1,14) ;create the no. electrons in ground state value array
OPENR,lun5,'e_gs.txt',/get_lun ;
READF,lun5,e_gs ;
CLOSE,lun5 ;
FREE_LUN,lun5,/FORCE

s = DBLARR(1,14) ;create the n value array
OPENR,lun6,'n.txt',/get_lun ;
READF,lun6,s ;
CLOSE,lun6 ;
FREE_LUN,lun6,/FORCE

l3_edge = DBLARR(1,14) ;create the edge value array
OPENR,lun7,'e.txt',/get_lun ;
READF,lun7,l3_edge ;
CLOSE,lun7 ;
FREE_LUN,lun7,/FORCE

gaunt = DBLARR(4,14) ;create the gaunt factor value array
OPENR,lun8,'gaunt.txt',/get_lun ;
READF,lun8,gaunt ;
CLOSE,lun8 ;
FREE_LUN,lun8,/FORCE

n_e = DBLARR(200,201) ; load density array
OPENR,lun9,'dene.txt',/get_lun ;
READF,lun9,n_e ;
CLOSE,lun9 ;
FREE_LUN,lun9,/FORCE

te = DBLARR(200,201) ;create the te array
OPENR,lun10,'Te.txt',/get_lun ;
READF,lun10,te ;
CLOSE,lun10 ;
FREE_LUN,lun10,/FORCE
```

```
;;;;;;;;;;;;;;;;;;;;;;;;;;;;;;;;;;;;;;;;;;;;;;;;;;;;;;;;;;;;;;;;;;;;;;;;;;

;LOAD CONSTANTS

MASS_NUMBER = 26.98; al mass
HE_I = 13.6 ;Hydrogen ionisation in eV

READ, photon_energy, PROMPT ='Enter photon energy in eV (39, 42, 45 or 48)'

;;;;;;;;;;;;;;;;;;;;;;;;;;;;;;;;;;;;;;;;;;;;;;;;;;;;;;;;;;;;;;;;;;;;;;;;;;

; PHYSICAL CONSTANTS IN CGS UNITS

E = 4.80d-10
H = 6.63d-27
M_E = 9.11d-28
K = 1.38d-16
C = 29979000000

delta_free_total = DBLARR(200,201)
delta_bound_total = DBLARR(200,201)
delta_ground_total =DBLARR(200,201)
nreal = DBLARR(200,201)
final_opacity = DBLARR(200,201)
delta_total = DBLARR(200,201)
solid_total_array = DBLARR(200,201)
;;;;;;;;;;;;;;;;;;;;;;;;;;;;;;;;;;;;;;;;;;;;;;;;;;;;;;;;;;;;;;;;;;;;;;;;;;

FOR a = 0, 199 DO BEGIN
FOR b = 0, 200 DO BEGIN

; DERVIVED VALUES

t_k = (te(a,b) * 1.6d-19)/ 1.38d-23 ;temperature in kelvins
v = (photon_energy * 1.6d-19) / 6.63d-34 ;frequency

pop_ratio = DBLARR(1,14)
rel_pop1 = DBLARR(1,14)
charge1 = DBLARR(1,14)

pop_ratio = de * (3.d23 / n_e(a,b)) * ((te(a,b) / HE_I)^1.5) * $
  (-1* (ie_shift / te(a,b)))

pop_ratio(0,0) = 1

;;;;;;;;;;;;;;;;;;;;;;;;;;;;;;;;;;;;;;;;;;;;;;;;;;;;;;;;;;;;;;;;;;;;;;;;;;

; FIRST ITERATION
```

```
START = 1

rel_pop1(0,0) = START

        FOR i = 1, 13 DO BEGIN
        n = i-1
                rel_pop1(0,i) = rel_pop1(0,n) * pop_ratio(0,i)
        ENDFOR

charge1 = rel_pop1 * ionis

neutral_pop1 = n_e(a,b) / TOTAL(charge1)

;FINAL POPULATION CALCULATION

rel_pop = DBLARR(1,14)
charge = DBLARR(1,14)

rel_pop(0,0) = neutral_pop1

        FOR i = 1, 13 DO BEGIN
        n = i-1
                rel_pop(0,i) = rel_pop(0,n) * pop_ratio(0,i)
        ENDFOR

charge = rel_pop * ionis
ion_total = TOTAL(rel_pop)

neutral_pop = n_e(a,b) / TOTAL(charge)

;;;;;;;;;;;;;;;;;;;;;;;;;;;;;;;;;;;;;;;;;;;;;;;;;;;;;;;;;;;;;;;;;;;;;;;;;;
; FREE FREE OPACITY CALCULATION

ff = DBLARR(1,14)

ff = (((4D * E^6)/(3d*  M_E * H * C))*(((2d * 3.1415d)/ $
  (3 * M_E * K * t_k))^0.5)* ionis * ionis * (rel_pop) * $
    (n_e(a,b))*(1/(v^3))*(1-exp(-1*(photon_energy / te(a,b)))))

;;;;;;;;;;;;;;;;;;;;;;;;;;;;;;;;;;;;;;;;;;;;;;;;;;;;;;;;;;;;;;;;;;;;;;;;;;

; BOUND FREE OPACITY CALCULATION

; PART A

bf_a = DBLARR(1,14)
        FOR j=0, 13 DO BEGIN
                IF (ie(0,j) LT Photon_energy) THEN BEGIN
                        bf_a(0,j)=(exp(ie(0,j)/te(a,b)))*(ie(0,j)/te(a,b))* $
```

```
        ((e_gs(0,j))/(s(0,j))^3)
                ENDIF ELSE BEGIN
                        bf_a(0,j) = 0
                ENDELSE
        ENDFOR

bf_a(0,13) = 0

; PART B

gaunt_factor = DBLARR(1,14)
;Select gaunt factors
IF (photon_energy EQ 39)THEN BEGIN
        FOR gf = 0, 13 DO BEGIN
        gaunt_factor(0,gf) = gaunt(3,gf)
        ENDFOR
ENDIF
        IF (photon_energy EQ 42)THEN BEGIN
        FOR gf = 0, 13 DO BEGIN
        gaunt_factor(0,gf) = gaunt(2,gf)
        ENDFOR
ENDIF
        IF (photon_energy EQ 45)THEN BEGIN
        FOR gf = 0, 13 DO BEGIN
        gaunt_factor(0,gf) = gaunt(1,gf)
        ENDFOR

ENDIF
        IF (photon_energy EQ 48)THEN BEGIN
        FOR gf = 0, 13 DO BEGIN
        gaunt_factor(0,gf) = gaunt(0,gf)
        ENDFOR
ENDIF

bf_b = DBLARR(1,14)
        FOR bbf = 0, 13 DO BEGIN
                FOR r = 1, 8 DO BEGIN
                        ie_ex = ((ionis(0, bbf) + 1) * (ionis(0, bbf) + 1)
        * HE_I) / ((s(0, bbf) + r) * (s(0, bbf) + r))
                        IF (ie_ex LT Photon_energy) THEN BEGIN
        bbb =  gaunt_factor(0, bbf)*(((2d * (ionis(0, bbf) + 1) * $
          (ionis(0, bbf) + 1) * HE_I)/ (te(a,b) * (s(0, bbf) + r)^3))* $
            exp(((ionis(0, bbf) + 1) * (ionis(0, bbf) + 1)* HE_I)/ $
               (te(a,b) * (s(0, bbf) + r)^2)))
                        ENDIF ELSE BEGIN
        bbb = 0
                        ENDELSE
        bf_b(0, bbf) = bbb + bf_b(0, bbf)
```

```
                ENDFOR
        ENDFOR

bf_b(0,13)=0

; TOTAL BF OPACITY

bf = DBLARR(1,14)
FOR z=0, 13 DO BEGIN
                IF (ie(0,z) LT Photon_energy) THEN BEGIN
                        bf(0,z) = bf_a(0,z) + bf_b(0,z)
                ENDIF ELSE BEGIN
                        bf(0,z) = bf_b(0,z)
                ENDELSE
        ENDFOR

;;;;;;;;;;;;;;;;;;;;;;;;;;;;;;;;;;;;;;;;;;;;;;;;;;;;;;;;;;;;;;;;;;;;;;;;;

;TOTAL OPACITY ARRAY

IF (photon_energy EQ 39)THEN cold_opacity = 8691 ELSE $
        IF (photon_energy EQ 42)THEN cold_opacity = 8433 ELSE $
                IF (photon_energy EQ 45)THEN cold_opacity = 8083 ELSE $
                        IF (photon_energy EQ 48)THEN cold_opacity = 7682 ELSE $
        cold_opacity = 0

mass = MASS_NUMBER * 1.67d-24 * ion_total

opacity = DBLARR(1,14)
        FOR w=1, 13 DO BEGIN
        opacity(0,w) = ((bf(0,w-1)+1) * ff(0,w))/ mass
        ENDFOR

opacity(0,0)=cold_opacity

;;;;;;;;;;;;;;;;;;;;;;;;;;;;;;;;;;;;;;;;;;;;;;;;;;;;;;;;;;;;;;;;;;;;;;;;;
; FINAL OPACITY RESULTS

f = DBLARR(1,14)

        FOR p = 1, 13 DO BEGIN
                f(0,p)= 1
        ENDFOR

f(0,0) = rel_pop(0,0) / TOTAL(rel_pop)

final_opacity(a,b) = TOTAL (f * opacity)
final_opacity(a,0)=cold_opacity
```

```
PRINT, final_opacity(a,b)

;;;;;;;;;;;;;;;;;;;;;;;;;;;;;;;;;;;;;;;;;;;;;;;;;;;;;;;;;;;;;;;;;;;;;;;;;

;REAL REFRACTIVE INDEX - DELTA, NREAL

lambda = (6.63d-34 * C) / (photon_energy * 1.6d-19)   ; wavelength in cm

ncrit = 1.1d+21 / (lambda * lambda *1d8)

;PRINT, ncrit

;;;;;;;;;;;;;;;;;;;;;;;;;;;;;;;;;;;;;;;;;;;;;;;;;;;;;;;;;;;;;;;;;;;;;;;;;

;FREE ELECTRON REFRACTIVE INDEX

delta_free = 0

        FOR i = 0, 13 DO BEGIN
                delta_free = delta_free + (charge(0, i) / (2 * ncrit))
        ENDFOR

;;;;;;;;;;;;;;;;;;;;;;;;;;;;;;;;;;;;;;;;;;;;;;;;;;;;;;;;;;;;;;;;;;;;;;;;;

;BOUND ELECTRON REFRACTIVE INDEX

f1 = DBLARR(1,14)
l3_width = 3.05

        FOR i = 1, 9 DO BEGIN
                f1(0,i) = ((l3_width * (l3_edge(0,i) * l3_edge(0,i))) /( 3.14159 * $
      photon_energy * photon_energy )) * ALOG (SQRT((1-((photon_energy * $
        photon_energy )/(l3_edge(0,i) * l3_edge(0,i)))) * (1-(( $
          photon_energy * photon_energy )/(l3_edge(0,i) * l3_edge(0,i))))))
       ENDFOR

        FOR i = 10, 13 DO BEGIN
                f1(0,i) = 0
        ENDFOR

        IF (Photon_energy EQ 39)THEN solid = 0.055 ELSE $
                IF (Photon_energy EQ 42)THEN solid = 0.045 ELSE $
                        IF (Photon_energy EQ 45)THEN solid = 0.037 ELSE $
                                IF (Photon_energy EQ 48)THEN solid = 0.029 ELSE $
          solid = 0

delta_bound = DBLARR(1,9)

        FOR i = 1, 8 DO BEGIN
```

```
                delta_bound (0,i) = (rel_pop(0,i) * f1 (0,i)) / (2 * ncrit)
       ENDFOR

solid_total = solid * f(0,0)

PRINT, delta_bound

;;;;;;;;;;;;;;;;;;;;;;;;;;;;;;;;;;;;;;;;;;;;;;;;;;;;;;;;;;;;;;;;;;;;;;;;;

delta_total(a,b) =   TOTAL(delta_bound)+ TOTAL(delta_free)+ solid_total

nreal(a,b) = 1 - delta_total(a,b)

PRINT, delta_total(a,b)


;;;;;;;;;;;;;;;;;;;;;;;;;;;;;;;;;;;;;;;;;;;;;;;;;;;;;;;;;;;;;;;;;;;;;;;;;

;FRACTION tests

solid_total_array(a,b) = solid_total

delta_free_total(a,b) = TOTAL(delta_free)

delta_bound_total(a,b) = TOTAL(delta_bound)

ENDFOR
ENDFOR

;;;;;;;;;;;;;;;;;;;;;;;;;;;;;;;;;;;;;;;;;;;;;;;;;;;;;;;;;;;;;;;;;;;;;;;;;

;OUTPUT FILES

OPENW, lun11, 'Oout.txt',/get_lun
PRINTF, lun11, final_opacity,FORMAT = '(200A)'
CLOSE, lun11
FREE_LUN,lun11,/FORCE

OPENW, lun12, 'delta.txt',/get_lun
PRINTF, lun12, delta_total,FORMAT = '(200A)'
CLOSE, lun12
FREE_LUN,lun12,/FORCE

OPENW, lun13, 'delta_ff.txt',/get_lun
PRINTF, lun13, delta_free_total,FORMAT = '(200A)'
CLOSE, lun13
FREE_LUN,lun13,/FORCE

OPENW, lun14, 'delta_bb.txt',/get_lun
```

```
PRINTF, lun14, delta_bound_total,FORMAT = '(200A)'
CLOSE, lun14
FREE_LUN,lun14,/FORCE

OPENW, lun15, 'delta_gs.txt',/get_lun
PRINTF, lun15, solid_total_array,FORMAT = '(200A)'
CLOSE, lun15
FREE_LUN,lun15,/FORCE
;;;;;;;;;;;;;;;;;;;;;;;;;;;;;;;;;;;;;;;;;;;;;;;;;;;;;;;;;;;;;;;;;;;;;;;;;;

END
```

References

[1] D. Attwood, *Soft X-rays and Extreme Ultraviolet Radiation* (Cambridge University Press, 1999).

[2] L. B. Da Silva et al., Phys. Rev. Lett. **69**, 438 (1992).

[3] J. E. Bailey et al., Phys. Rev.Lett. **99**, 265002 (2007).

[4] R. Neutze, R. Wouts, D. van der Spoel, E. Weckert, and J. Hajdu, Nature **406**, 752 (2000).

[5] H. N. Chapman, A. Barty, M. J. Bogan, S. Boutet, M. Frank, S. P. Hau-Riege, S. Marchesini, B. W. Woods, S. Bajt, W. H. Benner, et al., Nature Physics **2**, 839 (2006).

[6] S. M. Vinko, O. Ciricosta, B. I. Cho, K. Engelhorn, H.-K. Chung, C. R. D. Brown, T. Burian, J. Chalupský, R. W. Falcone, C. Graves, et al., Nature **482**, 59 (2012).

[7] B. Nagler et al., Nature Physics **5**, 693 (2009).

[8] M. H. Key, Physics of Plasmas **14**, 055502 (2007).

[9] S. Atzeni and J. Meyer-ter Vehn, *The Physics of Inertial Fusion* (Oxford, 2004), 1st ed.

[10] J. lindl, Phys. Plasmas **2**, 3933 (1995).

[11] S. W. Haan et al., Phys. Plasmas **18**, 051001 (2011).

[12] J. Lindl et al., Phys. Plasmas **11**, 339 (2004).

[13] H. Shapley, Publications of the Astronomical Society of the Pacific **30**, pp. 42 (1918).

[14] F. J. Rogers and C. A. Iglesias, Science **263**, 50 (1994).

[15] R. Kippenhahn and A. Weigert, *Stellar structure and evolution* (Springer–Verlaq, 1990), 1st ed.

[16] A. C. Phillips, *The Physics of Stars* (Wiley, 1994), 2nd ed.

[17] J. E. Bailey et al., Phys. Plasmas **16**, 058101 (2009).

[18] S. Basu and H. M. Anitia, MNRAS **287**, 189 (1997).

[19] B. Paxton, Publications of the Astronomical Society of the Pacific **116**, 699 (2004).

[20] EZ - web, http://www.astro.wisc.edu/∼townsend/static.php?ref=ez-web.

[21] M. J. Seaton et al., MNRAS **266**, 805 (1994).

[22] J. N. Bahcall et al., Astrophys. J **618**, 1049 (2005).

[23] J. J. Drake and P. Testa, Nature **436**, 525 (2005).

[24] M. Asplund et al., Astron. Astrophys. **417**, 754 (2004).

[25] A. M. Serenelli et al., Astrophys. J **705**, L123 (2009).

[26] W. L. Freedman et al., Astrophys. J. **553**, 47 (2001).

[27] D. J. Majaess et al., MNRAS **398**, 263 (2009).

[28] F. J. Rogers and C. A. Inlesias, Astrophys. J. Suppl. Ser. **79**, 507 (1992).

[29] N. R. Simon, Astrophys. J. **260**, L87 (1982).

[30] J. T. Larsen and S. M. Lane, JQSRT **51**, 179 (1994), HYADES supplied by Cascade Applied Sciences inc. Larsen@casinc.com.

[31] L. M. R. Hobbs, Ph.D. thesis, PhD thesis, The University of York (2011).

[32] P. Gibbon, *Short Pulse Laser Interactions with Matter* (Imperial College Press, 2005), 1st ed.

[33] L. V. Keldysh, Soviet Physics JETP **20**, 1307 (1965).

[34] W. L. Kruer, *The physics of laser plasma interactions* (Westview, Boulder, 2003).

[35] S. Elizer, *The Interaction of High Power Lasers with Plasmas* (IOP publishing, 2002), 1st ed.

[36] D. C. Slater, G. E. Busch, G. Charatis, R. R. Johnson, F. J. Mayer, R. J. Schroeder, J. D. Simpson, D. Sullivan, J. A. Tarvin, and C. E. Thomas, Phys. Rev. Lett. **46**, 1199 (1981).

[37] P. Gibbon and A. R. Bell, Phys. Rev. Lett. **68**, 1535 (1992).

[38] A. R. Bell, Physics of Fluids **28**, 2007 (1985).

[39] J. Davies, A. Bell, M. Haines, and S. Guérin, Physical Review E **56**, 7193 (1997).

[40] a. Bell and R. Kingham, Physical Review Letters **91**, 035003 (2003).

[41] R. C. Malone, R. L. McCrory, and R. L. Morse, phys. Rev. Lett. **34**, 721 (1975).

[42] A. R. Bell, R. G. Evans, and D. J. Nicholas, Phys. Rev. Lett. **46**, 243 (1981).

[43] M. Rosen, H. Scott, D. Hinkel, E. Williams, D. Callahan, R. Town, L. Divol, P. Michel, W. Kruer, L. Suter, et al., High Energy Density Physics **7**, 180 (2011).

[44] R. E. Olson, L. J. Suter, J. L. Kline, D. A. Callahan, M. D. Rosen, K. Widmann, E. A. Williams, D. E. Hinkel, N. B. Meezan, G. A. Rochau, et al., J. Phys: Conf. Ser. **244**, 032057 (2010).

[45] D. W. Forslund, J. M. Kindel, and K. Lee, Phys. Rev. Lett. **39**, 284 (1977).

[46] P. Gibbon and E. Förster, Plasma Physics and Controlled Fusion **38**, 769 (1996).

[47] S. Wilks and W. Kruer, IEEE Journal of Quantum Electronics **33**, 1954 (1997).

[48] R. P. Drake, *High Energy Density Physics* (Springer, 2006).

[49] Y. Sentoku, T. E. Cowan, A. Kemp, and H. Ruhl, Physics of Plasmas **10**, 2009 (2003).

[50] J. D. Kmetec, C. J. Gordon, III, J. J. Macklin, B. E. Lemoff, G. S. Brown, and S. E. Harris, Physical Review Letters **68**, 1527 (1992).

[51] H. R. Griem, *Principles of Plasma Spectroscopy* (Cambridge University Press, 1997).

[52] H.-K. Chung, M. Chen, W. Morgan, Y. Ralchenko, and R. Lee, High Energy Density Physics **1**, 3 (2005).

[53] Y. B. Zel'dovich and Y. P. Raizer, *Physics of Shock Waves and High-Temperature Hydrodynamic Phenomena* (Dover Publications, 2002).

[54] D. Salzmann, *Atomic Physics in Hot Plasmas* (Oxford University Press, 1998).

[55] W. J. Karzas and R. Latter, The Astrophysical Journal Supplement Series **6**, 167 (1961).

[56] G. B. Rybicki and A. P. Lightman, *Radiative Processes in Astrophysics* (John Wiley & Sons, 1979).

[57] J. Balmer et al., Phys. Rev. A **40**, 330 (1989).

[58] M. H. Edwards et al., Phys. Rev. Lett **97**, 035001 (2006).

[59] S. J. Davidson et al., Appl. Phys. Lett. **52**, 847 (1988).

[60] C. Chenais-Popovics et al., JQSRT **65**, 117 (2000).

[61] D. J. Hoarty et al., HEDP **6**, 105 (2010).

[62] K. Nazir et al., Appl. Phys. Lett. **69**, 3686 (1996).

[63] P. T. Springer et al., Phys. Rev. Lett **69**, 3735 (1992).

[64] C. Chenais-Popovics et al., Astrophys. J. Suppl. Ser. **127**, 275 (2000).

[65] T. S. Perry et al., Phys. Rev. Lett **67**, 3784 (1991).

[66] J. M. Foster et al., Phys. Rev. Lett. **67**, 3255 (1991).

[67] C. A. Iglesias, JQSRT **99**, 295 (2006).

[68] H. Huang, Ph.D. thesis, The University of York (2008).

[69] M. H. Edwards, D. S. Whittaker, G. J. Tallents, P. Mistry, G. J. Pert, B. Rus, T. Mocek, M. Kozlová, J. Polan, A. Praeg, et al., Phys. Rev. Lett. **99**, 195002 (2007).

[70] D. H. Kalantar, M. H. Key, L. B. DaSilva., S. G. Glendinning, J. P. Knauer, B. A. Remington, F. Weber, and S. V. Weber, Phys. Rev. Lett. **76** (1996).

[71] R. Keenan et al., J. Phys. B **35**, L447 (2002).

[72] J. E. Bailey et al., Rev. Sci. Instrum. **79**, 113104 (2008).

[73] D. Hoarty, S. James, H. Davies, C. Brown, J. Harris, C. Smith, S. Davidson, E. Kerswill, B. Crowley, and S. Rose, High Energy Density Physics **3**, 115 (2007).

[74] E. Wagenaars et al., HEDP **7**, 17 (2011).

[75] F. J. D. Serduke et al., JQSRT **65**, 527 (2000).

[76] R. H. D. Townsend and J. Macdonald, MNRAS **368**, L57 (2006).

[77] S. J. Rose, J.Phys. B: At. Mol. Opt. Phys **25**, 1667 (1992).

[78] J. A. Gaffney and S. J. Rose, High Energy Density Physics **5**, 216 (2009).

[79] Centre for X-ray Optics Lawrence Berkley National Laboratory, http://henke.lbl.gov/optical_constants.

[80] D. S. Whittaker and G. J. Tallents, MNRAS **400**, 1808 (2009).

[81] E. Shiles et al., Phys. Rev. B **22**, 1612 (1980).

[82] D. Y. Smith et al., in *Handbook of optical constants of solids*, edited by E. D. Palik (Academic press, 1985), p. 369.

[83] B. Henke, E. M. Gullikson, and J. C. Davis, Atomic Data and Nuclear tables **54**, 181 (1993).

[84] J. Nilsen, W. R. Johnson, C. a. Iglesias, and J. H. Scofield, Journal of Quantitative Spectroscopy and Radiative Transfer **99**, 425 (2006).

[85] B. J. B. Crowley, TPN/77/06 (AWE Report 644/11, September, 2011).

[86] R. Smith et al., Phys. Rev. A. **59**, R47 (1999).

[87] G. J. Tallents, J. Phys. D: Appl. Phys. **36**, R259 (2003).

[88] R. Keenan et al., Phys. Rev. Lett. **94**, 103901 (2005).

[89] J. J. Rocca, V. Shlyaptsev, F. G. Tomasel, O. D. Cortázar, D. Hartshorn, and J. L. A. Chilla, Phys. Rev. Lett. **73**, 2192 (1994).

[90] J. J. Rocca, O. D. Cortázar, B. Szapiro, K. Floyd, and F. G. Tomasel, Phys. Rev. E **47**, 1299 (1993).

[91] J. J. Rocca, Review of Scientific Instruments **70**, 3799 (1999).

[92] J. Zhang et al., Science. **276**, 1097 (1997).

[93] B. W. J. McNeil and N. R. Thompson, Nature Photonics **4**, 814 (2010).

[94] L. Young et al., Nature **466**, 56 (2010).

[95] W. Ackermann et al., Nature Photonics **1**, 336 (2007).

[96] E. Allaria, R. Appio, L. Badano, W. Barletta, S. Bassanese, S. Biedron, A. Borga, E. Busetto, D. Castronovo, P. Cinquegrana, et al., Nature Photonics **6**, 699 (2012).

[97] D. Pile, Nature Photonics **5**, 456 (2011).

[98] SACLA (XFEL), http://xfel.riken.jp/eng/index.html, accessed January 2013.

[99] European XFEL, www.xfel.eu, accessed December 2012.

[100] I. C. E. Turcu et al., Proc. SPIE **7469**, 746902 (2010).

[101] F. Frassetto, C. Cacho, C. A. Froud, I. C. E. Turcu, P. Villoresi, W. A. Bryan, E. Springate, and L. Poletto, Optics express **19**, 19169 (2011).

[102] B. Dromey, D. Adams, R. Hörlein, Y. Nomura, S. G. Rykovanov, D. C. Carroll, P. S. Foster, S. Kar, K. Markey, P. McKenna, et al., Nature Physics **5**, 146 (2009).

[103] T. Baeva, S. Gordienko, and A. Pukhov, Physical Review E **74**, 1 (2006).

[104] K. M. Skulina, C. S. Alford, R. M. Bionta, D. M. Makowiecki, E. M. Gullikson, R. Soufli, J. B. Kortright, and J. H. Underwood, Appl. Opt. **34**, 3727 (1995).

[105] P. Mercère, P. Zeitoun, M. Idir, S. Le Pape, D. Douillet, X. Levecq, G. Dovillaire, S. Bucourt, K. a. Goldberg, P. P. Naulleau, et al., Optics letters **28**, 1534 (2003).

[106] B. Flöter, P. Juranić, S. Kapitzki, B. Keitel, K. Mann, E. Plönjes, B. Schäfer, and K. Tiedtke, New Journal of Physics **12**, 083015 (2010).

[107] E. Hecht, *Optics* (Addison - Wesley, 1998).

[108] S. P. Lyon and J. D. Johnson, Los Alamos National Laboratory Report LA-UR-92-3407 (1992).

[109] J. I. Larruquert et al., Appl. Opt. **34**, 4892 (1995).

[110] J. I. Larruquert et al., Appl. Opt. **35**, 5692 (1996).

[111] N. Brimhall, N. Herrick, D. D. Allred, R. S. Turley, M. Ware, and J. Peatross, Applied Optics **49**, 1581 (2010).

[112] K. Rosfjord et al., Proc. SPIE **5538**, 92 (2004).

[113] C. Chang et al., Opt. Lett. **23**, 1028 (2002).

[114] E. M. Gullikson et al., Phys. Rev. B **49**, 283 (1994).

[115] T. Ditmire et al., Phys. Rev. lett. **77**, 4756 (1996).

[116] C. J. Walsh, D. M. Villeneuve, and H. Baldis, Phys. Rev. Lett. **53**, 1445 (1984).

[117] S. P. Regan, R. Epstein, V. N. Goncharov, I. V. Igumenshchev, D. Li, H. S. P. B. Radha, W. Seka, T. R. Boehly, J. A. Delettrez, O. V. Gotchev, et al., Phys. Plasmas **14**, 056305 (2007).

[118] C. Garban-Labaune, E. Fabre, C. E. Max, R. Fabbro, F. Amiranoff, J. Virmont, M. Weinfeld, and A. Michard, Phys. Rev. Lett. **48**, 1018 (1982).

[119] G. Winhart, K. Eidmann, C. Iglesias, A. Bar-Shalom, E. Mnguez, A. Rickert, and S. Rose, JQSRT **54**, 437 (1995).

[120] D. Ros et al. (Springer, Dordrecht, 2011).

[121] P. Mistry, M. Edwards, and G. J. Tallents, Phys. Rev. A **75**, 013818 (2006).

[122] Y. Li, J. Nilsen, J. Dunn, A. L. Osterheld, A. Ryabtsev, and S. Churilov, Phys. Rev. A **58**, R2668 (1998).

[123] G. J. Tallents, M. H. Key, P. Norreys, D. Brown, J. Dunn, and H. Baldis, Phys. Rev. A **40**, 2857 (1989).

[124] H. Chen, B. Soom, B. Yaakobi, S. Uchida, and D. D. Meyerhofer, Phys. Rev. Lett. **70**, 3431 (1993).

[125] D. D. Meyerhofer, H. Chen, J. a. Delettrez, B. Soom, S. Uchida, and B. Yaakobi, Physics of Fluids B: Plasma Physics **5**, 2584 (1993).

[126] National Institute of Standards and Technology Estar database, http://physics.nist.gov/PhysRefData/Star/Text/ESTAR.html.

[127] D. J. Heading, J. S. Wark, R. W. Lee, R. Stamm, and B. Talin, Phys. Rev. E. **56**, 936 (1997).

[128] R. F. Smith, J. Dunn, J. Nilsen, V. N. Shlyaptsev, S. Moon, J. Filevich, J. J. Rocca, M. C. Marconi, J. R. Hunter, and T. W. Barbee, Physical Review Letters **89**, 065004 (2002).

[129] J. Grava, M. Purvis, J. Filevich, M. Marconi, J. Rocca, J. Dunn, S. Moon, and V. Shlyaptsev, Physical Review E **78**, 016403 (2008).

[130] L. M. R. Gartside, G. J. Tallents, A. K. Rossall, E. Wagenaars, D. S. Whittaker, M. Kozlova, J. Nejdl, M. Sawicka, J. Polan, M. Kalal, et al., Optics Lett. **35**, 3820 (2010).

[131] L. Wilson, G. Tallents, J. Pasley, D. Whittaker, S. Rose, O. Guilbaud, K. Cassou, S. Kazamias, S. Daboussi, M. Pittman, et al., Physical Review E **86**, 1 (2012).

[132] J. Filevich, J. Rocca, M. Marconi, S. Moon, J. Nilsen, J. Scofield, J. Dunn, R. Smith, R. Keenan, J. Hunter, et al., Physical Review Letters **94**, 035005 (2005).

[133] M. Fajardo, G. Williams, et al., *Dense plasma diagnostics using high order harmonics, presented at Rad. Prop. Hot Dense Matter* (Santa Barbara, 2012).